THE JOURNAL OF PHYSICAL CHEMISTRY B
A JOURNAL OF THE AMERICAN CHEMICAL SOCIETY

Open Access
This article is licensed under CC-BY 4.0

pubs.acs.org/JPCB
Article

Molecular Thermodynamics of Lower Critical Solution Temperature Ionic Liquid/Water Mixtures: Tetrabutylphosphonium Trifluoroacetate

Published as part of The Journal of Physical Chemistry B special issue "Computer Simulation of Molecular Solids and Liquids: In Honor of Michael L. Klein".

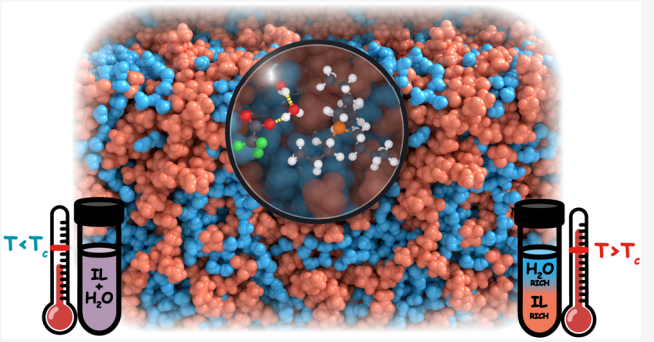
Shehan M. Parmar, Ahmed Mahfouz, Akanksha K. Menon, and Jesse G. McDaniel*

Cite This: https://doi.org/10.1021/acs.jpcb.6c04599

Read Online

ACCESS | Metrics & More | Article Recommendations | Supporting Information

ABSTRACT: Lower critical solution temperature (LCST) ionic liquids (ILs) are thermoresponsive materials that undergo liquid−liquid demixing with water into water-rich (WR) and IL-rich (ILR) phases upon heating. Despite the vast combinatorial space of cation−anion pairings, LCST behavior is observed in only a handful of aqueous ILs. To uncover the enthalpic and entropic driving forces that govern this unique phase behavior among molecular liquids, we investigate an exemplary LCST IL, tetrabutylphosphonium trifluoroacetate ($[P_{4444}][TFA]$), by pairing equilibrium molecular dynamics and finite-concentration thermodynamic integration with chilled-mirror dew point water activity experimental measurements. Computationally predicted excess chemical potentials of water ($\mu^{E}_{H_2O}$) show excellent agreement with experimental measurements over IL weight fractions w_{IL} = 85−95% at T = 300 and 323 K, with absolute deviations ranging from 0.04 to 1.2 kJ mol^{-1}, establishing accurate resolution of the non-ideal solvation contribution. $\mu^{E}_{H_2O}$ is counterbalanced by a strongly favorable ideal entropy of mixing, governed by the large (∼19:1) IL/water molar volume ratio, and a uniformly unfavorable solvation free energy (relative to bulk water). The excess partial molar enthalpy of water ($h^{E}_{H_2O}$) is marked by strong temperature sensitivity, undergoing an exothermic to endothermic shift of ∼5−6 kJ mol^{-1} from 300−373 K. On the other hand, the non-ideal entropy of solvation ($s^{E,n.id.}_{H_2O}$) is uniformly unfavorable. Mechanistically, this enthalpy/entropy temperature dependence is traced to electrostatic screening probed by the charge−correlation structure factor $S_{ZZ}(\mathbf{k})/k^2$, the competing water−water and water−anion interactions, and the structural organization of water imposed by the hydrophobic P_{4444}^{+} cation.



INTRODUCTION

Nearly a century of research has revealed the dichotomous role of water, either as a contaminant or co-solvent, in ionic liquid (IL)/water mixtures. Anhydrous ILs, or room-temperature molten salts, alone span a vast compositional space of ∼10^6 possible cation−anion pairings, offering tunable material selection. The addition of water in ILs has long been documented as an unwanted "impurity," where small amounts (<3% weight) dramatically shift transport properties,[1] limit gas solubilities,[2] and promote unintended and/or hazardous byproducts during synthesis or at electrochemical interfaces.[3−9] Yet when incorporated deliberately, water can modulate neat IL properties for more tailored molecular design. For instance, across various protic/aprotic ILs, water has been shown to broaden the liquidus range of ILs that would otherwise crystallize at room temperature,[10−17] improve mutual solubilities with other organic solvents,[18−20] tune local coordination environments for chemical selectivity,[4,21−25] stabilize proteins and macromolecules,[26−31] and increase ionic conductivity while decreasing viscosity to flexibly meet engineering constraints.[32−34] These contrasting behaviors highlight water as a highly active participant in bulk, thermophysical IL/water properties. Thus, fully realizing water's functional role in IL solutions across diverse compositions, structures, and thermodynamic conditions requires deep, molecular-level insight.

Received: July 10, 2026
Revised: September 9, 2026
Accepted: September 17, 2026

ACS Publications
© XXXX The Authors. Published by American Chemical Society

Downloaded from pubs.acs.org/jpcbfk/article-pdf/doi/10.1021/acs.jpcb.6c04599/6906150/acs.jpcb.6c04599.pdf by GEORGIA INST OF TECHNOLOGY, Shehan Parmar on 04 November 2026

More recently, certain IL/water mixtures have been found to exhibit intriguing thermoresponsive lower critical solution temperature (LCST) phase behavior, prompting interest in catalysis,[35,36] metal ion and protein extraction,[37−44] and thermally driven water desalination.[45−51] Unlike commonly observed upper critical solution temperature (UCST) mixtures—where heating promotes mixing—LCST ILs instead undergo spontaneous liquid−liquid separation, forming two immiscible phases once the system exceeds a critical temperature (T_c), or "cloud point." In a seminal work by Kohno and Ohno,[52] of 48 candidate ILs containing alkylphosphonium/alkylammonium cations, LCST behavior was observed in only six systems. Several combinatorial discovery campaigns observe similar sparse "hit" rates across 1,2,3-triazolium (22 of 160),[53] cycloammonium (6 of 30),[54] and zwitterionic (3 of 12)[55,56] ILs. This narrow selection window is often rationalized *a posteriori* by the subtle balance of hydrophobic/hydrophilic ion substituents, or quantitatively, by the hydrophilicity index (HI),[52,57] i.e., the number of water molecules per ion pair remaining in the demixed phase. While computational and experimental studies have proposed mechanistic hypotheses—entropy loss from directional hydrogen bonding (i.e., a "negative entropy of mixing"),[58−65] nanocluster formation[60,61,66−70]—gaps remain in their generality, e.g., many LCST IL mixtures do not form hydrogen bonds.[71−73] Consequently, understanding the origins of LCST phase behavior requires mechanistic, thermodynamic insight with microscopic structural interpretation.

Molecular thermodynamics provides the natural starting point for understanding LCST IL/water mixture chemistry. Liquid−liquid phase behavior is rationalized by enthalpy and entropy components to the Gibbs free energy of mixing, $\Delta G_{mix} = \Delta H_{mix} - T\Delta S_{mix}$. The microscopic origins of enthalpy—intermolecular IL−IL, water−water, and IL−water interactions—can govern miscibility through competition between large IL cohesive energies (∼−500 kJ mol^{-1}) and ion−water "cross-interactions."[74,75] Extensive research has connected this enthalpic balance to the subtle addition/subtraction of hydrophilic constituents (e.g., small anions such as Cl^-, I^-, BF_4^-) and (relatively) more hydrophobic constituents (e.g., charge-diffuse anions such as PF_6^- and $TFSI^-$, or long-alkyl chain cations such as C_8mim^+).[3,6,76−78] Hydrophobicity does not completely preclude water retention; nominally immiscible IL/water systems can still carry ∼1% weight water due to the inherent hygroscopicity of common ILs.[79] Thus, beyond purely local features (i.e., ion size, shape, charge distribution, hydrogen-bond strength and directionality), McDaniel and Verma[80] emphasize that long-range electrostatics more decisively influence miscibility, explaining why even structurally similar ions can exhibit disparate phase behaviors.

Entropic contributions originate from spatial order and loss of configurational microstates.[81] In pure water, spatial order emerges from cooperative formation of hydrogen-bond (H-bond) clusters characterized by varied (often tetrahedral) topologies and transient (∼1−10 ps) lifetimes.[82−88] The pioneering work of Frank and Wen[89] established that near infinite dilution, small and highly charged kosmotropes (i.e., "structure-making" ionic solutes) enhance water's *local* order and induce an entropy penalty, whereas larger, charge-diffuse chaotropes ("structure-breaking" ions) disrupt the surrounding H-bond network.[90−93] Generalizing these infinite-dilution principles, however, has sparked much debate in the literature. While many studies argue that ions and simple salts perturb water structure *beyond* their first solvation shells,[94−105] spectroscopy experiments[106−110] and molecular dynamics (MD) simulations[111] indicate that, for single ions in bulk water, reorientational dynamics and H-bond lifetimes outside the first hydration shell remain largely unchanged. Evidently, as these principles are extended from single ions toward concentrated aqueous salt mixtures, what precludes a universal understanding of the microscopic origins of entropy is the diversity in ion molecular structure, from size, shape, and charge distribution to functional groups. For instance, amphiphilic ions have large and predominantly entropic (solvation) free energy costs associated with cavity formation to accommodate nonpolar moieties, often resulting in compensation via self-assembly or aggregation, i.e., the hydrophobic effect.[81,94,112−118] Moreover, the water structure near ion pairs is strongly size-dependent.[81] Collins' seminal "law of matching water affinities"[119] established that ion pairs of comparable size (e.g., Li^+/F^-, Cs^+/I^-) favor ion−ion contact in solution—either through strong electrostatics for small, highly hydrated ions or hydrophobic association for large, weakly hydrated ions—whereas asymmetric pairings are preferentially separated by the solvent (e.g., water "cages") to compensate for an imbalance in solvation enthalpies.[120,121]

Beyond these paradigms of infinite dilution and simple aqueous electrolytes, achieving a mechanistic understanding of enthalpy−entropy balance for general IL/water mixtures remains an active area of research. Most studies examine how changing (1) IL composition,[122−133] (2) water concentration (i.e., mole fraction, x_{H_2O}),[7,124,126,128,131,132,134−148] and less frequently, (3) thermodynamic conditions,[125,142,149,150] modulate structure, transport, and phase behavior. A common observation in composition-centric studies is that the electrostatic strength of ion−water interactions dictates excess chemical potentials and, therefore, miscibility.[18,151] Anion−water interactions are thus especially important in this regard. On the one hand, hydrophilic anions (e.g., carboxylates, ethanoate, halides, nitrate, trifluoroacetate, etc.) form strong, enthalpically favorable H-bonds that promote water miscibility; on the other hand, highly fluorinated and/or charge-delocalized anions (e.g., PF_6^-, $TFSI^-$, tricyanomethanide, etc.) form ILs that are typically hydrophobic and immiscible with water.[18,20,125,152−155] Between these extremes lie partially miscible ILs, including those containing BF_4^-, $CF_3SO_3^-$, and phosphate anions, where miscibility is much more sensitive to the cation hydrophobicity, which increases based on the cationic core (i.e., imidazolium < pyridinium < tetraalkylphosphonium) and side-chain length.[20,156,157]

While a comprehensive review of concentration-dependent IL/water behavior is beyond the scope of this work, several themes emerge from the literature. Studies commonly delineate qualitative "compositional regimes":[158] trace or water-scarce (IL-rich) ($x_{H_2O} \lesssim 0.2$), intermediate ($0.2 \lesssim x_{H_2O} \lesssim 0.9$), and water-rich ($x_{H_2O} \gtrsim 0.9$) concentrations. In IL-rich regimes, cation−anion interactions (e.g., Coulombic, H-bonding, $\pi-\pi$ stacking) dictate liquid morphology. For common room-temperature ILs (RTILs), Cammarata et al.[122] describe water in this regime as "free", that is, rather than forming self-associated water clusters as in the pure liquid, monomeric water is randomly dispersed throughout the IL matrix with a preference to coordinate into anion···H−O−H··· anion complexes. This behavior is supported by IR spectroscopy, where water O−H stretching modes in RTILs lie

https://doi.org/10.1021/acs.jpcb.6c04599
J. Phys. Chem. B XXXX, XXX, XXX−XXX

Downloaded from pubs.acs.org/jpcbfk/article-pdf/doi/10.1021/acs.jpcb.6c04599/6906150/acs.jpcb.6c04599.pdf by GEORGIA INST OF TECHNOLOGY, Shehan Parmar on 04 November 2026

between those of water vapor (red-shifted from vapor) and bulk water (blue-shifted from bulk), indicating anion-coordinated water.

As water concentration increases, mixtures transition from locally governed structure to markedly more complex, heterogeneous, and mesoscopic domain formation. Notably, the boundaries of an "intermediate" regime vary substantially across IL chemistries, where distinct structural "turnover" points emerge from competing water−water, water−ion, and ion−ion interactions. For instance, López-Pastor et al.[159] observed early onset of cyclic water dimers in [EMIM][BF_4] and [BMIM][BF_4] at $x_{H_2O} \approx 0.04-0.07$, in which water simultaneously H-bonded both to an anion and to a neighboring water. In [C_4MIM][BF_4], Gao and Wagner[145] identify a "microphase transition" via small-angle neutron scattering (SANS), where water nanoclusters (i.e., an inverse microemulsion) form at $x_{H_2O} \approx 0.7$. In longer-chain imidazolium cations, such as [C_{10}MIM][BF_4], Maia et al.[160] observed no intermediate structural transition, with liquid−liquid phase separation occurring only once water-rich concentrations were reached ($x_{H_2O} \approx 0.9$). Abe et al.[161] showed that a subtle anion change from BF_4^- to NO_3^- (i.e., [C_4MIM][NO_3]) leads to 20 Å−sized "water pockets" at x_{H_2O} = 0.7−0.9. Likewise, Jiang et al.[135] report a stark structural "turnover" in [C_8MIM][NO_3] at x_{H_2O} = 0.75−0.8, corresponding to the highly ordered cation−cation (i.e., micellar) and water−anion−water structures before they collapse past the percolation limit from increased dilution. Taken together, these studies highlight the need to consider the *entire* range of concentrations to understand LCST IL/water mixtures.

Despite the wealth of these bulk structure trends derived from IL composition and concentration, free energies and thermodynamic properties are necessary to understand phase behavior. In theory, structural descriptors (e.g., pair correlation functions) can encode chemical potential and water activity; in practice, computing thermodynamic properties—most notably through Kirkwood−Buff (KB) integrals[162−164]—suffers from finite-size effects and high sensitivity to systems with significant long-range order.[162,165] Beyond static structure, translational/rotational diffusion and other dynamic properties (e.g., Debye−Stokes−Einstein (DSE) curves,[166,167] viscosity B-coefficients[168,169]) offer valuable insight into how ion−water transport relates to solvation and solubility under classical hydrodynamic assumptions; this relationship, however, is less well-defined for the many ILs and IL-based mixtures that exhibit "spatially heterogeneous dynamics."[170−172]

To this end, we directly investigate solvation free energies, partial molar enthalpies, and entropies of an exemplary LCST IL, tetrabutylphosphonium trifluoroacetate, [P_{4444}][TFA]. This IL is known for its low critical temperature (T_c ~303 K) and wide two-phase concentration window (30% $\lesssim w_{H_2O} \lesssim$ 90% weight H_2O).[173−175] Rationalizing its ion pairing behavior in water proves to be more complex than simple cation−anion additivity. Concretely, despite being among the most hydrophobic IL cations, P_{4444}^+ exhibits starkly different phase behavior depending on anion pairing. Fukaya et al.[176] observed LCST or UCST behavior for compositionally identical anions, the *trans*− and *cis*−isomers fumarate and maleate, respectively; even more puzzling was the absence of all LCST and UCST behavior in the ternary mixture! Moreover, TFA^- is hydrophilic and a weak base (the conjugate base of trifluoroacetic acid, pK_a = 0.52[177]), has a favorable (absolute) aqueous solvation free energy (~−251 kJ mol^{-1} ref[178]), and is thus expected to form strong hydrogen bonds with water.[122] Together, [P_{4444}][TFA]/H_2O mixtures consistently show gradual (e.g., ~1 h at 323 K ref[179]) ion−ion aggregate formation near the LCST critical point.[60,61,66,67,69,180−182] Therefore, we hypothesize that molecular thermodynamics can explain the origin of LCST phase behavior in [P_{4444}][TFA].

To this end, we perform equilibrium molecular dynamics (MD) simulations across a comprehensive range of temperatures and concentrations. In addition, we obtain chemical potentials and their enthalpy/entropy decomposition through thermodynamic integration (TI) and chilled-mirror dew point temperature experiments. Thus, to the best of our knowledge, we present the first direct comparison of simulation and experiments of excess chemical potentials of water for [P_{4444}][TFA]/H_2O mixtures. We first describe the formalism and protocols used to compute chemical potentials and their enthalpy/entropy decomposition from alchemical free energy techniques and experimental measurements of water activity. In the Results and Discussion section, we elucidate the plausible mechanisms that drive LCST behavior in [P_{4444}][TFA]/H_2O mixtures through partial molar enthalpy/entropy decomposition, the charge−correlation structure factor, radial and spatial distribution functions, and graph network aggregation analyses. We find that the LCST behavior of [P_{4444}][TFA]/H_2O is shaped by the counterbalance of a favorable ideal entropy of mixing and unfavorable solvation free energies, explained by a tightly coupled enthalpy−entropy compensation. The partial molar enthalpies are strongly temperature-sensitive, shifting from exothermic to endothermic over 300−373 K, and directly correspond to long-range electrostatics, as shown by the charge−correlation structure factor. Structural analyses further reveal three concentration regimes and the structural organization imposed by the hydrophobic P_{4444}^+ cation.

THEORY AND METHODS

Experimental Methods

Water Activity. For an IL/water solution at a given concentration below its phase separation temperature, the water activity, a_w, is < 1, due to the vapor pressure (P_v) of water in the solution being lower than the saturation pressure of pure water at that temperature (P_{sat}). To measure a_w, a chilled-mirror dew point temperature experimental technique was utilized. The IL/water solution loses a small amount of moisture within a hermetically sealed chamber until the gaseous phase is in thermodynamic equilibrium with the liquid phase. A small mirror within the chamber is then chilled until dew forms. From the dew point temperature (T_{dp}), P_v is determined. Water activity is then calculated as $a_w = P_v(T_{dp})/P_{sat}(T)$. The AQUALAB 4TE water activity meter was utilized to measure the water activities of all of the solutions in this work, with an accuracy of $a_w \pm 0.003$. For each sample, five measurements were taken and averaged. To resolve the temperature dependence of a_w, measurements were performed at six temperatures from 298−323 K in 5 K increments for IL weight fractions of w_{IL} = 85, 90, and 95%. The [P_{4444}][TFA] IL was synthesized following the procedure outlined in our previous work,[51,173,183] and NMR was performed to confirm the chemical structure and purity.

Downloaded from pubs.acs.org/jpcbfk/article-pdf/doi/10.1021/acs.jpcb.6c04599/6906150/acs.jpcb.6c04599.pdf by GEORGIA INST OF TECHNOLOGY, Shehan Parmar on 04 November 2026

https://doi.org/10.1021/acs.jpcb.6c04599
J. Phys. Chem. B XXXX, XXX, XXX−XXX

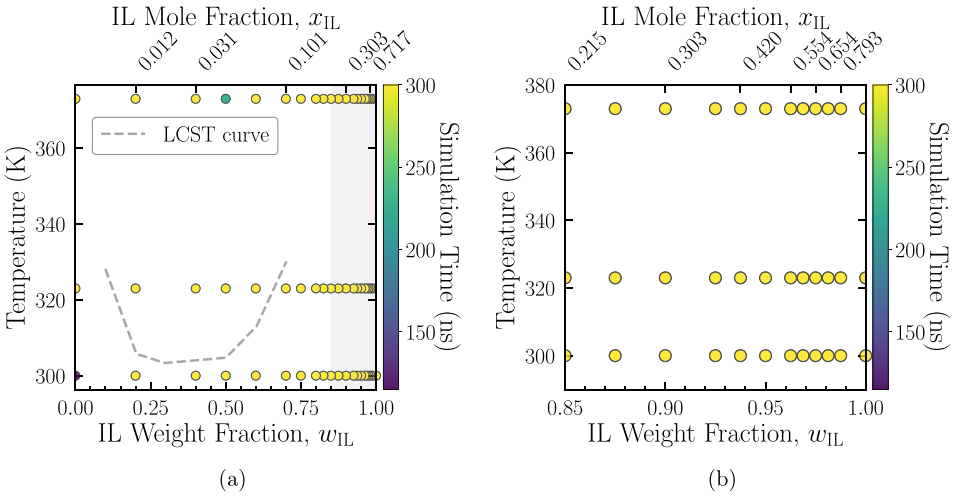


Figure 1. Temperatures and IL weight fractions, w_{IL}, of all simulations completed in this work, along with the $[P_{4444}][TFA]$ IL lower critical solution temperature (LCST) curve (gray dashed lines) from our previous work,[173] with (a) the full concentration window and (b) IL-rich region only ($w_{IL} \geq 0.85$). Marker color denotes the total production simulation time of each state point (Table S1). Adapted from ref 173. Available under a CC BY 3.0 license. Copyright 2025 Mahfouz, A.; Haddad, A. Z.; Kocher, J. D.; Menon, A. K.

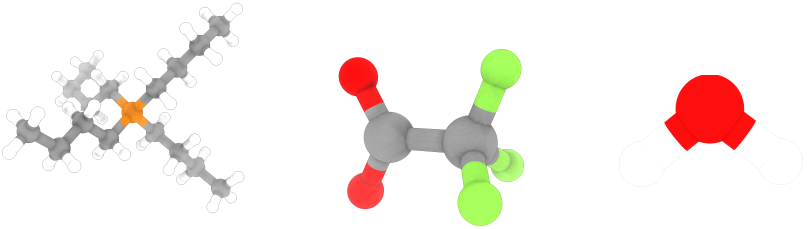


Figure 2. Molecular structures of species investigated in this work. Atoms include hydrogen (white), carbon (gray), oxygen (red), phosphorus (orange), and fluorine (light green).

Density. A handheld density meter (Mettler Toledo Handheld Densito) was used to characterize the density of the IL/water solutions at 298 K. The density of each solution was measured three times to determine the mean solution density. The density meter has a resolution of 0.0001 g cm^{-3} and an accuracy of ±0.001 g cm^{-3}.

Molecular Dynamics Simulation Details

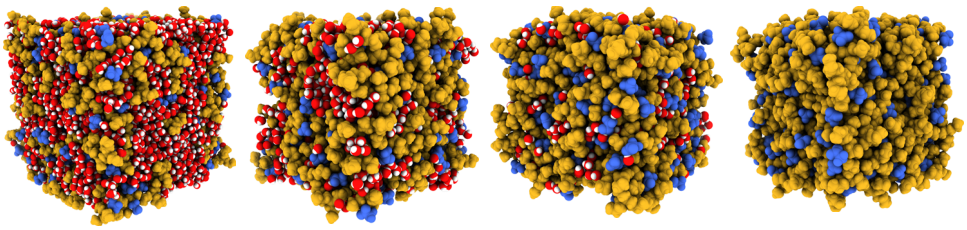
Equilibrium molecular dynamics (MD) simulations were performed for bulk, aqueous $[P_{4444}][TFA]$ IL mixtures in the *NPT* ensemble at 300, 323, and 373 K and 1 atm. Twenty-one distinct concentrations were simulated at each temperature, resulting in sixty-three independent simulations. System concentrations and conditions are summarized in Table S1. Additionally, $[EMIM][TFA]/H_2O$ simulations at comparable concentrations and temperatures (Table S2) were conducted to facilitate later comparative analyses. Although some simulated state points fall above the experimental LCST curve for $[P_{4444}][TFA]$, shown in Figure 1, all systems remained single-phase under the present simulation time scales. A representative overlapping state point (w_{IL} = 40%, 323 K) extended to ∼1 μs exhibits no phase separation (Figure S1), confirming a well-equilibrated single-phase system rather than insufficient sampling. This behavior is consistent with previous reports of spontaneous liquid−liquid phase separation in IL/water mixtures,[184−18769] and is a generally expected outcome, given the length and time scales required to observe phase transition behavior[188−193] and the sensitivity of equilibrium MD phase behavior to short- and long-range electrostatics, and hence the need for charge scaling[194] or polarizable force fields,[195] both beyond the scope of this work.

The LigParGen[196] tool was used to assign nonpolarizable OPLS-AA[197−199] force field parameters for all IL species, where partial atomic charges were determined via the 1.14*CM1A charge model.[200] Water−water interactions are governed by the TIP3P[201] model, where rigid water molecules were constrained using the SETTLE algorithm.[202] TIP3P is one of several standard nonpolarizable water models. Benchmarks against the four-site TIP4P/2005[203] and three-site SPC/E[204] confirm semiquantitative agreement in the thermodynamic and structural properties examined in this work (Section S22, Figures S29−S31), indicating that this choice does not materially affect subsequent results and conclusions. Lennard−Jones cross-interactions of sigma (σ) and epsilon (ϵ) parameters were obtained from geometric combination rules (i.e., $\sigma_{ij} = \sqrt{\sigma_i \sigma_j}$ and $\epsilon_{ij} = \sqrt{\epsilon_i \epsilon_j}$), per the OPLS-AA convention. The P_{4444}^{+} cation and TFA^{-} anion are shown in Figure 2a and b, respectively.

Initial configurations were generated using PACKMOL[205,206] to achieve the target mole fractions, followed by ∼10 ns *NPT* density equilibration simulations. The equilibrated density of neat $[P_{4444}][TFA]$ at room temperature (1.046 g cm^{-3}) showed excellent agreement within ∼1% of the extrapolated experimental density (∼1.035 g cm^{-3}), as well as excellent agreement for IL-rich concentrations shown in Table

https://doi.org/10.1021/acs.jpcb.6c04599
J. Phys. Chem. B XXXX, XXX, XXX−XXX

Downloaded from pubs.acs.org/jpcbfk/article-pdf/doi/10.1021/acs.jpcb.6c04599/6906150/acs.jpcb.6c04599.pdf by GEORGIA INST OF TECHNOLOGY, Shehan Parmar on 04 November 2026



(a) $w_{IL} = 40\%$ $x_{IL} = 0.031$ (b) $w_{IL} = 75\%$ $x_{IL} = 0.127$ (c) $w_{IL} = 87.5\%$ $x_{IL} = 0.253$ (d) $w_{IL} = 100\%$ $x_{IL} = 1.0$

Figure 3. Equilibrium snapshots of bulk-phase aqueous $[P_{4444}][TFA]$ mixtures with varying weight fractions, w_{IL}, of the IL species. P_{4444}^{+} cations depicted as goldenrod and TFA^{-} anions as royal blue. Systems are rendered with visually consistent scales for clarity, i.e., not rendered to physical scale.

S3. Densities across all temperatures and concentrations (Figure S2) are reported with statistical uncertainties of approximately 0.4−0.5%. Subsequent *NPT* production simulations were carried out at various time scales depending on temperature and desired sampling, as summarized in Table S1, with trajectory frames saved every 30 ps; property-specific sampling and analysis details are given in the Results and Supporting Information.

Simulations were conducted in the OpenMM software version 8.2.[207,208] on NVIDIA Tesla V100 GPUs. The van der Waals (VDW) interactions were truncated at 1.4 nm, and electrostatics were computed using the particle-mesh Ewald (PME) method.[209] A Monte Carlo barostat was used for pressure coupling, and a Langevin integrator was used with a 1 fs timestep and the friction coefficient set to 1 ps^{-1}. Representative equilibrium snapshots of bulk $[P_{4444}][TFA]/H_2O$ mixtures at selected IL mole fractions are shown in Figure 3.

Free Energy Simulations

Absolute Chemical Potential. The primary focus of this work is to (1) compute and (2) decompose the chemical potential of a water solute molecule in a $[P_{4444}][TFA]/H_2O$ mixture, M, at various weight fractions, w, and temperatures, T. Generally, the *absolute* chemical potential of water in a $[P_{4444}][TFA]/H_2O$ mixture is the partial molar Gibbs free energy, G; thus, for an isobaric−isothermal system,

$$\mu^{M}_{H_2O} = G(N_{H_2O} + 1, N_{IL}, P, T) - G(N_{H_2O}, N_{IL}, P, T) \quad (1)$$

where N_{H_2O} and N_{IL} are the number of water molecules and ion pairs, respectively, and P is the internal pressure of the liquid mixture. In the thermodynamic limit, $\mu^{M}_{H_2O} = (\partial G/\partial N_{H_2O})_{N_{IL},P,T}$.

Several authors, including Ben-Naim[210] and Shirts et al.,[211] have provided detailed discussions on the interpretation of the *absolute* chemical potential of a solute molecule. For completeness, we provide a derivation of the chemical potential of water in mixture M, $\mu^{M}_{H_2O}$, in the Supporting Information. Equations S1−S6 result in the following expression for the *absolute* chemical potential of a water solute molecule in an IL/water mixture:

$$\mu^{M}_{H_2O} = \Delta\mu_{solv} + k_B T \ln[\rho^{M}_{H_2O}(\Lambda^{M}_{H_2O})^3] - k_B T \ln[q^{M}_{H_2O}] \quad (2)$$

where $\Delta\mu_{solv}$ is the solvation free energy typically derived from alchemical free energy techniques, k_B is the Boltzmann constant, T is the absolute mixture temperature, $\rho^{M}_{H_2O}$ is the water solute molecule *number* density, $\rho_i = N_i/\langle V\rangle$, within the mixture, $\Lambda^{M}_{H_2O} = (h^2/2\pi M_{H_2O} k_B T)^{1/2}$ is the thermal de Broglie wavelength arising from momentum integration, h is Planck's constant, M_{H_2O} is a water molecule's mass, and $q^{M}_{H_2O}$ is the internal partition function of a water molecule.

It is evident from eq 2 that the *absolute* chemical potential is, in its general form, composed of four physically interpretable terms: (1) the "coupling" work, or the "interaction" Gibbs free energy, $\Delta\mu_{solv}$, due to the solute, H_2O, solvated within the IL/water liquid mixture; (2) the "liberation"[210] Gibbs free energy, $k_B T \ln[(\Lambda^{M}_{H_2O})^3] - k_B T \ln[V]$, (see eq S4) involved with (2a) releasing the (classical) solute particle from a fixed position such that it acquires kinetic energy from translational momenta $(\Lambda^{M}_{H_2O})$ and (2b) the entropy associated with the solute's exposure to the entire mixture volume, V, be it via compression or decompression; (3) the indistinguishability term, $k_B T \ln[N_{H_2O}]$, sometimes referred to as the "assimilation" free energy;[210] and (4) the internal degrees of freedom as modulated by the solvation environment $(q^{M}_{H_2O})$.

In this work, free energies of solvation are computed by thermodynamic integration (TI),[212−217] in which a specific solute water molecule i is gradually decoupled from the surrounding solvent,

$$\Delta\mu^{i}_{solv} = \int_0^1 d\lambda \left\langle \frac{\partial U(\lambda)}{\partial \lambda} \right\rangle_\lambda \quad (3)$$

where $U(\lambda)$ is the total system potential energy as a function of the coupling parameter λ, with $(\lambda = 1)$ the coupled state (solute is fully interacting with the solvent) and $(\lambda = 0)$ the decoupled state (solute−solvent interactions are turned off). Assuming ergodic sampling, eq 3 provides the absolute solvation free energy of water from a single-solute TI simulation. However, bulk, IL/water mixtures are defined by marked spatial heterogeneity and highly viscous dynamics in which a single solute (water) molecule may encounter significant variation in its local microsolvation environment. Consequently, single-solute TI simulations risk sampling a narrow subset of the IL/water mixture's entire configurational phase space, leading to potentially non-ergodic estimates of the solvation free energies.[218] To this end, we employ a multi-solute, fixed-radius sampling strategy in which independent TI simulations are performed for many distinct water molecules randomly selected from the equilibrated mixture. For each solute, we compute solvation free energies over a time scale consistent with a local microenvironment determined by the mean squared displacement (MSD). Thus, the absolute

https://doi.org/10.1021/acs.jpcb.6c04599
J. Phys. Chem. B XXXX, XXX, XXX−XXX

Downloaded from pubs.acs.org/jpcbfk/article-pdf/doi/10.1021/acs.jpcb.6c04599/6906150/acs.jpcb.6c04599.pdf by GEORGIA INST OF TECHNOLOGY, Shehan Parmar on 04 November 2026

solvation free energy of water in the IL/water mixture is given by the average over all solute molecules,

$$\Delta\mu_{\mathrm{solv}} = \frac{1}{N}\sum_{i}^{N}\Delta\mu_{\mathrm{solv}}^{i},\ N \le N_{\mathrm{H_2O}} \tag{4}$$

where we select N = 23−100 for computational feasibility (Table S6). Of the concentrations and temperatures simulated in Figure 1, we select IL-rich concentrations (w_{IL} = 70, 80, 85, 90, 92.5, and 95%) for subsequent solvation free energy simulations. All details regarding the system Hamiltonian (i.e., linear coupling of λ with electrostatic, van der Waals, and soft-core, repulsive interactions), evaluation of $\langle \partial U(\lambda)/\partial\lambda\rangle_{\lambda}$, and the multi-solute, fixed-radius protocol are provided in the Supporting Information, S5.

Excess Chemical Potential. Excess thermodynamic functions are defined relative to a known reference, or standard state, primarily to enable useful approximations of activities that are not directly measured, and in turn, highlight deviations from ideal or pure behavior. While the choice of standard state is inherently arbitrary,[219] a precise definition is required to define activity. Here, we take the chemical potential of water in pure water, $\mu^{\mathrm{p}}_{\mathrm{H_2O}}$, as our standard state, and define the *excess* chemical potential of water as

$$\mu^{\mathrm{E}}_{\mathrm{H_2O}} = \mu^{\mathrm{M}}_{\mathrm{H_2O}} - \mu^{\mathrm{p}}_{\mathrm{H_2O}} \tag{5}$$

where

$$\begin{aligned}\mu^{\mathrm{p}}_{\mathrm{H_2O}}(T, P = 1\mathrm{atm}) &= \Delta\mu^{\mathrm{p}}_{\mathrm{solv}} + k_{\mathrm{B}}T\ln[\rho^{\mathrm{p}}_{\mathrm{H_2O}}(\Lambda^{\mathrm{p}}_{\mathrm{H_2O}})^3] \\ &\quad - k_{\mathrm{B}}T\ln[q^{\mathrm{p}}_{\mathrm{H_2O}}]\end{aligned} \tag{6}$$

and all terms denote properties of a water solute molecule in pure water (denoted by p). Importantly, this standard state is temperature-dependent, defined at the mixture temperature T rather than at a fixed reference temperature (e.g., 298 K), ensuring that the excess chemical potential isolates deviations due to the solvation environment rather than temperature effects. We note that the internal partition function of a water solute in pure water, $q^{\mathrm{p}}_{\mathrm{H_2O}}$, is simply a product of vibrational, rotational, and electronic terms (e.g., $q = q_{\mathrm{rot}}q_{\mathrm{vib}}q_{\mathrm{elec}}$). Since q_{rot} is a function of molecular geometry alone,[220] it cancels between the mixture and pure states in the excess chemical potential. The electronic partition function is assumed to be unity at ambient temperatures, since only the electronic ground state is populated and defines the zero of energy. The vibrational partition function, however, requires consideration as intramolecular vibrational frequencies are known to shift with the solvation environment; it has been shown that vibrational spectra containing hydroxyl stretches of water at low concentrations in common ILs reveal pronounced blue shifts relative to their vibrational frequency in bulk water.[221] The vibrational partition function is a product over normal modes,[220]

$$q^{\mathrm{p,H_2O}}_{\mathrm{vib}} = \prod_{i=1}^{N_{\mathrm{vib}}}\frac{e^{-\beta h\nu_i^{\mathrm{H_2O}}/2}}{1 - e^{-\beta h\nu_i^{\mathrm{H_2O}}}} \tag{7}$$

where $\beta \equiv (k_{\mathrm{B}}T)^{-1}$ and $\nu_i^{\mathrm{H_2O}}$ is the frequency of vibrational mode i (i.e., symmetric stretch, antisymmetric stretch, and bending) of an H_2O molecule in the bulk liquid p. In the ground-state approximation, where $h\nu \gg k_{\mathrm{B}}T$ is true for the bending and stretching modes of water (∼1600−3700 $\mathrm{cm^{-1}}$) relative to $k_{\mathrm{B}}T$ (≈ 200 $\mathrm{cm^{-1}}$ at 300 K), the third term of eq 6 reduces to

$$-k_{\mathrm{B}}T\ln\left[\prod_{i=1}^{N_{\mathrm{vib}}}\frac{e^{-\beta h\nu_i^{\mathrm{H_2O}}/2}}{1 - e^{-\beta h\nu_i^{\mathrm{H_2O}}}}\right] \approx \sum_{i=1}^{3}\frac{1}{2}h\nu_i^{\mathrm{H_2O}} \tag{8}$$

Consequently, the resulting expression for the excess chemical potential of water from computational methods is

$$\begin{aligned}\mu^{\mathrm{E}}_{\mathrm{H_2O}} &= (\Delta\mu_{\mathrm{solv}} - \Delta\mu^{\mathrm{p}}_{\mathrm{solv}}) + k_{\mathrm{B}}T\ln\left[\frac{\rho^{\mathrm{M}}_{\mathrm{H_2O}}}{\rho^{\mathrm{p}}_{\mathrm{H_2O}}}\right] \\ &\quad + \sum_{i=1}^{3}\frac{1}{2}h(\nu_i^{\mathrm{M,H_2O}} - \nu_i^{\mathrm{p,H_2O}})\end{aligned} \tag{9}$$

where the difference in vibrational partition functions between water in the IL/water mixture and in pure water depends on $\Delta\nu_i = \nu_i^{\mathrm{M,H_2O}} - \nu_i^{\mathrm{p,H_2O}}$. In the case of 24:1 [BMIM][PF_6]:water (D_2O + H_2O) solutions, FT-IR spectra reveal an O−D stretch of HOD that is pronouncedly blue-shifted from 2510 $\mathrm{cm^{-1}}$ in bulk water to 2678 $\mathrm{cm^{-1}}$ in the IL environment.[221] This shift corresponds to an increase in zero-point vibrational energy of approximately ∼1.0 kJ $\mathrm{mol^{-1}}$. Given that similar data is unavailable for [P_{4444}][TFA]/H_2O mixtures, the $\sum_{i=1}^{3}\frac{1}{2}h\Delta\nu_i$ term is neglected (in lieu of more advanced QM/MM simulations[222]) as an unquantifiable error of comparable magnitude (∼1 kJ $\mathrm{mol^{-1}}$).

Equivalently, the choice of standard state from eq 6 remains consistent with experimental water activity measurements described above,

$$\mu^{\mathrm{E}}_{\mathrm{H_2O}} = \mu^{\mathrm{M}}_{\mathrm{H_2O}} - \mu^{\mathrm{p}}_{\mathrm{H_2O}}(T, P = 1\ \mathrm{atm}) = \mathrm{k_BTln[a_w]} \tag{10}$$

Enthalpy and Entropy Decomposition. The excess chemical potential of water is decomposed into (excess) partial molar enthalpy ($h^{\mathrm{E}}_{\mathrm{H_2O}}$) and entropy ($s^{\mathrm{E}}_{\mathrm{H_2O}}$) contributions,

$$\mu^{\mathrm{E}}_{\mathrm{H_2O}} = h^{\mathrm{E}}_{\mathrm{H_2O}} - Ts^{\mathrm{E}}_{\mathrm{H_2O}} \tag{11}$$

where the excess entropy (of solvation) of water is defined as

$$s^{\mathrm{E}}_{\mathrm{H_2O}} \equiv -\left(\frac{\partial\mu^{\mathrm{E}}_{\mathrm{H_2O}}}{\partial T}\right)_{P,N_{\mathrm{H_2O}},N_{\mathrm{IL}}} \tag{12}$$

Obtaining entropic contributions from molecular simulations is a long-standing computational challenge.[223−231] For simple molecular liquids, free energies rapidly converge to within ∼±0.2 kJ $\mathrm{mol^{-1}}$,[200,211,232] while entropies require an order-of-magnitude[233] greater computational cost because of the temperature derivative in eq 12 only to achieve comparable, ∼±2 kJ $\mathrm{mol^{-1}}$ accuracy.[229] The early work of Wan, Stote, and Karplus[229] demonstrated this convergence challenge across five methods for computing $-Ts^{\mathrm{E}}_{\mathrm{H_2O}}$. Compared to finite-difference methods, which obtained $-Ts^{\mathrm{E}}_{\mathrm{H_2O}}$ uncertainties as low as ±1 kJ $\mathrm{mol^{-1}}$, "direct" approaches (i.e., first computing potential energy averages to obtain enthalpy and then computing entropy by subtraction) resulted in ∼±11 kJ $\mathrm{mol^{-1}}$ uncertainties with simulations available at the time—a gap attributed to much faster converging solute−solvent interaction energies that govern free energies compared to slower

Downloaded from pubs.acs.org/jpcbfk/article-pdf/doi/10.1021/acs.jpcb.6c04599/6906150/acs.jpcb.6c04599.pdf by GEORGIA INST OF TECHNOLOGY, Shehan Parmar on 04 November 2026

https://doi.org/10.1021/acs.jpcb.6c04599
J. Phys. Chem. B XXXX, XXX, XXX−XXX

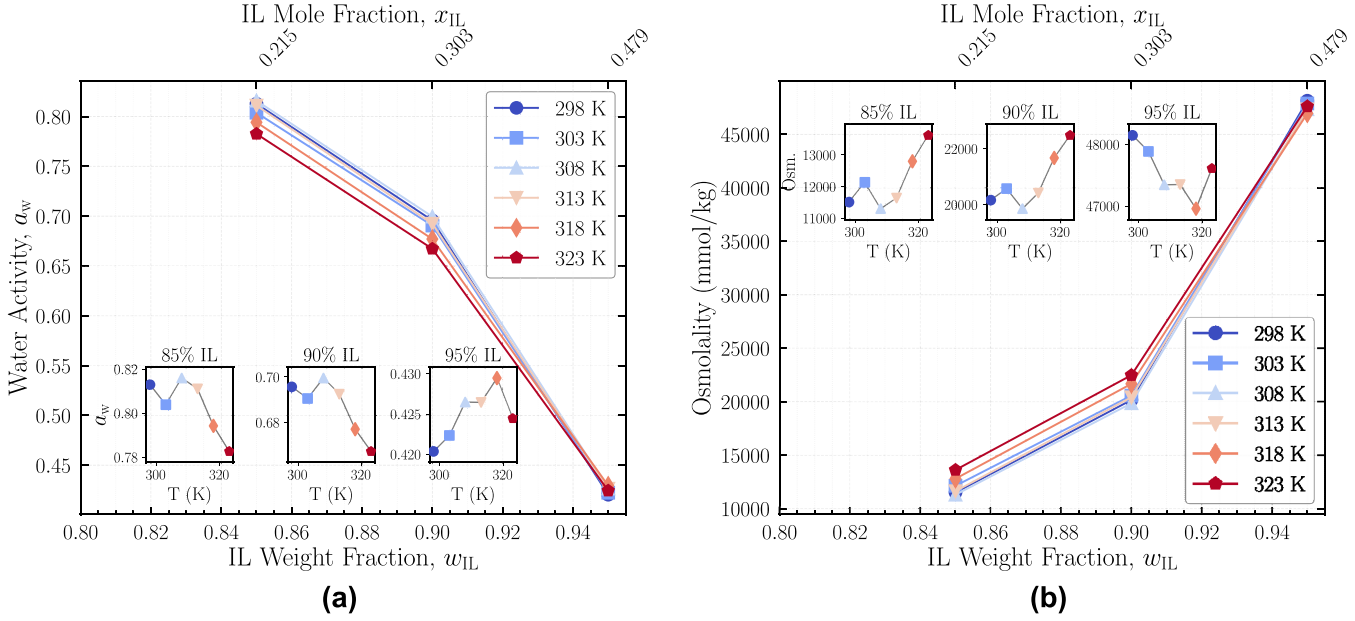


Figure 4. Water activity (a) and osmolalities (b) of $[P_{4444}][TFA]/H_2O$ mixtures as a function of IL weight fraction (w_{IL}) for temperatures across 298−323 K. Insets in both panels show the temperature dependence at fixed IL weight fractions (85, 90, and 95%).

converging solute−solvent total energies. More recently, Jorgensen[233] demonstrated that increased system sizes and longer simulations could improve "direct" methods to comparable, ∼±2 kJ mol^{-1} uncertainties.

We obtain $-Ts^{E}_{H_2O}$ by subtraction (eq 11), having independently computed $\mu^{E}_{H_2O}$ from TI and the (excess) partial molar enthalpy of water, $h^{E}_{H_2O}$, from equilibrium MD. By definition,

$$h^{E}_{H_2O} = h^{M}_{H_2O} - h^{p}_{H_2O}(T, 1\ \text{atm}) \tag{13}$$

where $h^{M}_{H_2O}$ is the partial molar enthalpy of water in the IL/water mixture and $h^{p}_{H_2O}(T)$ is the (standard state) pure component molar enthalpy of liquid water. Like eq 1, the partial molar enthalpy of water could be found by its definition, $h^{M}_{H_2O} \equiv (\partial H^{M}/\partial N_{H_2O})_{N_{IL},P,T} = H^{M}(N_{H_2O} + 1, N_{IL}, P, T) - H^{M}(N_{H_2O}, N_{IL}, P, T)$, where H^{M} is the total IL/water mixture enthalpy. An equivalent expression for *absolute* partial molar quantities (see eqs S13−S16) is given by

$$h^{M}_{H_2O} = h^{E}_{M} - x_{IL}\frac{\partial h^{E}_{M}}{\partial x_{IL}} + h^{p}_{H_2O} \tag{14}$$

where the molar excess enthalpy of the IL/water mixture is

$$h^{E}_{M} = h_{M} - [x_{IL}h^{p}_{IL} + x_{H_2O}h^{p}_{H_2O}] \tag{15}$$

where h_M is the total molar enthalpy of the IL/water mixture. The total (extensive) enthalpy is derived from molecular simulations via the ensemble average of the system potential energy U,

$$h_{M}\cdot(N_{H_2O} + N_{IL}) = H(N_{H_2O}, N_{IL}, P, T) = \langle U + PV\rangle_{NPT} \approx \langle U\rangle_{NPT} \tag{16}$$

where the pressure−volume work contribution is negligible relative to the internal energies of the liquid system, and thus ignored. We note that intramolecular contributions to water's energy are absent, given the use of a rigid water model; the potential energy U therefore reflects only intermolecular interactions and intramolecular contributions from the flexible ionic liquid force field.

In contrast to simulation-based free energy methods, experimental water activity measurements in this work provide direct access to temperature-dependent excess chemical potentials. Thus, the entropy contribution towards the excess chemical potentials from eq 10 is determined using the finite-difference method,

$$-s^{E}_{H_2O}(T) \cong \frac{\mu^{E}_{H_2O}(T + \Delta T) - \mu^{E}_{H_2O}(T - \Delta T)}{2\Delta T} \tag{17}$$

Finally, the entropy contribution itself can be further decomposed into its respective ideal and non-ideal contributions,

$$s^{E}_{H_2O} = s^{E,id.}_{H_2O} + s^{E,n.id.}_{H_2O} \tag{18}$$

For mixtures of components with disparate molecular sizes, such as IL/water systems, regular solution theory is generalized to solutions of unequal molecular components by Flory−Huggins theory.[234−236] In this framework, the ideal entropy is defined using the volume fraction,

$$s^{E,id.}_{H_2O} = -k_B \ln \varphi_{H_2O} \tag{19}$$

where the Flory−Huggins volume fraction is $\varphi_{H_2O} = x_{H_2O}V^{p}_{H_2O}/(x_{H_2O}V^{p}_{H_2O} + x_{IL}V^{p}_{IL})$ and V^{p}_{i} are the pure component molar volumes. This definition is widely used for polymer solutions and is more appropriate for IL/water mixtures, given the significant size asymmetry between the ionic liquid ion pair and water. Equation 19 reduces to the ideal solution expression S18 in the limit of equal molar volumes.

Based on eq 19, a complete expression for the non-ideal entropy (derived in eqs S19−S22) is

https://doi.org/10.1021/acs.jpcb.6c04599
J. Phys. Chem. B XXXX, XXX, XXX−XXX

Downloaded from pubs.acs.org/jpcbfk/article-pdf/doi/10.1021/acs.jpcb.6c04599/6906150/acs.jpcb.6c04599.pdf by GEORGIA INST OF TECHNOLOGY, Shehan Parmar on 04 November 2026

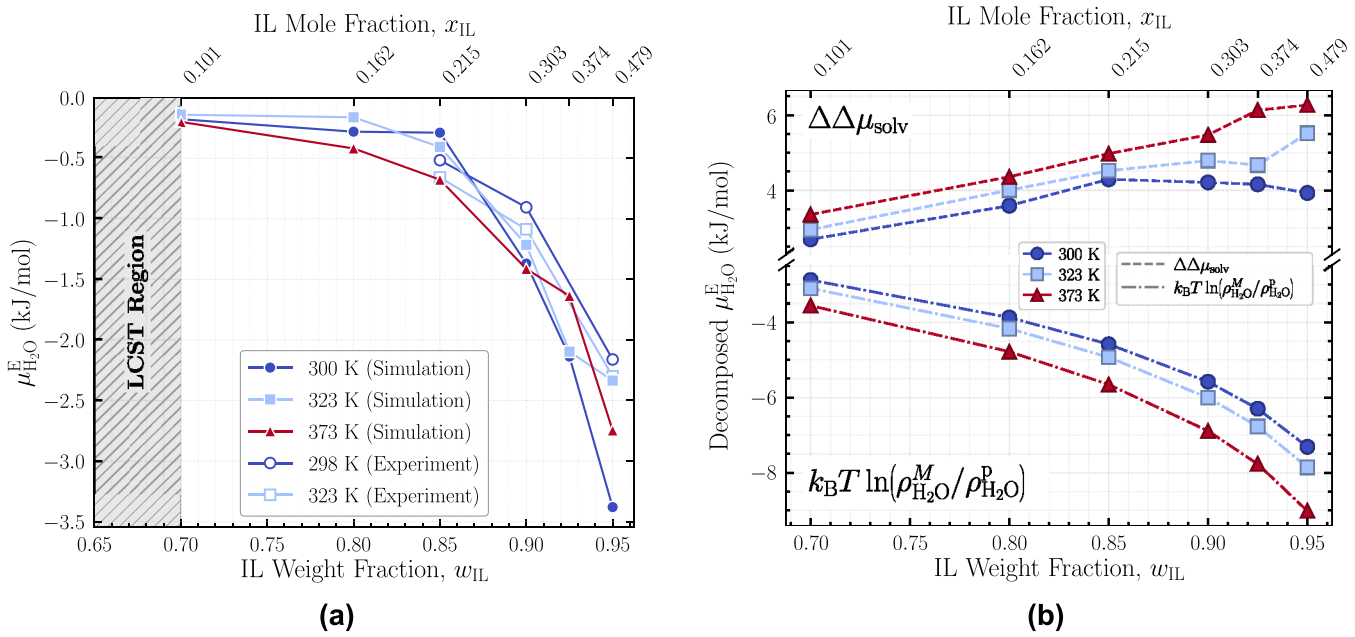


Figure 5. (a) Computational and experimental excess chemical potentials of water, $\mu^{E}_{H_2O}$, in $[P_{4444}][TFA]/H_2O$ mixtures as a function of IL weight fraction (w_{IL}) at varied temperatures. (b) Term-wise decomposition of $\mu^{E}_{H_2O}$ into solvation free energy differences ($\Delta\Delta\mu_{solv}$) and density ratio ($k_BT \ln[\rho^{M}_{H_2O}/\rho^{P}_{H_2O}]$) contributions.

$$s^{E,n.id.}_{H_2O} = \Delta s^{solv}_{H_2O} - k_B \ln\left[\frac{V^{id.}_M}{v^{E}_M + V^{id.}_M}\right] - k_BT\left(\alpha^{id.}_P - \frac{1}{v^{E}_M + V^{id.}_M}\frac{\partial}{\partial T}(v^{E}_M + V^{id.}_M)\right) \quad (20)$$

where v^{E}_M is the excess molar volume, $V^{id.}_M = x_{H_2O}V^{P}_{H_2O} + x_{IL}V^{P}_{IL}$ is the ideal volume of the IL/water mixture, $\alpha^{id.}_P = (1/V^{id.}_M)\partial V^{id.}_M/\partial T$ is the thermal expansion coefficient of the ideal mixture, and $\Delta s^{solv}_{H_2O} = -\partial(\Delta\mu_{solv} - \Delta\mu^{P}_{solv})/\partial T$. Equation 20 highlights two primary contributions to entropy not included in the Flory–Huggins ideal definition: (1) the solvation process, $\Delta s^{solv}_{H_2O}$, and (2) deviations in the accessible volume due to non-ideal mixing (i.e., $v^{E}_M \neq 0$), captured by the last two terms on the right-hand side of eq 20. Practically, the non-ideal entropy is found by $s^{E,n.id.}_{H_2O} = s^{E}_{H_2O} - s^{E,id.}_{H_2O}$.

RESULTS AND DISCUSSION

Water Activity and Osmolality Measurements

Water activity, a_w, quantifies the deviation of the chemical potential from the standard state,[237] i.e., $a_w = 1$ corresponds to the condition where $\mu^{M}_{H_2O} = \mu^{P}_{H_2O}(T, P = 1\ atm)$. Han et al.[238] describe water activity as a "facile technique to represent and understand hydrophobicity of ILs" and as a property linearly correlated with ion–water hydrogen bond basicity. Figure 4a is consistent with general trends that IL/water mixtures with strong ion–water interactions reduce the vapor pressure, and consequently, yield lower water activity values. Moreover, ion–water interactions notably strengthen in the "intermediate" or "hydrated" mole fraction ($x_{IL} \lesssim 0.25$) regime;[238] Figure 4a corroborates this trend, where increasing IL concentrations lead to decreasing water activities, and thus, stronger ion–water interactions. The insets of Figure 4a highlight the temperature dependence of a_w at fixed concentration, which is comparatively modest and concentration-dependent: a_w decreases weakly with temperature at w_{IL} = 85 and 90%, whereas at w_{IL} = 95%, the trend reverses and a_w increases with temperature. Despite this sign change in $\partial a_w/\partial T$, the corresponding experimental $\mu^{E}_{H_2O}$ (eq 10) decreases with temperature at all three concentrations (Table S10), since the k_BT prefactor outweighs the weak activity variation at w_{IL} = 95%.

Osmolality is a primary driver for desalination performance using LCST mixtures—it indicates the effectiveness of $[P_{4444}][TFA]$ as a draw solute for water extraction via forward osmosis.[173] The osmolality is calculated from the measured water activity as $Osm = -\ln(a_w)/M_w$, where M_w is the molar mass of pure water. Figure 4b shows the monotonically increasing osmolality as a function of increasing IL mole fraction, potentially explained by the increase in the number of "free ions" in the solution and hence increased critical temperatures at higher IL concentrations.

Excess Chemical Potential

Computational (eq 9) and experimental (eq 10) excess chemical potentials of water are compared in Figure 5. Of the twenty-one concentrations simulated (Table S1), IL-rich systems (w_{IL} = 80–95%) were selected for TI solvation free energies to provide the greatest contrast between the mixture and pure-water solvation environments, supplemented by an additional point at w_{IL} = 70% to probe the boundary of the LCST region. Across the six matched conditions (w_{IL} = 85–95% at T = 300 and 323 K), simulation and experiment agree with absolute deviations ranging from 0.04 kJ mol^{-1} (at 323 K, w_{IL} = 95%) to 1.2 kJ mol^{-1} (at 300 K, w_{IL} = 95%), across relatively low-magnitude $\mu^{E}_{H_2O}$ values of −0.3 to −3.4 kJ mol^{-1}. Concentration-dependent $\mu^{E}_{H_2O}$ trends are consistent between simulation and experiment, where increased magnitudes at higher IL weight fractions reflect progressively greater departures from ideal water solvation.

Downloaded from pubs.acs.org/jpcbfk/article-pdf/doi/10.1021/acs.jpcb.6c04599/6906150/acs.jpcb.6c04599.pdf by GEORGIA INST OF TECHNOLOGY, Shehan Parmar on 04 November 2026

https://doi.org/10.1021/acs.jpcb.6c04599
J. Phys. Chem. B XXXX, XXX, XXX–XXX

In the absence of the corrective vibrational partition function (the third term in eq 9, neglected in this work), simulations are expected to yield, at best, slightly more negative $\mu^{E}_{H_2O}$ by ∼1 kJ mol^{-1} compared to experiment based on the estimated zero-point frequency shifts for water hydroxyl stretches in IL environments.[221] This magnitude shift is most likely to be observed near the pure IL limit, and will be smaller at increasing water content as more water dimers and trimers are formed. Figure 5 indeed reveals slightly *more* negative $\mu^{E}_{H_2O}$ values compared to the experiment at w_{IL} = 90 and 95%, the magnitude of which is further attributable to the trade-off made between computational cost and sampling fidelity in the TI simulations. Two sources of uncertainty govern the solvation free energy simulations: the number of water solute molecules sampled per distribution, N_{SLT}, and the TI integration time scale, τ (per term in eq S7), over independent TI simulations. As demonstrated by the convergence study in Figure S4 (performed at 300 K and w_{IL} = 85%), the mean solvation free energy varies by up to ∼7 kJ mol^{-1} across τ = 10^{-4}−10^{1} ns (at fixed N_{SLT} = 100), whereas it varies by only ∼1 kJ mol^{-1} across N_{SLT} = 10−50 (at fixed $\tau \approx$ 1 ns).

Thus, for a given water solute molecule, the characteristic diffusion time scales are predominantly coupled to the elevated viscosities of the IL-rich phase. At w_{IL} = 90%, [P_{4444}][TFA]/H_2O has a viscosity of ∼35 mPa s;[51,239] at room temperature, the neat IL solidifies. Table S4 summarizes τ, defined by the time at which $\sqrt{MSD}$ = 5 Å, with the MSD averaged over all atoms in the mixture (Figure S3). For the $\mu^{E}_{H_2O}$ simulations in Figure 5, τ spans multiple orders of magnitude—from 0.03 ns at 373 K and w_{IL} = 70% to ∼50 ns at 300 K and w_{IL} = 95%. Consequently, the deviation between computational and experimental $\mu^{E}_{H_2O}$ increases at higher IL weight fractions. Nonetheless, even in the least diffusive system ($\tau \approx$ 50 ns at w_{IL} = 95%, T = 300 K), agreement remains within ∼1.2 kJ mol^{-1}.

The molecular thermodynamics of water solvation in [P_{4444}][TFA]/H_2O is not completely resolved through the excess chemical potential trends alone. In particular, the non-monotonic temperature dependence of $\mu^{E}_{H_2O}$ (e.g., −3.38, −2.34, and −2.75 kJ mol^{-1} at w_{IL} = 95% for 300, 323, and 373 K, respectively) is most naturally rationalized by decomposing $\mu^{E}_{H_2O}$ into two competing, monotonic contributions. Whereas this comparatively large w_{IL} = 95% variation is plausibly physical, the much weaker non-monotonicity at w_{IL} = 80% (−0.28, −0.16, and −0.42 kJ mol^{-1} over the same temperatures) lies within the solute-sampling uncertainty (Figure S4) and is more plausibly a statistical artifact. Figure 5b includes the decomposition of $\mu^{E}_{H_2O}$ (eq 9) into the solvation free energy difference, $\Delta\Delta\mu_{solv} = \Delta\mu_{solv} - \Delta\mu^{p}_{solv}$, and the density ratio term, $k_BT \ln[\rho^{M}_{H_2O}/\rho^{p}_{H_2O}]$, the latter arising from the liberation and assimilation contributions to the chemical potential in eq 9.[210] The density ratio, expressed in terms of the pure component molar volumes, V^{p}_{i}, and excess molar volume, v^{E}_{M},

$$\frac{\rho^{M}_{H_2O}}{\rho^{p}_{H_2O}} = \frac{x_{H_2O}V^{p}_{H_2O}}{v^{E}_{M} + x_{H_2O}V^{p}_{H_2O} + x_{IL}V^{p}_{IL}} \quad (21)$$

is governed by the large ideal volume ratio between the [P_{4444}][TFA] ion pair and water, $V^{p}_{IL}/V^{p}_{H_2O} \approx$ 19 at 300 K. Based on the sensitivity analysis in Figure S5b, the excess molar volume contributes to the overall density ratio free energy by ±0.2 kJ mol^{-1} over an observed range of v^{E}_{M} = −2 to +1 cm^3 mol^{-1} across all concentrations (Figure S5a). Moreover, the density ratio itself is largely constant across temperatures at constant concentration (Table S9), indicating that the density ratio's contribution to the overall free energy is predominantly entropic. In its entirety, the density-ratio term is hence largely composed of the commonly referenced ideal entropy of mixing term, $k_BT \ln \varphi_{H_2O}$ (eq 19), which, by construction, is identical across simulation and experiment (insofar as the pure component molar volumes are accurate, as we show in Table S3 for pure IL density comparisons). Consequently, the close agreement between simulation and experiment observed in Figure 5a is principally a manifestation of agreement in the solvation free energy difference, $\Delta\Delta\mu_{solv}$.

Relative to the solvation free energy difference, $\Delta\Delta\mu_{solv}$, the density ratio term exerts a greater influence on the overall concentration dependence of $\mu^{E}_{H_2O}$, decreasing by approximately a factor of two across the IL-rich concentrations while $\Delta\Delta\mu_{solv}$ increases by only ∼1.5 kJ mol^{-1} over the same range. Intuitively, this behavior is expected since the density-ratio term diverges to $-\infty$ as $\rho^{M}_{H_2O} \to 0$ in the dilute limit. In analogous contexts at finite densities, Ben-Naim and Marcus[240] showed that density ratios in hydrocarbon transfer between water and pure hydrocarbon yield comparable contributions to the solvation free energy itself, e.g., $RT \ln(130/18) \approx$ 4.9 kJ mol^{-1} for water/hexane and $RT \ln(291/18) \approx$ 6.9 kJ mol^{-1} for water/hexadecane. Similarly, Nishikawa and others[66,241] demonstrated that density fluctuations derived from number-density structure factors in [P_{4444}][TFA]/H_2O are approximately six-fold greater than in acetonitrile/H_2O, in part due to the disparate molar volume ratios ($V^{p}_{ACN}/V^{p}_{H_2O} \approx$ 3 versus ∼19 for [P_{4444}][TFA]/H_2O).

The density ratio contributions are partially counterbalanced by positive $\Delta\Delta\mu_{solv}$ values, ranging from +2.7 to +6.3 kJ mol^{-1} across all temperatures and concentrations (Figure 5b). The solvation free energy difference is computed relative to the self-solvation free energy of water in pure TIP3P, $\Delta\mu^{p}_{solv}$ = −25.4 kJ mol^{-1} at 300 K, consistent with TIP3P benchmarks (−25.5 kJ mol^{-1} at 298 K)[217] and the experimental value (−26.5 kJ mol^{-1} at 298 K).[240,242] Like the density ratio, $\Delta\Delta\mu_{solv}$ is modulated by both temperature and concentration: between 300 and 373 K, $\Delta\Delta\mu_{solv}$ increases by approximately 1−2 kJ mol^{-1} at a given concentration, and by a comparable ∼1−3 kJ mol^{-1} with increasing IL weight fraction (across the entire concentration range) at a given temperature. As will be discussed in the following section, $\Delta\Delta\mu_{solv}$ is a manifestation of the average in eq 4, in which the nanostructural heterogeneity of [P_{4444}][TFA]/H_2O governs water solvation thermodynamics. Taken together, the temperature dependence of $\mu^{E}_{H_2O}$ cannot be interpreted without the decomposed contributions from $\Delta\Delta\mu_{solv}$ and $k_BT \ln[\rho^{M}_{H_2O}/\rho^{p}_{H_2O}]$, which each encompass larger-magnitude contributions than $\mu^{E}_{H_2O}$ itself. Whether the resulting non-monotonicity is physically meaningful or a statistical artifact of the highly viscous 300 K [P_{4444}][TFA] system is later rationalized through the excess partial molar enthalpy and entropy (*vide infra*): via eq 12 and the relationship between the partial molar enthalpy and entropy temperature derivatives, much of the $\mu^{E}_{H_2O}$ temperature

Downloaded from pubs.acs.org/jpcbfk/article-pdf/doi/10.1021/acs.jpcb.6c04599/6906150/acs.jpcb.6c04599.pdf by GEORGIA INST OF TECHNOLOGY, Shehan Parmar on 04 November 2026

https://doi.org/10.1021/acs.jpcb.6c04599
J. Phys. Chem. B XXXX, XXX, XXX−XXX

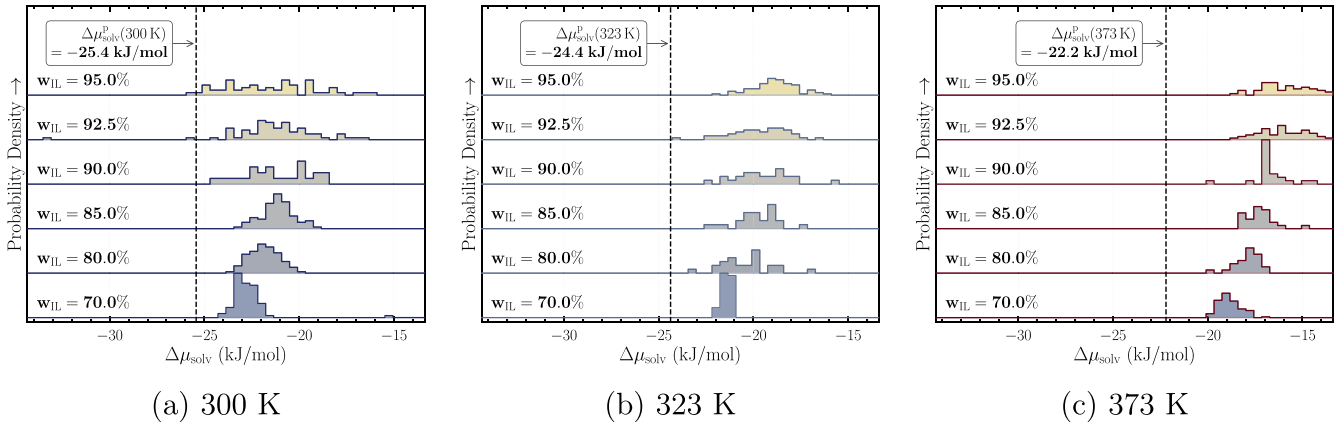


Figure 6. Temperature-dependent solvation free energy distributions, $\Delta\mu_{solv}$, derived from thermodynamic integration (TI) simulations for water in $[P_{4444}][TFA]/H_2O$ mixtures at varied IL weight fractions. Dashed vertical lines indicate the solvation free energy of water in pure water, $\Delta\mu^{p}_{solv}(T, P = 1\ atm)$, at each temperature.

dependence remains consistent, whereas certain conditions (e.g., w_{IL} = 80%) exhibit a non-monotonicity more likely originating from statistical noise.

Solvation Free Energies and Microenvironment Characterization

Traditionally, solvation thermodynamics is studied through the lens of the excess chemical potential at the infinite dilution limit, i.e., the solvation Gibbs energy of a single water molecule in the neat ionic liquid, where $k_BT\ \ln[\rho^{M}_{H_2O}/\rho^{p}_{H_2O}] \rightarrow -\infty$. Figure S6 shows the temperature-dependent solvation free energies of a single water solute in neat $[P_{4444}][TFA]$ alongside the pure water self-solvation reference. The resulting $\Delta\Delta\mu_{solv}$ at infinite dilution (Figure S6b) is +0.7 ± 3.9 kJ mol^{-1} at 300 K, +3.1 ± 3.2 kJ mol^{-1} at 323 K, and +6.4 ± 0.6 kJ mol^{-1} at 373 K. The large statistical uncertainties at 300 and 323 K reflect insufficient sampling of $[P_{4444}][TFA]$ in its most viscous regime, even at the longest sampling times employed in this work ($\tau \approx 9$ ns); convergence studies (Figure S4) suggest these values systematically underestimate the ergodic solvation free energy. Nonetheless, the qualitative trend of increasingly unfavorable water solvation with temperature remains robust across all three temperatures.

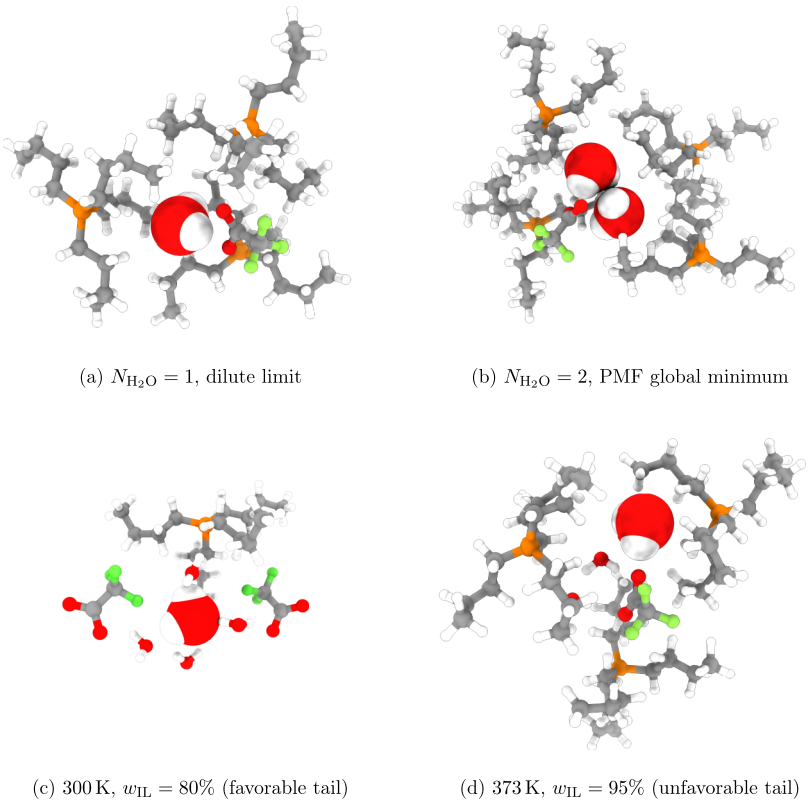
When placed in context with a broader spectrum of water solvation in various ionic liquid/water mixtures, these $\Delta\Delta\mu_{solv}$ values indicate intermediate solvation situated between hydrophilic and hydrophobic systems. On one extreme, strong anion−water hydrogen bonding in chloride-based ILs drives favorable water solvation; e.g., Lynden−Bell et al.[157] report $\Delta\Delta\mu_{solv} \approx -7$ kJ mol^{-1} for water in [dmim][Cl] at 400 K. Both experimental and computational studies have shown that structural modifications to the anion significantly modulate water solvation: for imidazolium-based ILs, $\Delta\Delta\mu_{solv}$ spans approximately −2 to +11 kJ mol^{-1}, following a trend governed by anion identity ($FSI^- < NO_3^- \lesssim OTf^- < BF_4^- < TFSI^- < PF_6^-$).[79,80,151,157] Thus, while the TFA^- anion favors strong water−anion interactions, the hydrophobic $-CF_3$ group and the large P_{4444}^+ cation simultaneously counteract this favorability, resulting in $\Delta\Delta\mu_{solv}$ values that fall within a range of hydrophilic and hydrophobic ILs. However, single-solute solvation free energies are inherently insufficient for interpreting concentration-dependent phase behavior of IL/water mixtures, as they probe only the most thermodynamically favorable water−ion coordination environments at infinite dilution. As McDaniel and Verma[80] highlight, such a property only partially discriminates between hydrophilic and hydrophobic ionic liquids. [BMIM][FSI] is one notable example: the single-water solvation free energy ($\Delta\Delta\mu_{solv} \approx -2$ kJ mol^{-1})[80] does not reflect the immiscibility of [BMIM][FSI] with water but rather its hygroscopic nature, where favorable ∼1.8 Å $O_w-H_w\cdots O_{FSI}$ hydrogen bonds between water and FSI^- sulfonyl oxygen atoms create optimal adsorption sites.

One approach to move beyond the assumption of complete water dispersion inherent to single-solute solvation free energies[243] is the potential of mean force (PMF), $w(r)$, which quantifies the free energy landscape of separating a water−water dimer in the bulk ionic liquid. As shown in Figure S7, the water−water PMF in neat $[P_{4444}][TFA]$ at 300 K exhibits a global minimum of −17.6 kJ mol^{-1} at a center-of-mass separation of $r \approx 2.8$ Å, indicative of an energetically favorable hydrogen bond. The depth of this minimum is semiquantitatively consistent with water−water PMFs reported by Wang et al.[243] in $[P_{6,6,6,14}]$−orthoborate ILs, where the close-contact water dimer was identified as the most energetically favorable configuration. Beyond the global minimum, oscillating local minima provide the first direct indication of more complex interactions between water and neighboring ionic species that give rise to structural heterogeneity. The local minimum at $r \approx 5.0$ Å corresponds to a water−anion−water structural motif in which the water dimer is bridged by a single, shared oxygen atom of the COO^- group of a planar TFA^- anion. At larger separations ($r \approx 7$ Å), broader and shallower local minima indicate less distinct structural motifs arising from (1) water−anion−water configurations in which the dimer is separated by COO^- involving both oxygen atoms, or (2) separation via hydrophobic CF_3 and cationic alkyl groups, as the water molecules progressively associate into separate solvation shells. At longer range, these oscillations attenuate as ionic species screen the effective water−water interaction.

While the single-solute solvation free energy ($N_{H_2O} = 1$) indicates that incorporating water into the $[P_{4444}][TFA]$ ion network is unfavorable relative to bulk water (noting that unfavorable solvation does not preclude water uptake, which is always driven by the divergent ideal mixing entropy at low concentrations), the water−water PMF ($N_{H_2O} = 2$) demon-

Downloaded from pubs.acs.org/jpcbfk/article-pdf/doi/10.1021/acs.jpcb.6c04599/6906150/acs.jpcb.6c04599.pdf by GEORGIA INST OF TECHNOLOGY, Shehan Parmar on 04 November 2026

https://doi.org/10.1021/acs.jpcb.6c04599
J. Phys. Chem. B XXXX, XXX, XXX−XXX



(a) $N_{H_2O} = 1$, dilute limit (b) $N_{H_2O} = 2$, PMF global minimum

(c) 300 K, $w_{IL} = 80\%$ (favorable tail) (d) 373 K, $w_{IL} = 95\%$ (unfavorable tail)

Figure 7. Representative solvation microenvironments for water in $[P_{4444}][TFA]/H_2O$ mixtures from the dilute limit to finite concentration. (a) Single water molecule (N_{H_2O} = 1) in neat $[P_{4444}][TFA]$. (b) Water−water dimer at the PMF global minimum ($r \approx 2.8$ Å). (c) Solvation environment ($\Delta\Delta\mu_{solv}$ = +1.8 kJ mol^{-1}) from the left tail of the TI distribution at 300 K and w_{IL} = 80%. (d) Unfavorable solvation environment ($\Delta\Delta\mu_{solv}$ = +8.7 kJ mol^{-1}) from the right tail at 373 K and w_{IL} = 95%. The selected water solute is displayed with van der Waals spheres.

strates that this penalty is partially offset by cooperative[243] pairwise interactions. At finite concentration—where N_{H_2O} = 217, 335, 459, 729, 1033, and 1772 for w_{IL} = 95, 92.5, 90, 85, 80, and 70%, respectively—the microsolvation landscape is considerably more complex. Two-body cooperativity evolves into preferential, multi-body interactions among water molecules competing for favorable coordination environments within the ion Coulomb matrix. The multi-solute TI distributions in Figure 6 reveal the thermodynamic manifestation of microsolvation heterogeneity—at each temperature and concentration, individual water solvation free energies range from as narrow as $\Delta\mu_{solv} \in [-22.1, -20.9]$ kJ mol^{-1} (at w_{IL} = 70%, 323 K) to as wide as $\Delta\mu_{solv} \in [-33.3, -16.7]$ kJ mol^{-1} (at w_{IL} = 92.5%, 300 K), reflecting the breadth of coordination environments accessible within the $[P_{4444}][TFA]/H_2O$ mixture. Across all conditions, the distributions are generally shifted to less negative free energies relative to the pure water reference ($\Delta\Delta\mu_{solv} > 0$; Table S6). With increasing water content at a given temperature, the mean $\Delta\mu_{solv}$ shifts by ∼1−3 kJ mol^{-1} toward the pure water reference across the w_{IL} = 70−95% range, as water−water coordination increasingly competes with water−anion interactions. The concentration dependence of water solvation is governed not only by local coordination motifs but also by long-range electrostatic features corroborated by charge−correlation structure factors (*vide infra*). Temperature modulates absolute solvation more subtly. At a given concentration, the mean $\Delta\mu_{solv}$ increases monotonically by ∼5 kJ mol^{-1} from 300 to 373 K, compared to ∼3 kJ mol^{-1} for pure water over the same range. For the three-stage decoupling path employed in this work (electrostatic → van der Waals → soft-core repulsion; Section S5), favorable electrostatic contributions dominate $\Delta\mu_{solv}$ at all conditions (Figure S10), while the van der Waals/repulsive contribution is comparatively modest and less sensitive to both concentration and temperature. As such component decompositions are path-dependent,[244] these trends should be interpreted qualitatively.

As will be discussed through radial distribution functions and coordination numbers, the TI distributions sample transient yet representative solvation structures that collectively define the free energy landscape of water in $[P_{4444}][TFA]$. Near the dilute limit, non-ideal solvation is mediated by a hydrogen-bonded water−anion structural motif (Figure 7a). Unlike the persistent anion−water−anion bridge detected spectroscopically for common room-temperature ionic liquid anions (e.g., BF_4^-, PF_6^-, ClO_4^-, and $TFSI^-$),[122] the O−H···COO^- coordination is reminiscent of the bidentate motif found in similar carboxylate−water[245] and $[BMIM][TFA]/H_2O$[246] systems. The water−water hydrogen-bonded dimer (Figure 7b), corresponding to the global minimum of the PMF, is accessed only through enhanced sampling at the dilute limit; at finite concentration, such close-contact dimers are embedded within and modulated by the surrounding ionic environment. Beyond these idealized cases, the solvation microenvironments at finite concentration are structurally diverse. Representative configurations drawn from opposing extremes of the TI distributions—the left-most tail at 300 K and w_{IL} = 80% (Figure 7c) and the unfavorable tail at 373 K and w_{IL} = 95% (Figure 7d)—illustrate the subtle, competitive interplay between water−water and water−anion coordination

https://doi.org/10.1021/acs.jpcb.6c04599
J. Phys. Chem. B XXXX, XXX, XXX−XXX

Downloaded from pubs.acs.org/jpcbfk/article-pdf/doi/10.1021/acs.jpcb.6c04599/6906150/acs.jpcb.6c04599.pdf by GEORGIA INST OF TECHNOLOGY, Shehan Parmar on 04 November 2026

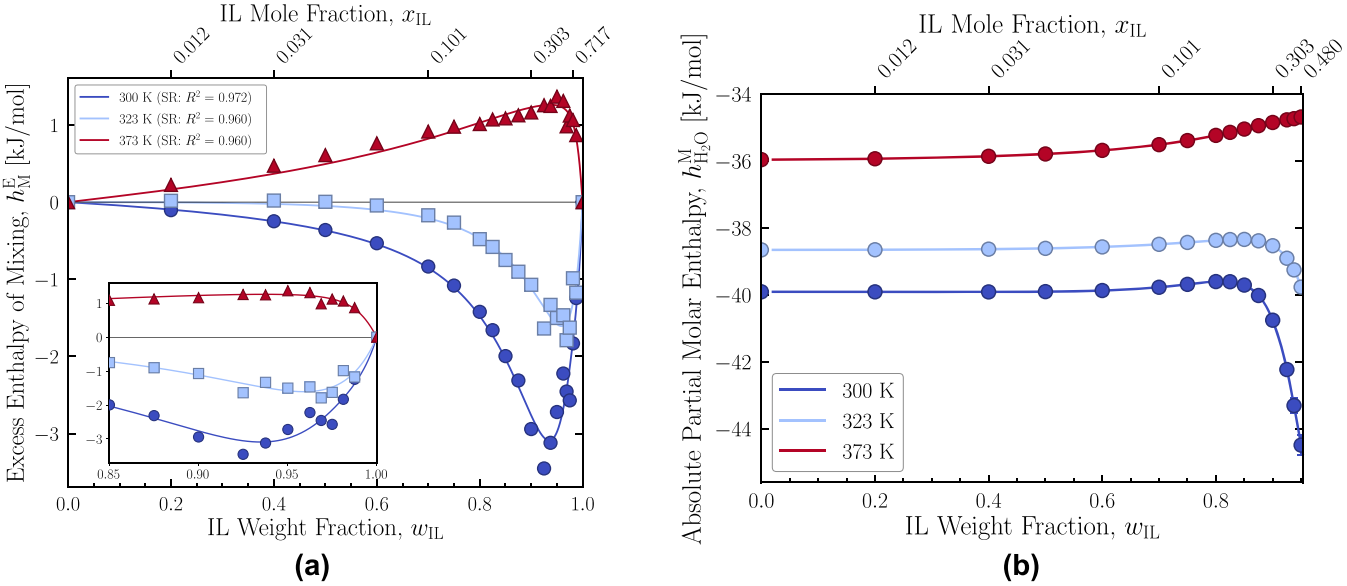


Figure 8. (a) Simulated excess enthalpies of mixing, h^E_M, as a function of IL weight fraction (w_{IL}) at varied temperatures with symbolic regression (SR) fit curves; SEM bounds on h^E_M (omitted for clarity) are below ∼0.15 kJ mol^{-1} (<6% of plotted values) across the studied phase space. (b) Absolute partial molar enthalpies of water, $h^M_{H_2O}$, derived from the fitted excess enthalpy of mixing via eq S14. Uncertainties in $h^M_{H_2O}$ are obtained from a parametric bootstrap (SI).

that underpins the breadth of the TI distributions and motivates the structural analysis presented in the following sections.

Enthalpy and Entropy Decomposition

While cumulative non-idealities are captured by excess chemical potentials and solvation free energies, macroscopic phase behavior reflects molecular driving forces shaped by tightly coupled enthalpy−entropy compensation. Miscibility, for instance, is rarely rationalized through either enthalpic or entropic arguments alone. NaCl is water-soluble with an endothermic dissolution enthalpy (ΔH°_{soln} = +3.6 kJ mol^{-1}), whereas $CaCO_3$ is highly insoluble despite an exothermic one (ΔH°_{soln} = −11.3 kJ mol^{-1}).[247,248] Although these enthalpies arise from the near-cancellation of large-magnitude crystal lattice dissociation energies (+790 kJ mol^{-1} for NaCl) and ion hydration enthalpies (−786 kJ mol^{-1} for Na^+ and Cl^-),[247,248] entropic contributions (themselves governed by ion charge density, shape, and the resulting solvation structure) dictate the observed phase behavior.[114,116,248] Similarly, although oil and water are immiscible at room temperature, transferring nonpolar solutes such as methane from organic solvent to water at 298 K is exothermic (ΔH_{soln} = −10.5 kJ mol^{-1}), where phase separation is driven instead by the entropic penalty of hydrophobic effects ($-T\Delta S_{soln}$ > +22 kJ mol^{-1}).[81,116,249] Moreover, enthalpy and entropy are coupled through the constant-pressure heat capacity,

$$C^M_{p,H_2O} = \left(\frac{\partial h^M_{H_2O}}{\partial T}\right)_P = T\left(\frac{\partial s^M_{H_2O}}{\partial T}\right)_P \quad (22)$$

such that temperature dependence in one is necessarily encoded in the other (rooted microscopically in energy fluctuations), a feature especially relevant for understanding LCST systems.[249,250]

For [P_{4444}][TFA] specifically, the cohesive energy of ∼−544 kJ mol^{-1} per ion pair at 300 K (Figure S11) is larger (in magnitude) than typical imidazolium BF_4^- salts (from −495 to −462 kJ mol^{-1}),[75] slightly higher (in magnitude) than [EMIM][TFA] (∼−520 kJ mol^{-1}), and comparable to that of [N_{1888}][TFSI] at ∼−553 kJ mol^{-1}. The high cohesion reflects both strong Coulombic ion−ion interactions and increased van der Waals attraction accompanying long alkyl substituents on tetraalkyl cations.[251] Moreover, the ions *individually* present another large energetic scale upon water solvation (Figure S12), where the hydrophilic TFA^- anion has a highly favorable simulated solvation free energy of ∼−330 kJ mol^{-1}, while the bulky P_{4444}^+ cation is comparatively weakly hydrated at ∼−93 kJ mol^{-1}. While direct subtraction across these two quantities is not rigorous (the cohesive energy is entirely enthalpic, whereas the simulated ion solvation free energies contain both enthalpic and entropic contributions), the partial molar quantities reported herein are expected to exhibit small residual differences between such high-magnitude scales.

The excess enthalpy of mixing, h^E_M, was computed from equilibrium MD via eq 15 across the full concentration window at 300, 323, and 373 K (Figure 8a), with standard error of the mean (SEM) bounds below ±0.15 kJ mol^{-1}. The partial molar enthalpy of water in the [P_{4444}][TFA]/H_2O mixture, $h^M_{H_2O}$, follows from h^E_M via eq 14, which requires an analytical derivative of the fitted curve with respect to IL mole fraction, $\partial h^E_M/\partial x_{IL}$ (Figure 8b). Historically, analytical forms used to fit excess functions follow classical models founded on regular-solution assumptions. As highlighted by Kelkar, Shi, and Maginn,[252] however, partial molar enthalpies are sensitive to the choice of fit, especially in the IL-rich regime. To address these limitations, curve fits were obtained via symbolic regression (SR), which discovers an analytic expression that optimizes over both accuracy and complexity by searching the functional space directly, without committing to a fixed parametric form *a priori*; full procedural details and bootstrap-based uncertainty quantification are provided in the SI. We adopt the SR-discovered expression as the best analytic representation, selected via PySR's[253] score-based criterion

Downloaded from pubs.acs.org/jpcbfk/article-pdf/doi/10.1021/acs.jpcb.6c04599/6906150/acs.jpcb.6c04599.pdf by GEORGIA INST OF TECHNOLOGY, Shehan Parmar on 04 November 2026

https://doi.org/10.1021/acs.jpcb.6c04599
J. Phys. Chem. B XXXX, XXX, XXX−XXX

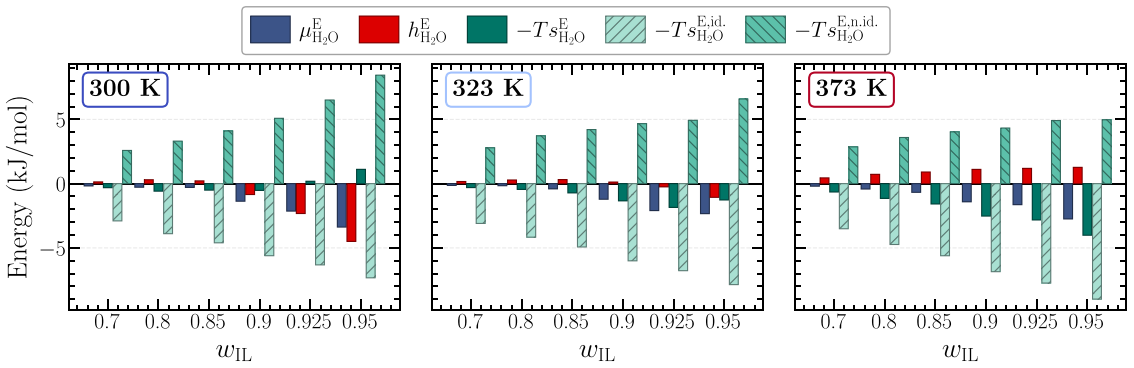


Figure 9. Decomposition of the excess chemical potential of water, $\mu^{E}_{H_2O}$, into excess partial molar enthalpy ($h^{E}_{H_2O}$), ideal entropy ($-Ts^{E,id.}_{H_2O}$), and non-ideal entropy ($-Ts^{E,n.id.}_{H_2O}$) contributions at varied temperatures and IL weight fractions.

that balances fit accuracy against expression complexity along the Pareto front (augmented by a second-derivative roughness penalty in the loss function to suppress fits with unstable gradients). Compared to traditional analytical forms (e.g., Redlich−Kister, van Laar, polynomial expansions), SR yields reasonable agreement, deviating by up to 0.9 kJ mol^{-1} at lower IL concentrations (w_{IL} = 85%) and 1.4 kJ mol^{-1} at the highest, IL-rich concentrations (w_{IL} = 95%). As summarized in Table S7 and Figures S13−S14, the SR-derived partial molar enthalpies are sufficiently robust that the enthalpy/entropy decomposition interpretation is largely insensitive to the choice of functional form. At x_{IL} = 0 (pure water) and 300 K, $h^{M}_{H_2O}$ converges to −39.91 kJ mol^{-1}, corresponding to a heat of vaporization $\Delta H_{vap} = -h^{M}_{H_2O}(x_{IL} = 0) + RT \approx 39.91 + 2.49 \approx 42.40$ kJ mol^{-1}, in close agreement with the literature TIP3P value (42.22 kJ mol^{-1}),[217] further validating the procedure in the water-rich regime. Similarly, the excess partial molar enthalpy of water at infinite dilution in the ionic liquid, $h^{E,\infty}_{H_2O} \equiv \lim_{x_{IL}\to 1} h^{E}_{H_2O}$ = −8.0 ± 0.8 kJ mol^{-1} at 300 K from the symbolic regression fit, is in the same, semiquantitative exothermic regime as the experimental value of −3.9 ± 0.1 kJ mol^{-1} reported by Khan over 328−393 K for the [BMIM][TFA]/H_2O system.[25]

The most striking feature of $h^{E}_{M}(x_{IL}, T)$ for [P_{4444}][TFA]/H_2O is a strong temperature dependence (Figure 8a): across the studied concentration window, h^{E}_{M} shifts by ∼5 kJ mol^{-1} between 300 and 373 K. This magnitude shift exceeds the typical range across the 194 binary systems reviewed by Podgoršek et al.[254] More notably, the shift drives h^{E}_{M} from exothermic to endothermic at high w_{IL}, a temperature-induced sign change with little reported precedent for IL/water mixtures. Sign changes in h^{E}_{M} typically require altering the ion molecular structure, e.g., [EMIM][CF_3SO_3]/H_2O mixes endothermically while [EMIM][CH_3SO_3]/H_2O mixes exothermically.[177,255] While rare, some IL/water mixtures have been reported to exhibit concentration-dependent sign changes at fixed temperature (e.g., [EMIM][SCN]/H_2O).[256]

Excess enthalpies of mixing are typically rationalized in terms of the relative strengths of unlike (water−IL) and like (water−water, ion−ion) species interactions.[177,257] Near room temperature, the exothermic h^{E}_{M} observed for [P_{4444}][TFA]/H_2O reflects the dominance of TFA^{-}−H_2O hydrogen bonding. Unsurprisingly, [EMIM][TFA]/H_2O is also exothermic and fully water-miscible across the entire concentration window over 313−348 K, with its less hydrophobic and smaller $EMIM^{+}$ cation. For supplemental comparison, we use the same OPLS-AA/TIP3P force fields to simulate [EMIM][TFA]/H_2O, reproducing the temperature-dependent trends in Ficke et al.'s[177] calorimetric data (despite well-documented deviations in absolute mixing enthalpies between classical force field simulations and experiment[252,258]). As shown in Figure S15, h^{E}_{M} for [EMIM][TFA]/H_2O remains negative across the full concentration window at all studied temperatures, with the peak h^{E}_{M} at 300 and 373 K differing by only ∼1 kJ mol^{-1}, in contrast to the ∼5 kJ mol^{-1} difference in [P_{4444}][TFA]/H_2O over the same range.

Quantitatively, the temperature dependence is most apparent in the IL-rich regime, where $h^{E}_{H_2O}$ at w_{IL} = 95% transitions from −4.5 ± 0.3 kJ mol^{-1} at 300 K, to −1.1 ± 0.2 kJ mol^{-1} at 323 K, and inverts to +1.3 ± 0.1 kJ mol^{-1} at 373 K. At elevated temperatures, like-species interactions (water−water, ion−ion) increasingly dominate as water−anion contacts diminish. The temperature derivative of h^{E}_{M} yields a maximum excess heat capacity of $c_p^{E,max} \approx$ +65 J K^{-1} mol^{-1} for [P_{4444}][TFA]/H_2O (at w_{IL} = 92.5%), several-fold larger than the ∼+15 J K^{-1} mol^{-1} value computed for [EMIM][TFA]/H_2O (consistent with the calorimetric value of +13.8 J K^{-1} mol^{-1} ref[177]) and well above the (−15, +24) J K^{-1} mol^{-1} range documented across IL/water systems,[259] indicating an unusually strong structural sensitivity of [P_{4444}][TFA]/H_2O to temperature in the IL-rich regime. As will be shown in the following sections, the charge−charge structure factor $S_{ZZ}(\mathbf{k})$ reveals a concomitant temperature modulation absent in [EMIM][TFA]/H_2O.

The minimum in h^{E}_{M} near $w_{IL} \approx$ 92.5% at 300 K likewise reflects the onset of water self-association. Near neat IL concentrations (w_{IL} > 92.5%), water is dispersed and essentially monomeric. The gradual increase in water concentration drives a rapid deepening of h^{E}_{M} at 300 K, directly accounted for by water forming strongly hydrogen-bonded dimers and small clusters, as corroborated by the deep, favorable minimum in the water−water PMF (Figure S7). The concentration-dependent h^{E}_{M} minima and maxima further coincide with both the fragmentation of the IL polar network and the crossover from water−anion to water−water coordination, as elucidated by RDFs, coordination numbers, and water aggregation analyses (*vide infra*).

To complete the thermodynamic picture, we pair the partial molar enthalpy trends with ideal and non-ideal partial molar entropies by eqs 19 and 20. At x_{IL} = 0 (pure water) and 300 K, the simulated TIP3P self-solvation entropy, $-T\Delta s^{P}_{solv}$ = +14.8

https://doi.org/10.1021/acs.jpcb.6c04599
J. Phys. Chem. B XXXX, XXX, XXX−XXX

Downloaded from pubs.acs.org/jpcbfk/article-pdf/doi/10.1021/acs.jpcb.6c04599/6906150/acs.jpcb.6c04599.pdf by GEORGIA INST OF TECHNOLOGY, Shehan Parmar on 04 November 2026

kJ mol^{-1}, agrees within ∼3 % with the experimental value of +15.3 kJ mol^{-1} at 298 K reported by Ben−Naim and Marcus.[240] Table S5 further includes the water self-solvation enthalpy and entropy at all simulated temperatures. As shown in Figure 9, the excess non-ideal solvation entropy, $-Ts^{E,n.id.}_{H_2O}$, varies in magnitude from +2.58 kJ mol^{-1} at the most water-rich condition to +8.44 kJ mol^{-1} at the most IL-rich condition (300 K). These convert to absolute solvation entropies, $-T\Delta s_{solv}$, in the range +17.4 kJ mol^{-1}−23.2 kJ mol^{-1}, providing semi-quantitative comparisons to solvation entropies found in the literature. Consequently, water solvation in $[P_{4444}][TFA]/H_2O$ is comparable in entropic cost to Wan, Stote, and Karplus's benchmark of methylamine in pure water (∼+22 kJ mol^{-1} ref[229]), i.e., the cost of dehydrating a small polar molecule from bulk water. While solvation entropy data for water in ionic liquids remains sparse and not uniformly characterized across the IL family, the values reported in Figure 9 are within a reasonable order of magnitude of partial molar entropies reported for water in both miscible and immiscible IL systems.[260−262] Evidently, across the entire studied concentration and temperature phase space, the non-ideal solvation entropy of water, $-Ts^{E,n.id.}_{H_2O}$, in $[P_{4444}][TFA]/H_2O$ opposes mixing.

The concentration dependence of the non-ideal solvation entropy of water is most evident at 300 K. The entropic penalty, $-Ts^{E,n.id.}_{H_2O}$, rises by over a factor of three across the studied concentrations, from +2.58 kJ mol^{-1} at w_{IL} = 70% to +8.44 kJ mol^{-1} at w_{IL} = 95% (the first panel in Figure 9). Physically, the entropic cost of inserting a water molecule reflects the work of opening a cavity within the ion Coulombic network,[263,264] a network that becomes most compact and cohesive at high IL weight fraction and low temperature. As will be shown in later sections, the IL-rich regime is delineated by $w_{IL} \approx 87.5\%$, after which the mixture transitions from predominantly water−water coordination to water−anion (and even anion−water−anion bridge) coordination. While $TFA^{-}\cdots H_2O$ interactions may be enthalpically favorable, the associated entropic penalty can be traced to the significant structural organization uniquely imposed by the P_{4444}^{+} cation; in the following section, spatial distribution functions (SDFs) reveal a stark contrast in water arrangement relative to the fully water-miscible [EMIM][TFA] analogue.

The temperature dependence, by contrast, is best understood by separating the temperature contribution itself from $s^{E,n.id.}_{H_2O}$. At w_{IL} = 70%, $s^{E,n.id.}_{H_2O}$ is essentially constant at ∼−8 J K^{-1} mol^{-1} across 300−373 K, and thus $-Ts^{E,n.id.}_{H_2O}$ varies modestly by <0.3 kJ mol^{-1}; at w_{IL} = 80%, the variation is still small (<1 kJ mol^{-1}). At w_{IL} = 95%, $s^{E,n.id.}_{H_2O}$ decreases in magnitude from −28 J K^{-1} mol^{-1} at 300 K to −13 J K^{-1} mol^{-1} at 373 K; $-Ts^{E,n.id.}_{H_2O}$ correspondingly decreases by ∼3.5 kJ mol^{-1}. That is, the solvation entropy ($-Ts^{E,n.id.}_{H_2O}$) is most sensitive to temperature at w_{IL} = 95%, precisely where $h^{E}_{H_2O}$ itself undergoes its largest temperature dependence (transitioning from −4.5 kJ mol^{-1} at 300 K to +1.3 kJ mol^{-1} at 373 K). As $h^{E}_{H_2O}$ approaches zero with decreasing IL weight fraction, so does the entropy temperature dependence.

Unlike the non-ideal entropy, the ideal Flory−Huggins entropy (eq 19) generally favors mixing across the studied phase space due to the large molar volume ratio between the IL ions and water. Consequently, the sum (eq 18) yields a total excess partial molar entropy of water (dark green bar in Figure 9) that exhibits a clear temperature and concentration dependence. Because $s^{E}_{H_2O} = -\partial\mu^{E}_{H_2O}/\partial T$ (eq 12), the sign of the total excess entropy should be consistent with the temperature slope of $\mu^{E}_{H_2O}$. Near the dilute water limit, this consistency is especially apparent: at w_{IL} = 95%, $-Ts^{E}_{H_2O}$ is positive at 300 K ($s^{E}_{H_2O} < 0$), requiring $\partial\mu^{E}_{H_2O}/\partial T > 0$, in line with the rise of $\mu^{E}_{H_2O}$ from −3.4 to −2.3 kJ mol^{-1} between 300 and 323 K, before $s^{E}_{H_2O}$ turns positive and $\mu^{E}_{H_2O}$ decreases again at 373 K. Toward the water-rich concentrations, $s^{E}_{H_2O}$ is small and weakly positive ($\partial\mu^{E}_{H_2O}/\partial T \lesssim 0$), and the underlying $\mu^{E}_{H_2O}$ temperature variation shrinks accordingly; the subtle non-monotonicities apparent in Figure 5a (e.g., w_{IL} = 80%) are therefore likely statistical artifacts, consistent with the solute-sampling (N_{SLT}) scatter quantified in Figure S4. Because $s^{E}_{H_2O}$ itself follows from $h^{E}_{H_2O}$ (eq 11), numerically verifying the excess form of the heat capacity identity (eq 22) is in some ways a restatement of this consistency; as shown in Table S11, it holds for most temperature and concentration combinations. While the temperature dependence of a_w permits an analogous experimental decomposition into $h^{E}_{H_2O}$ and $-Ts^{E}_{H_2O}$ (Table S10 and Figure S16), the resulting values approach the noise floor set by the ±0.003 instrument precision at the 5 K temperature spacings used here; we therefore restrict direct simulation/experiment comparison in this work to $\mu^{E}_{H_2O}$. Even so, the experimental non-ideal entropy mirrors the steeply growing ideal Flory−Huggins term, growing increasingly unfavorable toward the dilute water limit in agreement with the simulated $s^{E,n.id.}_{H_2O}$.

At 300 K, $-Ts^{E}_{H_2O}$ crosses zero between w_{IL} = 90 and 92.5%, transitioning from a favorable contribution to the excess chemical potential at water-rich conditions (−0.31 kJ mol^{-1} at w_{IL} = 70%) to an unfavorable one in the IL-rich regime (+1.11 kJ mol^{-1} at w_{IL} = 95%); at 323 and 373 K, by contrast, $-Ts^{E}_{H_2O}$ remains uniformly favorable across the full concentration window. While the absolute magnitude of the 300 K crossover retains some sensitivity to the choice of partial molar enthalpy fit (Figure S13), $-Ts^{E}_{H_2O}$ counterbalances the partial molar enthalpy and thus unambiguously increases with IL content at 300 K and decreases at 323 and 373 K. Such a reversal in concentration and temperature dependence is elucidated by decomposing the water−water PMF (Figure S9) into its enthalpic and entropic contributions. The raw PMFs at the sampled temperatures are shown in Figure S8, with the decomposition obtained via eq 12 using three finite-difference schemes (ΔT = 20 K, ΔT = 30 K, and the 5-point linear least-squares fit[229]). First, the contact hydrogen-bonded minimum at $r \approx 2.8$ Å is enthalpically dominated and commensurately opposed by entropy. Additional local minima at $r \approx 5$ and 7 Å, albeit less favorable, are also enthalpically dominated—arising from the partial or total electrostatic screening of the water−water interaction by intervening ionic species.[243] The magnitudes of the decomposed contributions retain some sensitivity to the choice of finite-difference scheme, but the qualitative features discussed here are preserved across all three methods. Second, as the PMF evolves along the reaction coordinate, the enthalpic and entropic contributions mirror each other across all separations and diminish in concert as

Downloaded from pubs.acs.org/jpcbfk/article-pdf/doi/10.1021/acs.jpcb.6c04599/6906150/acs.jpcb.6c04599.pdf by GEORGIA INST OF TECHNOLOGY, Shehan Parmar on 04 November 2026

https://doi.org/10.1021/acs.jpcb.6c04599
J. Phys. Chem. B XXXX, XXX, XXX−XXX

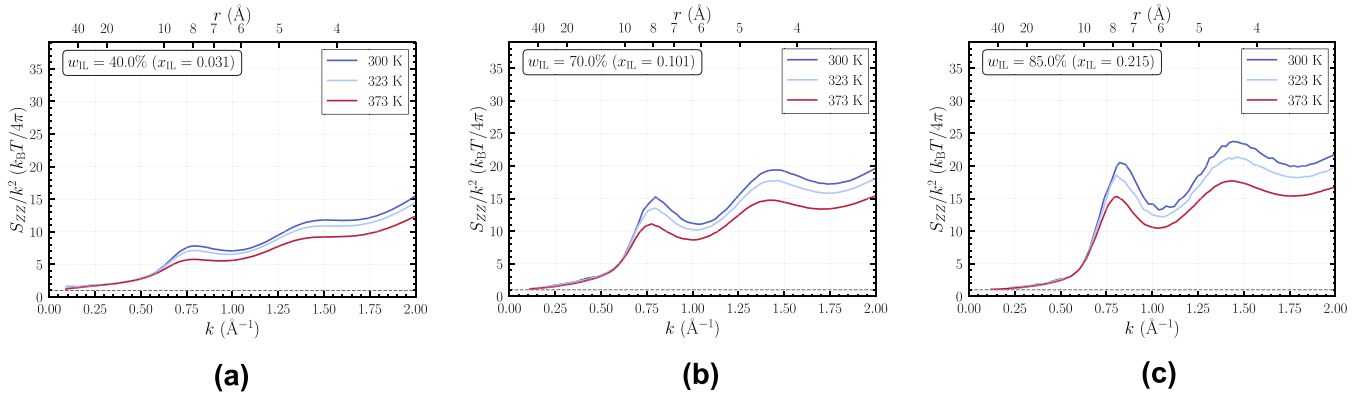


Figure 10. Charge−correlation structure factor, $S_{ZZ}(\mathbf{k})/k^2$, for $[P_{4444}][TFA]/H_2O$ mixtures at (a) w_{IL} = 40%, (b) w_{IL} = 70%, and (c) w_{IL} = 85% at 300, 323, and 373 K.

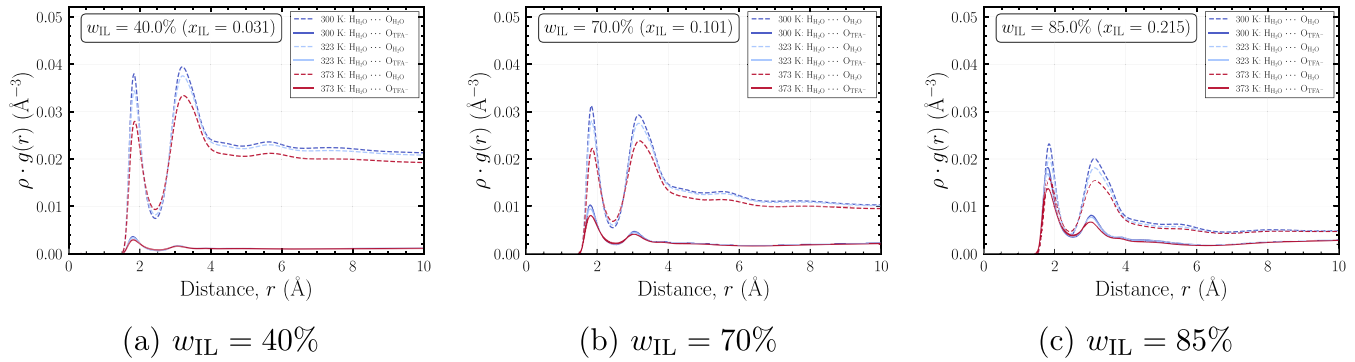


Figure 11. Radial number density, $\rho g(r)$, where ρ is the bulk number density of the acceptor oxygen (O_{H_2O} for water−water and O_{TFA^-} for water−anion), for $[P_{4444}][TFA]/H_2O$ mixtures at (a) w_{IL} = 40%, (b) w_{IL} = 70%, and (c) w_{IL} = 85% at 300, 323, and 373 K.

temperature rises. This balance is intrinsically tied to the microsolvation environment and structural heterogeneity imposed by the mixture, a connection quantified in the following section through the charge−charge structure factor $S_{ZZ}(\mathbf{k})$.

Taken together, Figure 9 reveals that neither the partial molar enthalpy nor the excess partial molar entropy of water dominates the chemical potential of mixing across the studied concentration and temperature window. Instead, the phase behavior of $[P_{4444}][TFA]/H_2O$ is shaped by *enthalpy−entropy compensation*.[81,118,210,265] The microscopic basis of compensation has been a long-standing question in solvation thermodynamics: as Ben-Naim notes, even with explicit decompositions of enthalpy and entropy in hand, "it is not clear whether this effect comes about from the direct solute−water interaction or through the indirect effect of the solute on the structure of the surroundings of the solvated water molecule."[210] For $[P_{4444}][TFA]/H_2O$ specifically, this compensation is evident in the strong temperature dependence of the partial molar enthalpy, the competition between ideal and non-ideal entropy contributions, and the microstructural heterogeneity of the mixture.

Modulation of Electrostatics and Local Structure

The molecular thermodynamics of water in $[P_{4444}][TFA]/H_2O$ thus far makes apparent a markedly heterogeneous solvation environment. Behind the heterogeneity lies a competition of ion−ion, water−water, and water−ion interactions governed by electrostatic screening, which can be probed in reciprocal space to recover the structural basis for the partial molar trends above. Concretely, the electrostatic energy of an ionic liquid can take the reciprocal-space form

$$E_{elec} = \frac{1}{2}\int d\mathbf{r}_1 d\mathbf{r}_2 \frac{\rho(\mathbf{r}_1)\rho(\mathbf{r}_2)}{r_{12}} = \frac{1}{2V}\sum_{\mathbf{k}} \frac{4\pi\rho_{\mathbf{k}}\rho_{-\mathbf{k}}}{k^2} \tag{23}$$

where $\rho(\mathbf{r})$ is the liquid charge density, $\rho_{\mathbf{k}}$ is the charge density Fourier component, and V is the system volume. The charge−correlation structure factor is as follows

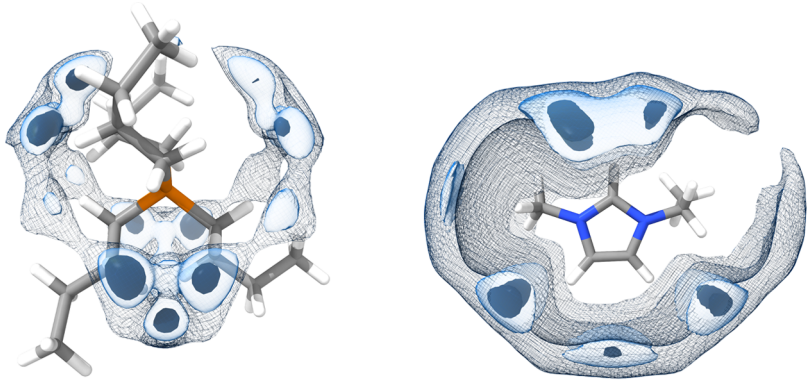
$$S_{ZZ}(\mathbf{k}) = \frac{1}{V}\langle \rho_{\mathbf{k}}\rho_{-\mathbf{k}} \rangle \tag{24}$$

where $\langle \cdots \rangle$ denotes the equilibrium ensemble average, such that $S_{ZZ}(\mathbf{k})/k^2$ quantifies the per-wavevector contribution to eq 23. $S_{ZZ}(\mathbf{k})/k^2$ is strictly repulsive, with peaks marking length scales over which unfavorable charge correlations accumulate—features we expect to modulate with concentration and temperature in concert with the favorable and unfavorable solvation physics highlighted in Figure 9.

Figure 10 shows $S_{ZZ}(\mathbf{k})/k^2$ for $[P_{4444}][TFA]/H_2O$ at w_{IL} = 40, 70, and 85% across 300, 323, and 373 K. Energies are reported in units of $k_BT/4\pi$, with the dashed asymptote at $\mathbf{k} \to 0$ fixed by the Stillinger−Lovett sum rule.[266−268] All three temperature curves recover the asymptote ($S_{ZZ}(\mathbf{k})/k^2 \approx k_BT/4\pi$, i.e., unity in the reported units) at low $\mathbf{k}$ on average, consistent for nonpolarizable force fields.[269] As w_{IL} increases toward neat $[P_{4444}][TFA]$, a repulsive peak develops near $k \approx 0.8$ Å^{-1}, attributable to a broad TFA^-−TFA^- coordination shell at ~10 Å (Figure S19). As water content increases, the peak heights attenuate monotonically, attributable to water

https://doi.org/10.1021/acs.jpcb.6c04599
J. Phys. Chem. B XXXX, XXX, XXX−XXX

Downloaded from pubs.acs.org/jpcbfk/article-pdf/doi/10.1021/acs.jpcb.6c04599/6906150/acs.jpcb.6c04599.pdf by GEORGIA INST OF TECHNOLOGY, Shehan Parmar on 04 November 2026



(a) (b)

Figure 12. Spatial distribution function (SDF) of water oxygen around the (a) P_{4444}^+ cation in $[P_{4444}][TFA]/H_2O$ and (b) $EMIM^+$ cation in $[EMIM][TFA]/H_2O$ at w_{IL} = 95% (ocean navy), 90% (cerulean), and 80% (deep cerulean, rendered as mesh), at 300 K and an absolute water−oxygen number density of 15 nm^{-3}. Bulk water oxygen densities are provided in Table S12. Full 360° rotation videos are included in the Supporting Information.

screening repulsive anion−anion electrostatics, analogous to the behavior observed in the hydrophilic imidazolium ILs ($[BMIM][BF_4]$, $[BMIM][NO_3]$, [BMIM][OTf]) characterized by McDaniel and Verma.[80] The absence of such a peak is itself a hydrophobic signature, as in water-immiscible ILs such as $[BMIM][PF_6]$, [BMIM][FSI], and [BMIM][TFSI], which lack the electrostatic driving force for favorable water solvation.

Remarkably, temperature mimics the effect of water dilution. At fixed w_{IL}, peak heights attenuate monotonically across 300−373 K. At w_{IL} = 85%, the peak height drops by ∼9% from 300 to 323 K and an additional ∼16% from 323 to 373 K. This starkly contrasts with, for example, the fully water-miscible [EMIM][TFA] IL, as shown in Figure S20: at the same w_{IL} = 85%, not only is its 300 K $S_{ZZ}(\mathbf{k})/k^2$ peak roughly 3× smaller, but it also drops by only ∼3% from 300 to 323 K and an additional ∼12% from 323 to 373 K. The temperature-driven attenuation of the $[P_{4444}][TFA]$ $S_{ZZ}(\mathbf{k})/k^2$ peak indicates temperature as a thermodynamic driving force, diminishing the local ion−ion electrostatic conditions that favor water mixing at low temperatures.

Functionally, electrostatics are enthalpic. That is, $S_{ZZ}(\mathbf{k})$ is a manifestation of real-space charge correlations driven by intermolecular interactions. Thus, pair correlations complement our reciprocal-space analysis, providing the local structure to further elucidate the temperature and concentration dependence observed in the partial molar enthalpy data. Following McDaniel and Son,[270] we report the radial distribution as the explicit pairwise probability $\rho g(r)$ (units of $Å^{-3}$), as opposed to $g(r)$, to provide direct comparisons of coordination peak heights across all w_{IL}.

Figure 11 shows $\rho g(r)$ for the water−water ($H_{H_2O}\cdots O_{H_2O}$, dashed) and water−anion ($H_{H_2O}\cdots O_{TFA^-}$, solid) pair correlations of $[P_{4444}][TFA]/H_2O$ at w_{IL} = 40, 70, and 85% across 300, 323, and 373 K. The bulk number density is set to the acceptor oxygen, $\rho_{O_{H2O}}$ and $\rho_{O_{TFA-}}$, respectively. Both pairs exhibit a sharp first peak near $r \approx 1.8$ Å, characteristic of hydrogen-bond contacts between the water proton and either water−oxygen or carboxylate−oxygen acceptors. The water−water and water−anion peak heights are inversely related, with water−water hydrogen bonds progressively replaced by competing water−anion coordination at increased w_{IL}. Near $w_{IL} \approx 85-87.5\%$, the two first-peak heights cross over, marking the structural transition from water−water to water−anion dominated coordination. Coordination numbers (eqs S31 and S32) integrated over the first solvation shell confirm the crossover quantitatively (Figure S17): the bulk water $N_{OH} \approx 1.8$ (or $N_{OO} \approx 5.2$ within 3.5 Å, consistent with the TIP3P benchmark[201]) and near-bulk $[P_{4444}][TFA]$ water−anion $N_{OH} \approx 1.3$ intersect at $w_{IL} \approx 87.5\%$ with $N_{OH} \approx 0.8$. In the later sections, we will also show the macroscopic consequence of this local coordination crossover, where water cluster and aggregation analyses illustrate the rupture of the percolating water network near $w_{IL} \approx 75\%$.

Underlying these concentration-dependent trends is a rising fraction of waters residing in water−anion-coordinated solvation shells with increasing w_{IL}. A subset are bound by a second anion—tethered into an anion−water−anion bridge motif—accounting for up to ∼18% of waters at w_{IL} = 95% and 300 K (Figure S18). By contrast, spherical-anion imidazolium ILs such as $[BMIM][BF_4]$ and $[BMIM][PF_6]$ show well-resolved anion−water−anion spectroscopic signatures as the dominant water motif, while TFA^-−containing ILs produce only broad, poorly resolved water−anion H-bond bands.[122] Structurally, the water forms two hydrogen bonds with the $-CO_2^-$ group in a bidentate fashion to optimize its interaction with the anion (as established for acetate by photoelectron and DFT studies[245,271]). The water−anion coordination growth is naturally coupled to the cation−anion network, whose $P^+\cdots O^-$ contact at ∼3.9 Å diminishes with temperature, in contrast to fully water-miscible [EMIM][TFA] (Figure S24).

The concentration and temperature dependence established thus far highlights the inseparable nature of structure and underlying solvation thermodynamics. We hypothesize that the P_{4444}^+ cation itself modulates the local microenvironments observed in the bulk, which in turn shapes the enthalpy−entropy compensation behavior of water. One clear reporter of the influence of P_{4444}^+ on bulk structure is the number-density analogue of the charge−correlation structure factor, in which the charge weighting is replaced by the atomic form factor. Namely, the number-density structure factor is as follows[251]

$$S_{NN}(\mathbf{k}) = \frac{1}{V}\langle \rho_N(\mathbf{k})\rho_N(-\mathbf{k})\rangle \tag{25}$$

where $\rho_N(\mathbf{k})$ is the Fourier component of the microscopic number density. For X-ray scattering, each atom contributes

https://doi.org/10.1021/acs.jpcb.6c04599
J. Phys. Chem. B XXXX, XXX, XXX−XXX

Downloaded from pubs.acs.org/jpcbfk/article-pdf/doi/10.1021/acs.jpcb.6c04599/6906150/acs.jpcb.6c04599.pdf by GEORGIA INST OF TECHNOLOGY, Shehan Parmar on 04 November 2026

proportionate to its electron density via the atomic form factor, $f_i(\mathbf{k})$,

$$\rho_N(\mathbf{k}) = \sum_{i=1}^{N} f_i(\mathbf{k}) e^{i\mathbf{k}\cdot\mathbf{r}_i} \tag{26}$$

Typically, $f_i(\mathbf{k})$ has a small k-dependence and can be approximated by the atomic number for S_{NN} evaluated at small wavevectors. Figure S21 shows $S_{NN}(\mathbf{k})$ for $[P_{4444}][TFA]/H_2O$ and $[EMIM][TFA]/H_2O$ at w_{IL} = 40, 70, and 85%. Near $k \approx 0.65-0.7$ Å^{-1} (a ∼9 Å real-space length scale), a pronounced prepeak emerges in $[P_{4444}][TFA]/H_2O$ that is entirely absent in [EMIM][TFA]. Previous studies have assigned such a prepeak to polarity domain alternation,[251,272] in which the polar anion/phosphonium-head alternates with the apolar butyl chains in real space.

Moreover, the hydrophobic nature of P_{4444}^+ has a clear consequence on the local water solvation shell. As w_{IL} increases, polarity domain alternation enhances butyl-tail aggregation, which naturally reshapes the surrounding microenvironment. To this end, we compute the SDF of water oxygen around the P_{4444}^+ and $EMIM^+$ cations using TRAVIS,[273] reporting absolute number densities in nm^{-3}; isosurfaces are rendered at a contour level of 15 nm^{-3} across w_{IL} = 80, 90, 95% at 300 K (Figure 12). In $[P_{4444}][TFA]/H_2O$, water density localizes into discrete lobes positioned in the geometric crevices between the four butyl arms at ∼4 Å from the phosphorus center, consistent with the first peak of the $P^+\cdots O_{H_2O}$ radial distribution function (Figure S25). Figure 12a shows 8−9 separated lobes at w_{IL} = 95% (total isosurface volume 2.06 Å^3, surface area 16.81 Å^2) that merge into four connected lobes at 90 wt % (15.58 Å^3, 79.19 Å^2) and a single connected surface at 80 wt % (46.41 Å^3, 167.7 Å^2) as water concentration increases.

In the analogous $[EMIM][TFA]/H_2O$ system, water density is more diffusely distributed across two distinct radial shells at ∼3.5 Å (in-plane carbon−water contact) and ∼5.4 Å (above and below the ring face) (Figure 12b), with isosurface volume 3−4× larger than $[P_{4444}][TFA]$ at every concentration (6.90 Å^3 vs 2.06 Å^3 at 95 wt %; 201.7 Å^3 vs 46.41 Å^3 at 80 wt %). While $[EMIM][TFA]/H_2O$ and $[P_{4444}][TFA]/H_2O$ display similar enthalpies of mixing across concentration at 300 K (Figures 8a and S15), the SDFs reveal an unmistakable difference in cation−water structural organization. While water surrounds the planar $EMIM^+$ in a cloud-like coordination environment, P_{4444}^+ imposes a more geometrically templated water shell. This is consistent with Morita's interpretation that the large hydration shell around P_{4444}^+ causes a loss of excess entropy of mixing.[61] Although dynamics lie outside the scope of this work, water reorientation is also markedly slower in $[P_{4444}][TFA]/H_2O$ than in $[EMIM][TFA]/H_2O$ (Figure S32), in line with the higher viscosity of the former.

The structural organization imposed by P_{4444}^+ has a direct geometric consequence on water hydrogen bonding. The analogous water−water and water−anion radial number densities for $[EMIM][TFA]/H_2O$ (Figure S22) and the corresponding coordination numbers (Figure S23) provide a stark structural fingerprint of how the hydrophobic P_{4444}^+ cation modulates the solvation shell structure. Qualitatively, the water−anion $H_{H_2O}\cdots O_{TFA^-}$ first peak grows more aggressively with w_{IL} in $[EMIM][TFA]$ than in $[P_{4444}][TFA]$; the suppressed water−anion coordination in $[P_{4444}][TFA]$ is compensated by enhanced water−water self-association. Quantitatively, at w_{IL} = 95% and 300 K, the water−water N_{OH} rises from 0.21 in [EMIM][TFA] to 0.49 in $[P_{4444}]$-[TFA], while the water−anion N_{OH} falls from 1.94 to 1.21. Interestingly, the P_{4444}^+ cation modulates the water−water/water−anion coordination crossover, where water−water N_{OH} overtakes water−anion N_{OH} in the range $w_{IL} \approx 75-80\%$ for [EMIM][TFA] as opposed to $w_{IL} \approx 85-87.5\%$ for $[P_{4444}]$-[TFA], indicating a propensity for water to form a connected H-bond network even at relatively IL-rich concentrations due to the hydrophobic nature of the cation,[81,103,274−276] as corroborated by the aggregation analysis in later sections. Beyond immediate H-bond distances, the joint geometric character of the H-bond, i.e., the intersection of radial separation and O−H···O angle, is captured in the combined distribution functions (Figures S27 and S28) and the anion-centered SDFs (Figure S26). Within the linear H-bond region ($1.5 \le r \le 2.2$ Å, $\theta \ge 150°$), water−anion contacts are subtly enriched in [EMIM][TFA], and water−water contacts are subtly enriched in $[P_{4444}][TFA]$.

Taken together, local solvation structure and electrostatics drive water solvation in $[P_{4444}][TFA]/H_2O$. The resulting macroscopic liquid−liquid phase behavior is, of course, a manifestation of enthalpy−entropy compensation: $h^E_{H_2O}$ and $s^E_{H_2O}$ are inescapably coupled through eq 22, such that the structural and electrostatic modulations resolved above are necessarily reflected in both the enthalpic and entropic contributions. Enumerating and evaluating all combinations of water−ion, water−water, and ion−ion interactions motivates theoretical frameworks that directly bridge structure to thermodynamics. For instance, Lazaridis and Karplus[226] decompose excess entropies of solvation via a sum of integrals over solute−solvent and solvent−solvent pair, triplet, and higher-order translational and orientational correlation functions. Within this ansatz, the entropic penalty of solvation is encoded in the positional and orientational correlation of water with its surrounding solvent environment, as implicated herein.

Water Aggregation and Network Analysis

The concentration dependence of $[P_{4444}][TFA]/H_2O$ mixing manifests across short- and long-range length scales. While the RDFs in Figure 11 resolve local coordination motifs, the mesoscopic organization of water is naturally characterized as a hydrogen-bond network defined by interconnected water aggregates.[277] To this end, graph network and cluster analyses have been previously applied to a range of IL and IL/water systems,[251,278−280] which we adapt for understanding water aggregation in $[P_{4444}][TFA]/H_2O$. Concretely, two waters are taken as hydrogen-bonded under the distance−angle criterion $r_{OH} \le 2.27$ Å and $\alpha \le 40°$ (equivalently $\theta_{O-H\cdots O} \ge 140°$),[82] with a graph network algorithm performed using a fork of MDTraj.[281,282] By construction, each water molecule constitutes a node and each hydrogen bond an edge, such that connected nodes form a water aggregate (equivalently, a water cluster). Unlike conventional hydrogen-bond analyses (e.g., the coordination numbers shown in Figures S17 and S23), the graph network analysis herein provides longer-range, mesoscopic connectivity implications. The molecule-weighted aggregate size distribution,

$$P(n) = \frac{n\langle N(n)\rangle}{N_{H_2O}} \tag{27}$$

Downloaded from pubs.acs.org/jpcbfk/article-pdf/doi/10.1021/acs.jpcb.6c04599/6906150/acs.jpcb.6c04599.pdf by GEORGIA INST OF TECHNOLOGY, Shehan Parmar on 04 November 2026

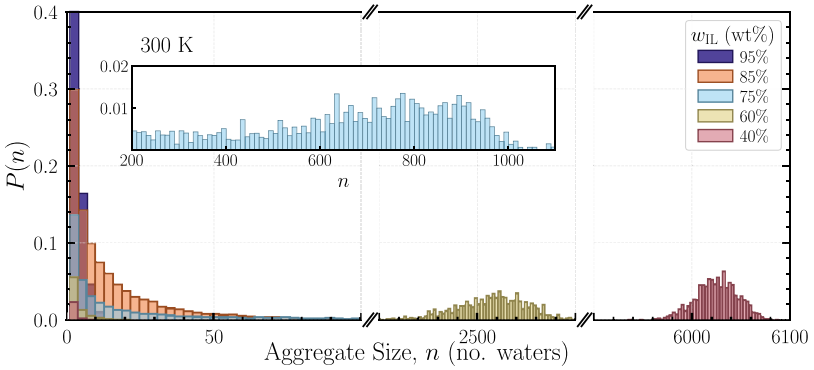


Figure 13. Molecule-weighted water aggregate size distribution, $P(n)$, at 300 K for $[P_{4444}][TFA]/H_2O$ mixtures at five IL weight fractions.

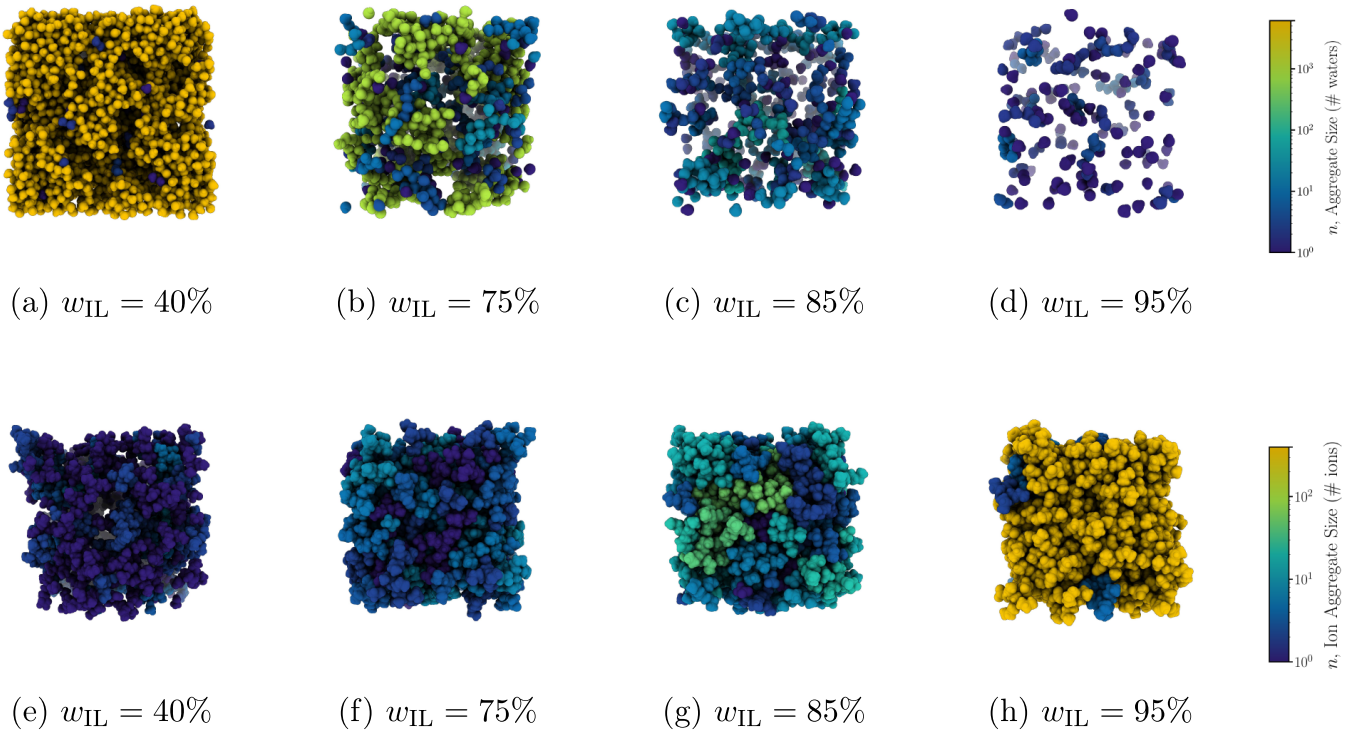


Figure 14. Representative snapshots of the water hydrogen-bond network (top row; water molecules only) and the ionic liquid polar network (bottom row; ions only) in $[P_{4444}][TFA]/H_2O$ mixtures at 300 K, colored by cluster membership. (a) Water network spanning the entire simulation box. (b) Coexistence of heterogeneous water cluster networks near the percolation limit. (c) Small water clusters with emerging chain-like aggregates. (d) Isolated water molecules and small water clusters. (e) Small, dispersed ion clusters in the water-rich regime. (f) Intermediate ion aggregates near the water percolation limit. (g) Large ion clusters forming a near-continuous polar network. (h) Nearly all ions belong to a single continuous polar network spanning the simulation box.

gives the probability that a randomly chosen water belongs to a cluster of size n, where $\langle\cdots\rangle$ denotes the ensemble average, $N(n)$ is the number of size−n clusters, and N_{H_2O} is the total number of water molecules in the system.[278] Figure 13 shows the $P(n)$ at 300 K across five IL weight fractions, each corresponding to a water-only system snapshot colored by cluster membership (i.e., the water molecule color corresponds to its respective water cluster's unique aggregate size n) in Figure 14a−d. The entire concentration sweep at 13 values at 300 K is included in Figure S33.

Three concentration regimes emerge in Figure 13 for $[P_{4444}][TFA]/H_2O$ at 300 K. At $w_{IL} > 92.5\%$, $P(n)$ peaks sharply at $n = 1$ with negligible probability beyond $n \approx 10$, indicating isolated water monomers and tiny clusters (Figure 14d). From $92.5\% \geq w_{IL} \geq 75\%$, $P(n)$ evolves from smaller clusters (~15−20 waters at $w_{IL} = 92.5\%$) to larger, chain-like aggregates (~500 waters at $w_{IL} = 80\%$), which define the percolation threshold (Figure 14b,c). The percolation crossover seen in Figure 13 is also mirrored in the local coordination structure, where the water−water and water−anion RDFs trade peak heights near this concentration regime (Figure 11). For $w_{IL} < 75\%$, $P(n)$ shows concentrated probability density near $n = N_{H_2O}$, where clusters begin to span the entire simulation box to form bicontinuous water and ion aggregates. Similarly, the ion aggregate distributions mirror these water cluster concentration regimes (Figures S35 and 14e−h). In fact, the ion aggregate behavior reveals a direct connection between water network evolution with increased dilution and the enthalpy of mixing trends reported in Figure 8a. At $w_{IL} \approx 92.5\%$, precisely where the enthalpy of mixing

https://doi.org/10.1021/acs.jpcb.6c04599
J. Phys. Chem. B XXXX, XXX, XXX−XXX

Downloaded from pubs.acs.org/jpcbfk/article-pdf/doi/10.1021/acs.jpcb.6c04599/6906150/acs.jpcb.6c04599.pdf by GEORGIA INST OF TECHNOLOGY, Shehan Parmar on 04 November 2026

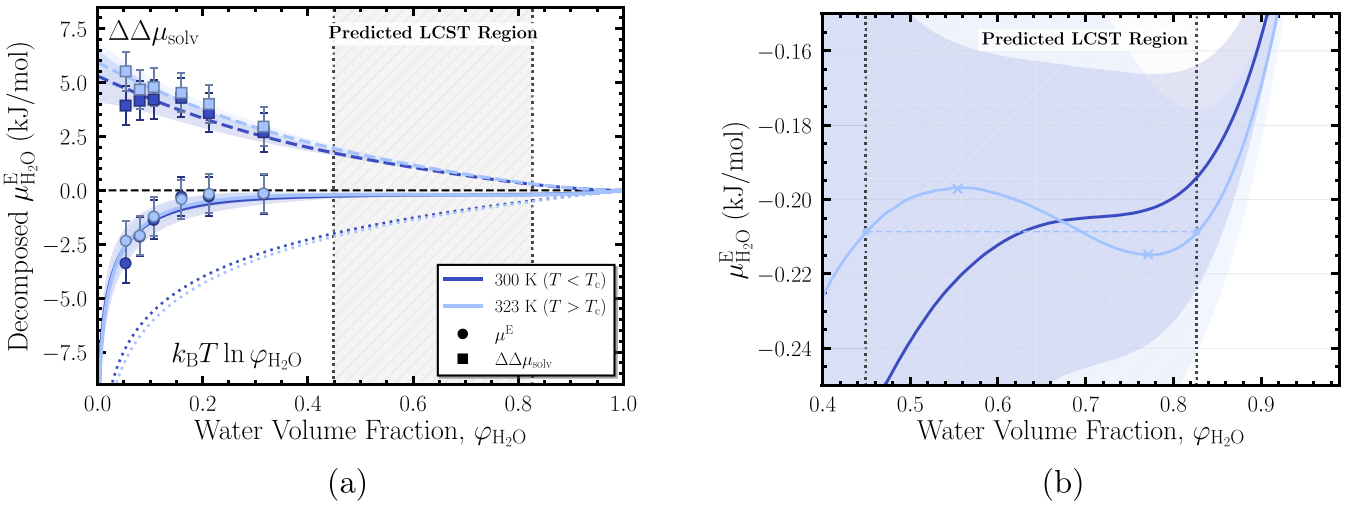


Figure 15. Bayesian inference of the water chemical potential $\mu^E_{H_2O}(\varphi_{H_2O}, T)$. (a) Posterior median $\mu^E_{H_2O}$ (solid) decomposed into the ideal density term ($k_BT \ln \varphi_{H_2O}$, dotted) and the non-ideal solvation excess ($\Delta\Delta\mu_{solv}$, dashed) at 300 and 323 K, with simulated data (markers, ±0.9 kJ mol^{-1}); the hatched band marks the predicted 323 K coexistence (LCST) region. (b) Zoomed-in view of the predicted LCST region, in kJ mol^{-1}.

reaches its minimum ($h^E_M = -3.45$ kJ mol^{-1}), the ion aggregate $P(n)$ in Figure S34c shows the polar network fragmenting into a visible bimodal distribution. The enthalpy minimum marks the point along the evolving water and ion networks where water−anion interactions are most optimal. Further dilution grows water from isolated monomers into larger aggregates that disrupt and fragment the IL polar network, with water−water self-interactions progressively overtaking the enthalpically favorable cross-term and thus driving h^E_M further toward ideality in the bicontinuous regime at $w_{IL} < 75\%$.[283]

LCST MECHANISTIC INSIGHT

Phase separation is driven by the tendency to lower the free energy.[284] Liquid−liquid demixing is classically rationalized in terms of the excess Gibbs energy of mixing, $G^E_{mix} = \sum_i N_i \mu^E_i$.[210] In water/*n*-alkane systems near room temperature, G^E_{mix} is sufficiently positive across a wide enough concentration window that it develops two distinct minima (i.e., separated by a locally concave-down region where $\partial^2 G^E_{mix}/\partial\varphi^2_{H_2O} < 0$) near the infinite-dilution limits, corresponding to two, nearly pure coexisting phases of low mutual solubility. Similarly, above the critical temperature of the $T-\varphi_{H2O}$ phase coexistence curve, $[P_{4444}][TFA]/H_2O$ separates into two coexisting phases that retain residual amounts of both species.[173] Thus, phase separation behavior is most rigorously captured by the stability criterion,[285,286] intuitively observed as the change in chemical potential with *water volume fraction*, φ_{H_2O}. That is, given the general boundary conditions $\mu^E_{H_2O}(\varphi_{H_2O} = 0) \to -\infty$ and $\mu^E_{H_2O}(\varphi_{H_2O} = 1) = 0$, a stable single-phase binary mixture must satisfy $\partial\mu^E_{H_2O}/\partial\varphi_{H_2O} \geq 0$ over the full concentration range. Conversely, the mixture is unstable wherever this criterion is violated, i.e.,

$$\left(\frac{\partial \mu^E_{H_2O}}{\partial \varphi_{H_2O}}\right)_{T,P} \approx \frac{k_BT}{\varphi_{H_2O}} + \left(\frac{\partial \Delta\Delta\mu_{solv}}{\partial \varphi_{H_2O}}\right)_{T,P} < 0 \quad (28)$$

where the excess molar volume effects are neglected for simplicity ($\rho^M_{H_2O}/\rho^p_{H_2O} \approx \varphi_{H_2O}$; eqs 21 and 19). The first term is always necessarily positive. Equation 28 thus leads to the corollary that $\partial\Delta\Delta\mu_{solv}/\partial\varphi_{H_2O}$ must be sufficiently negative (over some concentration range, and not necessarily across all concentrations) for phase separation to occur.

It thus follows that the "levers" controlling liquid−liquid phase separation are most naturally rationalized by enthalpic and (non-ideal) entropic contributions to the solvation free energy, $\Delta\Delta\mu_{solv} \approx h^E_{H_2O} - Ts^{E,n.id.}_{H_2O}$. Differentiating with respect to φ_{H_2O}, the condition for phase separation to occur can then be recast as

$$\left(\frac{\partial \Delta\Delta\mu_{solv}}{\partial \varphi_{H_2O}}\right)_{T,P} \approx \left(\frac{\partial h^E_{H_2O}}{\partial \varphi_{H_2O}}\right)_{T,P} - T\left(\frac{\partial s^{E,n.id.}_{H_2O}}{\partial \varphi_{H_2O}}\right)_{T,P} < -\frac{k_BT}{\varphi_{H_2O}} \quad (29)$$

From eq 29, the empirically observed UCST and LCST behaviors can each be rationalized as one of two potential conditions for phase separation. On the one hand, UCST is recovered when both enthalpy and entropy decrease with volume fraction (i.e., $\partial h^E_{H_2O}/\partial\varphi_{H_2O} < 0$ and $\partial s^{E,n.id.}_{H_2O}/\partial\varphi_{H_2O} < 0$, with $h^E_{H_2O} > 0$ and $s^{E,n.id.}_{H_2O} > 0$ decaying toward zero). Separately, because the entropic contribution scales with temperature, this yields a two-phase system at sufficiently low temperatures, where $\partial h^E_{H_2O}/\partial\varphi_{H_2O} < T\,\partial s^{E,n.id.}_{H_2O}/\partial\varphi_{H_2O} - k_BT/\varphi_{H_2O}$, and a single phase at higher temperatures, where $\partial h^E_{H_2O}/\partial\varphi_{H_2O} > T\,\partial s^{E,n.id.}_{H_2O}/\partial\varphi_{H_2O} - k_BT/\varphi_{H_2O}$. On the other hand, one possibility for conditions that favor LCST is when both enthalpy and entropy *increase* with volume fraction (i.e., $\partial h^E_{H_2O}/\partial\varphi_{H_2O} > 0$ and $\partial s^{E,n.id.}_{H_2O}/\partial\varphi_{H_2O} > 0$, with $h^E_{H_2O} < 0$ and $s^{E,n.id.}_{H_2O} < 0$ approaching zero). Again, because the entropic contribution scales with temperature, this yields a two-phase system at sufficiently *high* temperatures ($\partial\mu^E_{H_2O}/\partial\varphi_{H_2O} < 0$), where $\partial h^E_{H_2O}/\partial\varphi_{H_2O} < T\,\partial s^{E,n.id.}_{H_2O}/\partial\varphi_{H_2O} - k_BT/\varphi_{H_2O}$, and a single phase at lower temperatures ($\partial\mu^E_{H_2O}/\partial\varphi_{H_2O} > 0$), where $\partial h^E_{H_2O}/\partial\varphi_{H_2O} > T\,\partial s^{E,n.id.}_{H_2O}/\partial\varphi_{H_2O} - k_BT/\varphi_{H_2O}$.

For $[P_{4444}][TFA]/H_2O$, the observed enthalpy and entropy results trend in the direction of the latter, LCST scenario.

https://doi.org/10.1021/acs.jpcb.6c04599
J. Phys. Chem. B XXXX, XXX, XXX−XXX

Downloaded from pubs.acs.org/jpcbfk/article-pdf/doi/10.1021/acs.jpcb.6c04599/6906150/acs.jpcb.6c04599.pdf by GEORGIA INST OF TECHNOLOGY, Shehan Parmar on 04 November 2026

From Figure 9 at 300 K, $h^{E}_{H_2O}$ rises from ∼−4.5 (w_{IL} = 95%) to ∼+0.1 kJ mol^{-1} (w_{IL} = 70%) while $s^{E,n.id.}_{H_2O}$ rises from ∼−28 to ∼−9 J mol^{-1} K^{-1} over the same range, satisfying both $\partial h^{E}_{H_2O}/\partial\varphi_{H_2O} > 0$ and $\partial s^{E,n.id.}_{H_2O}/\partial\varphi_{H_2O} > 0$. Although the φ_{H_2O} dependence is less clear at higher temperatures, where $h^{E}_{H_2O}$ ostensibly approaches ideality ($h^{E}_{H_2O} \approx 0$) by $\varphi_{H_2O} \gtrsim 0.22$, the non-ideal entropy gradient persists, with $s^{E,n.id.}_{H_2O}$ rising from ∼−13 to ∼−8 J mol^{-1} K^{-1} at 373 K. The requisite negative solvation gradient for phase separation is then borne out in Figure 5b, which confirms $\partial\Delta\Delta\mu_{solv}/\partial\varphi_{H_2O} = \partial\Delta\mu_{solv}/\partial\varphi_{H_2O} \lesssim 0$, with $\Delta\Delta\mu_{solv}$ decreasing by ∼1−3 kJ mol^{-1} across the sampled φ_{H_2O} window (clearest at 373 K, falling from ∼+6.3 to ∼+3.4 kJ mol^{-1}).

Moving beyond discrete, simulated $\mu^{E}_{H_2O}$ values to uncover complete, continuous $\mu^{E}_{H_2O}(\varphi_{H_2O}, T)$ curves is itself nontrivial. In the Flory−Huggins framework, the excess chemical potential is often expressed through a conventional interaction parameter, χ, i.e., $\mu^{E}_{H_2O} = k_BT \ln \varphi_{H_2O} + \chi(1-\varphi_{H_2O})^2$, to absorb non-idealities.[287] To instead deduce *probabilistic* $\mu^{E}_{H_2O}(\varphi_{H_2O}, T)$ curves, one desires curves that are (1) data-driven, i.e., constrained by discrete, simulated $\mu^{E}_{H_2O}$, and (2) physics-informed, i.e., carrying a reasonable temperature dependence (e.g., $\chi \propto a/T + b$ ref[288,289]) and enforcing physical constraints (e.g., $\partial\mu^{E}_{H_2O}/\partial\varphi_{H_2O} = \partial^2\mu^{E}_{H_2O}/\partial\varphi^2_{H_2O} = 0$ at the experimental critical point, eq S39). To this end, we apply a Bayesian inference methodology (implemented in Pyro/NumPyro;[290,291] see Supporting Information, eqs S35−S40) that places priors on Redlich−Kister coefficients of a two-dimensional $\mu^{E}_{H_2O}(\varphi_{H_2O}, T)$.

As shown in Figure 15a and b, the resulting $\mu^{E}_{H_2O}(\varphi_{H_2O}, T)$ curves at 300 and 323 K are drawn from posterior distributions of Redlich−Kister coefficients (eq S36, Figure S36) that, by construction, satisfy the critical-point conditions at the experimental (φ_{H_2O} = 0.71, T_c = 303 K). Outside the predicted coexistence window, the Redlich−Kister form yields a monotonic $\mu^{E}_{H_2O}$, consistent with a stable single phase (eq 28); within it, applying the Maxwell equal-area rule (eq S40) to the 323 K curve outlines an LCST region that is semi-quantitatively consistent with the experimental coexistence window.[173] From this investigation, it is thus possible to rationalize plausible LCST $\mu^{E}_{H_2O}(\varphi_{H_2O}, T)$ curves that discriminate the two-phase binodal region through a chemical potential barrier of less than ∼100 J mol^{-1} (Figure 15b).

Beyond the quantitative values and concentration-dependent trends in $h^{E}_{H_2O}$ and $s^{E}_{H_2O}$, their delicate and complex compensating behavior (amounting to only ∼−1 to −2 kJ mol^{-1} in $\mu^{E}_{H_2O}$) explains why LCST is observed in such a narrow concentration−temperature phase space for many ILs. Moreover, the compensation itself can be viewed as a property of the ion's molecular structure: as shown in Figure 12a, the P_{4444}^{+} cation heavily influences the structural organization of water in its solvation environment. Thus, it is plausible to surmise that because LCST reflects such a fragile balance, even structurally similar ILs such as [N_{4444}][TFA] and [P_{5555}][TFA] fail to exhibit LCST behavior.[52]

CONCLUSIONS

For the lower critical solution temperature (LCST) ionic liquid [P_{4444}][TFA]/H_2O mixture, equilibrium molecular dynamics simulations and finite-concentration thermodynamic integration simulations were paired with chilled-mirror dew point water activity experiments to compute the excess chemical potential ($\mu^{E}_{H_2O}$), partial molar enthalpy ($h^{E}_{H_2O}$), and partial molar entropy ($s^{E}_{H_2O}$) of water. Simulated $\mu^{E}_{H_2O}$ values show excellent agreement with experimental measurements over w_{IL} = 85−95% and T = 300 and 323 K, with absolute deviations ranging from 0.04 to 1.2 kJ mol^{-1} depending on the concentration and temperature. Since $\mu^{E}_{H_2O}$ decomposes into a volume fraction-dependent ideal entropy of mixing contribution—identical between simulation and experiment by construction—and a non-ideal solvation free energy, the agreement confirms the non-ideal solvation contribution is accurately resolved.

The excess chemical potential decomposes into a strongly favorable density-ratio contribution (governed by the large ∼19:1 IL/water molar volume ratio) and a uniformly unfavorable solvation free energy difference (relative to bulk water) of $\Delta\Delta\mu_{solv} \approx$ +3 to +6 kJ mol^{-1} that grows with both increasing w_{IL} and increasing temperature. The excess enthalpy of mixing exhibits a strong temperature dependence across the entire concentration window, shifting from exothermic at 300 K ($h^{E}_{H_2O}(w_{IL}$ = 95%) = −4.5 ± 0.3 kJ mol^{-1}) to endothermic at 373 K (+1.3 ± 0.1 kJ mol^{-1}), with a magnitude exceeding the typical range across IL/water mixtures.[254] The non-ideal entropy of solvation is uniformly unfavorable (+3 to +8.4 kJ mol^{-1} at 300 K) and most sensitive to concentration, exactly where $h^{E}_{H_2O}$ is most sensitive to temperature, a signature of tightly compensating enthalpy and entropy contributions.[81,210]

Mechanistically, the enthalpy−entropy compensation is traced to both short- and long-range electrostatics and structure. The charge−correlation structure factor $S_{ZZ}(\mathbf{k})/k^2$ exhibits a repulsive peak near ∼0.8 Å^{-1}, which unambiguously attenuates with both dilution and, more surprisingly, temperature—a behavior conspicuously absent from [EMIM][TFA]. The $S_{ZZ}(\mathbf{k})/k^2$ reveals a clear enthalpic signature, which is compensated by the structural organization of water imposed by the P_{4444}^{+} cation. The concentration dependence of $\mu^{E}_{H_2O}$, $h^{E}_{H_2O}$, and $s^{E}_{H_2O}$ is governed by the competition between water−water and water−anion coordination, which undergoes a stark crossover to favor the latter over the former past $w_{IL} \approx$ 87.5%. From spatial distribution functions, water arranges into geometrically confined lobes between the butyl arms of P_{4444}^{+}, while the rotational relaxation times highlight the effects of increased viscosity of [P_{4444}][TFA] at low water concentrations.

Taken together, these results reframe long-standing interpretations of LCST IL phase behavior. The "negative entropy of mixing" hypothesis frequently invoked in the LCST literature[60−62] is resolved from the uniformly unfavorable *partial molar entropy of solvation*. The enthalpy/entropy decomposition sustains a negative $\partial\Delta\Delta\mu_{solv}/\partial\varphi_{H_2O}$ across the studied IL-rich concentrations, thus plausibly compatible with the stability conditions required for LCST. This motivates ongoing work in high-throughput molecular dynamics[292,293] to systematically map the enthalpy/entropy landscape across a wider IL chemical space.

Downloaded from pubs.acs.org/jpcbfk/article-pdf/doi/10.1021/acs.jpcb.6c04599/6906150/acs.jpcb.6c04599.pdf by GEORGIA INST OF TECHNOLOGY, Shehan Parmar on 04 November 2026

https://doi.org/10.1021/acs.jpcb.6c04599
J. Phys. Chem. B XXXX, XXX, XXX−XXX

■ ASSOCIATED CONTENT

Supporting Information

The Supporting Information is available free of charge at https://pubs.acs.org/doi/10.1021/acs.jpcb.6c04599.

Summary of simulation conditions; derivation of the chemical potential of water from statistical mechanics; thermodynamic integration protocol and convergence study; derivation of the non-ideal entropy; mole-fraction- and temperature-dependent densities and excess molar volumes; density ratios; force field benchmarks (water self-solvation in TIP3P); single-water solvation free energy at infinite dilution; water−water potential of mean force and its enthalpy/entropy decomposition; solvation free energy magnitudes and component decomposition; cohesive energy; concentration- and temperature-dependent excess and partial molar enthalpies with parametric-bootstrap uncertainty quantification; [EMIM][TFA]/H_2O excess enthalpy of mixing; experimental enthalpy/entropy decomposition; water coordination numbers; anion−water−anion bridge coordination; TFA^-−TFA^- radial distribution function; structural comparisons between $[P_{4444}][TFA]$ and [EMIM][TFA], including the charge−correlation and number-density structure factors, water−water and water−anion radial number densities, water−water/water−anion coordination crossover, and cation−anion radial number densities; rotational autocorrelation functions of water in $[P_{4444}][TFA]$ and [EMIM][TFA]; water and ion aggregate size distributions across the concentration window; and Bayesian inference of the water excess chemical potential $\mu^{E}_{H_2O}(\varphi_{H_2O}, T)$ recovering LCST phase behavior, including the Redlich−Kister model, priors, likelihood, physical constraints, and posterior coefficient distributions (PDF)

360° rotation of the water-oxygen SDF around the P_{4444}^+ cation in $[P_{4444}][TFA]$/water at 95 wt% IL, 300 K (MP4)

360° rotation of the water-oxygen SDF around the $EMIM^+$ cation in [EMIM][TFA]/water at 95 wt% IL, 300 K. (MP4)

360° rotation of the water-oxygen SDF at the TFA^- anion hydrogen-bond site in $[P_{4444}][TFA]$/water at 95 wt% IL, 300 K (MP4)

360° rotation of the water-oxygen SDF at the TFA^- anion hydrogen-bond site in [EMIM][TFA]/water at 95 wt% IL, 300 K (MP4)

OpenMM_scripts (ZIP)

■ AUTHOR INFORMATION

Corresponding Author

Jesse G. McDaniel − *Department of Chemistry and Biochemistry, Georgia Institute of Technology, Atlanta, Georgia 30332, United States;* orcid.org/0000-0002-9211-1108; Email: mcdaniel@gatech.edu

Authors

Shehan M. Parmar − *Department of Chemistry and Biochemistry, Georgia Institute of Technology, Atlanta, Georgia 30332, United States;* orcid.org/0000-0002-2033-0862

Ahmed Mahfouz − *George W. Woodruff School of Mechanical Engineering, Georgia Institute of Technology, Atlanta, Georgia 30332, United States;* orcid.org/0000-0001-5664-0806

Akanksha K. Menon − *George W. Woodruff School of Mechanical Engineering, Georgia Institute of Technology, Atlanta, Georgia 30332, United States;* orcid.org/0000-0003-1979-507X

Complete contact information is available at: https://pubs.acs.org/10.1021/acs.jpcb.6c04599

Notes

The authors declare no competing financial interest.

■ ACKNOWLEDGMENTS

S.M.P. acknowledges support from the U.S. Department of Energy, Office of Science, Office of Advanced Scientific Computing Research, Department of Energy Computational Science Graduate Fellowship under Award Number DE-SC0022158, and the NERSC ERCAP 2022 grant number ERCAP0021857. S.M.P. was also supported by the Molecular Sciences Software Institute (MolSSI) Software Fellowship under NSF grant CHE-2136142. A.M. acknowledges support from the Woodruff School of Mechanical Engineering at Georgia Tech. The authors would also like to acknowledge Andrew Z. Haddad at the Lawrence Berkeley National Laboratory (LBNL) for synthesizing the IL studied in this work, Jordan D. Kocher at the National Laboratory of the Rockies (NLR) for an insightful discussion on LCST thermodynamics, and Chloe Renfro for valuable discussions on potentials of mean force (PMFs).

■ REFERENCES

(1) Zhou, J.; Liu, X.; Zhang, S.; Zhang, X.; Yu, G. Effect of Small Amount of Water on the Dynamics Properties and Microstructures of Ionic Liquids. *AIChE J.* **2017**, *63*, 2248−2256.

(2) Blanchard, L. A.; Gu, Z.; Brennecke, J. F. High-Pressure Phase Behavior of Ionic Liquid/CO_2 Systems. *J. Phys. Chem. B* **2001**, *105*, 2437−2444.

(3) Welton, T. Room-Temperature Ionic Liquids. Solvents for Synthesis and Catalysis. *Chem. Rev.* **1999**, *99*, 2071−2084.

(4) Endres, F.; Zein El Abedin, S. Air and Water Stable Ionic Liquids in Physical Chemistry. *Phys. Chem. Chem. Phys.* **2006**, *8*, 2101.

(5) Visser, A. E.; Swatloski, R. P.; Reichert, W. M.; Davis, J. H., Jr.; Rogers, R. D.; Mayton, R.; Sheff, S.; Wierzbicki, A. Task-Specific Ionic Liquids for the Extraction of Metal Ions from Aqueous Solutions. *Chem. Commun.* **2001**, 135−136.

(6) Huddleston, J. G.; Visser, A. E.; Reichert, W. M.; Willauer, H. D.; Broker, G. A.; Rogers, R. D. Characterization and Comparison of Hydrophilic and Hydrophobic Room Temperature Ionic Liquids Incorporating the Imidazolium Cation. *Green Chem.* **2001**, *3*, 156−164.

(7) Wang, Y.-L.; Sarman, S.; Glavatskih, S.; Antzutkin, O. N.; Rutland, M. W.; Laaksonen, A. Atomistic Insight into Tetraalkylphosphonium-Bis(Oxalato)Borate Ionic Liquid/Water Mixtures. I. Local Microscopic Structure. *J. Phys. Chem. B* **2015**, *119*, 5251−5264.

(8) Chauvin, Y.; Mussmann, L.; Olivier, H. A Novel Class of Versatile Solvents for Two-Phase Catalysis: Hydrogenation, Isomerization, and Hydroformylation of Alkenes Catalyzed by Rhodium Complexes in Liquid 1,3-Dialkylimidazolium Salts. *Angew. Chem., Int. Ed.* **1996**, *34*, 2698−2700.

(9) Schröder, U.; Wadhawan, J. D.; Compton, R. G.; Marken, F.; Suarez, P. A. Z.; Consorti, C. S.; De Souza, R. F.; Dupont, J. Water-Induced Accelerated Ion Diffusion: Voltammetric Studies in 1-Methyl-3-[2,6-(S)-Dimethylocten-2-Yl]Imidazolium Tetrafluorobo-

Downloaded from pubs.acs.org/jpcbfk/article-pdf/doi/10.1021/acs.jpcb.6c04599/6906150/acs.jpcb.6c04599.pdf by GEORGIA INST OF TECHNOLOGY, Shehan Parmar on 04 November 2026

rate, 1-Butyl-3-Methylimidazolium Tetrafluoroborate and Hexafluorophosphate Ionic Liquids. *New J. Chem.* **2000**, *24*, 1009−1015.
(10) Abe, H.; Nakama, K.; Hayashi, R.; Aono, M.; Takekiyo, T.; Yoshimura, Y.; Saihara, K.; Shimizu, A. Electrochemical Anomalies of Protic Ionic Liquid - Water Systems: A Case Study Using Ethylammonium Nitrate - Water System. *Chem. Phys.* **2016**, *475*, 119−125.
(11) Chen, H.; Kwait, D. C.; Gönen, Z. S.; Weslowski, B. T.; Abdallah, D. J.; Weiss, R. G. Phase Characterization and Properties of Completely Saturated Quaternary Phosphonium Salts. Ordered, Room-Temperature Ionic Liquids. *Chem. Mater.* **2002**, *14*, 4063−4072.
(12) Getsis, A.; Mudring, A.-V. Imidazolium Based Ionic Liquid Crystals: Structure, Photophysical and Thermal Behaviour of [Cnmim]Br·xH2O (n = 12, 14; X = 0, 1). *Cryst. Res. Technol.* **2008**, *43*, 1187−1196.
(13) Majhi, D.; Dai, J.; Komolkin, A. V.; Dvinskikh, S. V. Understanding Ionic Mesophase Stabilization by Hydration: A Solid-State NMR Study. *Phys. Chem. Chem. Phys.* **2020**, *22*, 13408−13417.
(14) Saielli, G. The Effect of Hydration on the Stability of Ionic Liquid Crystals: MD Simulations of [C14C1im]Cl and [C14C1im]-Cl·H2O. *Phys. Chem. Chem. Phys.* **2021**, *23*, 24386−24395.
(15) Amrousse, R.; Katsumi, T.; Bachar, A.; Brahmi, R.; Bensitel, M.; Hori, K. Chemical Engineering Study for Hydroxylammonium Nitrate Monopropellant Decomposition over Monolith and Grain Metal-Based Catalysts. *React. Kinet., Mech. Catal.* **2014**, *111*, 71−88.
(16) Decker, M.; Klein, N.; Freedman, E.; Leveritt, C.; Wojciechowski, J. *HAN-based Liquid Gun Propellants: Physical Properties,*; Technical Report BRL.-TR-2864, 1987.
(17) Depew, D. D.; Vaghjiani, G. L.; Parmar, S. M.; Wang, J. J. Liquid Structure and Hydrogen Bonding in Aqueous Hydroxylammonium Nitrate. *J. Phys. Chem. B* **2024**, *128*, 824−840.
(18) Seddon, K. R.; Stark, A.; Torres, M.-J. Influence of Chloride, Water, and Organic Solvents on the Physical Properties of Ionic Liquids. *Pure Appl. Chem.* **2000**, *72*, 2275−2287.
(19) Gardas, R. L.; Freire, M. G.; Carvalho, P. J.; Marrucho, I. M.; Fonseca, I. M. A.; Ferreira, A. G. M.; Coutinho, J. A. P. High-Pressure Densities and Derived Thermodynamic Properties of Imidazolium-Based Ionic Liquids. *J. Chem. Eng. Data* **2007**, *52*, 80−88.
(20) Freire, M. G.; Carvalho, P. J.; Gardas, R. L.; Marrucho, I. M.; Santos, L. M. N. B. F.; Coutinho, J. A. P. Mutual Solubilities of Water and the [Cnmim][Tf2N] Hydrophobic Ionic Liquids. *J. Phys. Chem. B* **2008**, *112*, 1604−1610.
(21) Vekariya, R. L. A Review of Ionic Liquids: Applications towards Catalytic Organic Transformations. *J. Mol. Liq.* **2017**, *227*, 44−60.
(22) Papasizza, M.; Yang, X.; Cheng, J.; Cuesta, A. Electrocatalytic Reduction of CO2 in Neat and Water-Containing Imidazolium-Based Ionic Liquids. *Curr. Opin. Electrochem.* **2020**, *23*, 80−88.
(23) Yuan, L.; Zhang, L.; Feng, J.; Jiang, C.; Feng, J.; Li, C.; Zeng, S.; Zhang, X. Upscaling Studies for Efficiently Electric-Driven CO2 Reduction to CO in Ionic Liquid-Based Electrolytes. *Chem. Eng. J.* **2022**, *450*, 138378.
(24) Mantovi, P. S.; Da Cruz, J. C.; De Angelis, L. D.; Souza, M. L.; Rossi, L. M.; Córdoba De Torresi, S. I.; Lima, F. H. B.; Torresi, R. M. Tuning CO_2 RR Pathways through Water Control in Ionic Liquids. *ACS Catal.* **2025**, *15*, 18261−18269.
(25) Khan, I.; Kurnia, K. A.; Mutelet, F.; Pinho, S. P.; Coutinho, J. A. P. Probing the Interactions between Ionic Liquids and Water: Experimental and Quantum Chemical Approach. *J. Phys. Chem. B* **2014**, *118*, 1848−1860.
(26) Byrne, N.; Angell, C. A. Formation and Dissolution of Hen Egg White Lysozyme Amyloid Fibrils in Protic Ionic Liquids. *Chem. Commun.* **2009**, 1046−1048.
(27) Byrne, N.; Angell, C. A. The Solubility of Hen Lysozyme in Ethylammonium Nitrate/H2O Mixtures and a Novel Approach to Protein Crystallization. *Molecules* **2010**, *15*, 793−803.
(28) Debeljuh, N.; Barrow, C. J.; Byrne, N. The Impact of Ionic Liquids on Amyloid Fibrilization of Aβ16-22: Tuning the Rate of Fibrilization Using a Reverse Hofmeister Strategy. *Phys. Chem. Chem. Phys.* **2011**, *13*, 16534−16536.
(29) Debeljuh, N.; Barrow, C. J.; Henderson, L.; Byrne, N. Structure Inducing Ionic Liquids−Enhancement of Alpha Helicity in the Abeta(1-40) Peptide from Alzheimer's Disease. *Chem. Commun.* **2011**, *47*, 6371−6373.
(30) Weingärtner, H.; Cabrele, C.; Herrmann, C. How Ionic Liquids Can Help to Stabilize Native Proteins. *Phys. Chem. Chem. Phys.* **2012**, *14*, 415−426.
(31) Oprzeska-Zingrebe, E. A.; Smiatek, J. Aqueous Ionic Liquids in Comparison with Standard Co-Solutes. *Biophysical Reviews* **2018**, *10*, 809−824.
(32) Anouti, M.; Jacquemin, J.; Porion, P. Transport Properties Investigation of Aqueous Protic Ionic Liquid Solutions through Conductivity, Viscosity, and NMR Self-Diffusion Measurements. *J. Phys. Chem. B* **2012**, *116*, 4228−4238.
(33) Geng, Y.; Chen, S.; Wang, T.; Yu, D.; Peng, C.; Liu, H.; Hu, Y. Density, Viscosity and Electrical Conductivity of 1-Butyl-3-Methylimidazolium Hexafluorophosphate + Monoethanolamine and + N, N-dimethylethanolamine. *J. Mol. Liq.* **2008**, *143*, 100−108.
(34) Zhao, Y.; Zhang, X.; Zeng, S.; Zhou, Q.; Dong, H.; Tian, X.; Zhang, S. Density, Viscosity, and Performances of Carbon Dioxide Capture in 16 Absorbents of Amine + Ionic Liquid + H_2O, Ionic Liquid + H_2O, and Amine + H_2O Systems. *J. Chem. Eng. Data* **2010**, *55*, 3513−3519.
(35) Qiao, Y.; Ma, W.; Theyssen, N.; Chen, C.; Hou, Z. Temperature-Responsive Ionic Liquids: Fundamental Behaviors and Catalytic Applications. *Chem. Rev.* **2017**, *117*, 6881−6928.
(36) Bianga, J.; Künnemann, K. U.; Gaide, T.; Vorholt, A. J.; Seidensticker, T.; Dreimann, J. M.; Vogt, D. Thermomorphic Multiphase Systems: Switchable Solvent Mixtures for the Recovery of Homogeneous Catalysts in Batch and Flow Processes. *Chem.—Eur. J.* **2019**, *25*, 11586−11608.
(37) Kohno, Y.; Ohno, H. Ionic Liquid/Water Mixtures: From Hostility to Conciliation. *Chem. Commun.* **2012**, *48*, 7119−7130.
(38) Kohno, Y.; Saita, S.; Murata, K.; Nakamura, N.; Ohno, H. Extraction of Proteins with Temperature Sensitive and Reversible Phase Change of Ionic Liquid/Water Mixture. *Polym. Chem.* **2011**, *2*, 862.
(39) Vander Hoogerstraete, T.; Onghena, B.; Binnemans, K. Homogeneous Liquid-Liquid Extraction of Metal Ions with a Functionalized Ionic Liquid. *J. Phys. Chem. Lett.* **2013**, *4*, 1659−1663.
(40) Onghena, B.; Jacobs, J.; Van Meervelt, L.; Binnemans, K. Homogeneous Liquid-Liquid Extraction of Neodymium(Iii) by Choline Hexafluoroacetylacetonate in the Ionic Liquid Choline Bis(Trifluoromethylsulfonyl)Imide. *Dalton Trans.* **2014**, *43*, 11566−11578.
(41) Depuydt, D.; Liu, L.; Glorieux, C.; Dehaen, W.; Binnemans, K. Homogeneous Liquid-Liquid Extraction of Metal Ions with Non-Fluorinated Bis(2-Ethylhexyl)Phosphate Ionic Liquids Having a Lower Critical Solution Temperature in Combination with Water. *Chem. Commun.* **2015**, *51*, 14183−14186.
(42) Ventura, S. P. M.; e Silva, F. A.; Quental, M. V.; Mondal, D.; Freire, M. G.; Coutinho, J. A. P. Ionic-Liquid-Mediated Extraction and Separation Processes for Bioactive Compounds: Past, Present, and Future Trends. *Chem. Rev.* **2017**, *117*, 6984−7052.
(43) Shukla, S. K.; Pandey, S.; Pandey, S. Applications of Ionic Liquids in Biphasic Separation: Aqueous Biphasic Systems and Liquid-Liquid Equilibria. *J. Chromatogr. A* **2018**, *1559*, 44−61.
(44) Kurniawan, K.; Kim, S.; Lee, J.-c. *Ionic Liquid-Based Technologies for Environmental Sustainability*; Elsevier, 2022; pp 295−329.
(45) Cai, Y.; Shen, W.; Wei, J.; Chong, T. H.; Wang, R.; Krantz, W. B.; Fane, A. G.; Hu, X. Energy-Efficient Desalination by Forward Osmosis Using Responsive Ionic Liquid Draw Solutes. *Environ. Sci.: Water Res. Technol.* **2015**, *1*, 341−347.
(46) Zhong, Y.; Feng, X.; Chen, W.; Wang, X.; Huang, K.-W.; Gnanou, Y.; Lai, Z. Using UCST Ionic Liquid as a Draw Solute in

Downloaded from pubs.acs.org/jpcbfk/article-pdf/doi/10.1021/acs.jpcb.6c04599/6906150/acs.jpcb.6c04599.pdf by GEORGIA INST OF TECHNOLOGY, Shehan Parmar on 04 November 2026

Forward Osmosis to Treat High-Salinity Water. *Environ. Sci. Technol.* **2016**, *50*, 1039−1045.
(47) Hsu, C.-H.; Ma, C.; Bui, N.; Song, Z.; Wilson, A. D.; Kostecki, R.; Diederichsen, K. M.; McCloskey, B. D.; Urban, J. J. Enhanced Forward Osmosis Desalination with a Hybrid Ionic Liquid/Hydrogel Thermoresponsive Draw Agent System. *ACS Omega* **2019**, *4*, 4296−4303.
(48) Zeweldi, H. G.; Bendoy, A. P.; Park, M. J.; Shon, H. K.; Johnson, E. M.; Kim, H.-S.; Kim, H.; Chung, W.-J.; Nisola, G. M. Forward Osmosis with Direct Contact Membrane Distillation Using Tetrabutylphosphonium P-Toluenesulfonate as an Effective and Safe Thermo-Recyclable Osmotic Agent for Seawater Desalination. *Chemosphere* **2021**, *263*, 128070.
(49) Zeweldi, H. G.; Bendoy, A. P.; Park, M. J.; Shon, H. K.; Kim, H.-S.; Johnson, E. M.; Kim, H.; Lee, S.-P.; Chung, W.-J.; Nisola, G. M. Tetrabutylammonium 2,4,6-Trimethylbenzenesulfonate as an Effective and Regenerable Thermo-Responsive Ionic Liquid Drawing Agent in Forward Osmosis for Seawater Desalination. *Desalination* **2020**, *495*, 114635.
(50) Kamio, E.; Kurisu, H.; Takahashi, T.; Matsuoka, A.; Yoshioka, T.; Nakagawa, K.; Sun, Y.; Matsuyama, H. Effect of Temperature on the Osmotic Behavior of LCST Type Ionic Liquid Solutions as Draw Solutions in the Forward Osmosis Process. *Sep. Purif. Technol.* **2021**, *275*, 119164.
(51) Haddad, A. Z.; Menon, A. K.; Kang, H.; Urban, J. J.; Prasher, R. S.; Kostecki, R. Solar Desalination Using Thermally Responsive Ionic Liquids Regenerated with a Photonic Heater. *Environ. Sci. Technol.* **2021**, *55*, 3260−3269.
(52) Kohno, Y.; Ohno, H. Temperature-Responsive Ionic Liquid/Water Interfaces: Relation between Hydrophilicity of Ions and Dynamic Phase Change. *Phys. Chem. Chem. Phys.* **2012**, *14*, 5063−5070.
(53) Chu, Y.-H.; Cheng, M.-F.; Chiang, Y.-H. Combinatorial Discovery of Small-Molecule 1,2,3-Triazolium Ionic Liquids Exhibiting Lower Critical Solution Temperature Phase Transition. *Sci. Rep.* **2020**, *10*, No. 18247.
(54) Chu, Y.-H.; Hwang, C.-C.; Chen, C.-Y.; Tseng, M.-J. Combinatorial Discovery of Thermoresponsive Cycloammonium Ionic Liquids. *Chem. Commun.* **2020**, *56*, 11855−11858.
(55) Chu, Y.-H.; Chen, C.-Y. Structural Fine-Tuning of Zwitterionic Salts for the Discovery of LCST-type Thermoresponsive Materials. *Mater. Chem. Front.* **2021**, *5*, 7286−7290.
(56) Chu, Y.-H.; Chen, C.-Y.; Chen, J.-S. Structural Engineering and Optimization of Zwitterionic Salts for Expeditious Discovery of Thermoresponsive Materials. *Molecules* **2022**, *27*, 257.
(57) Ando, T.; Kohno, Y.; Nakamura, N.; Ohno, H. Introduction of Hydrophilic Groups onto the Ortho-Position of Benzoate Anions Induced Phase Separation of the Corresponding Ionic Liquids with Water. *Chem. Commun.* **2013**, *49*, 10248.
(58) Zhao, Y.; Wang, H.; Pei, Y.; Liu, Z.; Wang, J. Understanding the Mechanism of LCST Phase Separation of Mixed Ionic Liquids in Water by MD Simulations. *Phys. Chem. Chem. Phys.* **2016**, *18*, 23238−23245.
(59) Gulotty, E. M.; Sanadhya, S.; Tucker, Z. D.; Moghaddam, S. S.; Ashfeld, B. L. Controlling Phase Separation Behavior of Thermo-Responsive Ionic Liquids through the Directed Distribution of Anionic Charge. *J. Mol. Liq.* **2022**, *360*, 119401.
(60) Kang, H.; Suich, D. E.; Davies, J. F.; Wilson, A. D.; Urban, J. J.; Kostecki, R. Molecular Insight into the Lower Critical Solution Temperature Transition of Aqueous Alkyl Phosphonium Benzene Sulfonates. *Commun. Chem.* **2019**, *2*, No. 51.
(61) Morita, T.; Miki, K.; Nitta, A.; Ohgi, H.; Westh, P. Effects of Constituent Ions of a Phosphonium-Based Ionic Liquid on Molecular Organization of H2O as Probed by 1-Propanol: Tetrabutylphosphonium and Trifluoroacetate Ions. *Phys. Chem. Chem. Phys.* **2015**, *17*, 22170−22178.
(62) Forero-Martinez, N. C.; Cortes-Huerto, R.; Benedetto, A.; Ballone, P. Thermoresponsive Ionic Liquid/Water Mixtures: From Nanostructuring to Phase Separation. *Molecules* **2022**, *27* (5), 1647 DOI: 10.3390/molecules27051647.
(63) Billinge, I. H.; Barbosa, G. D.; Tao, S.; Terban, M. W.; Turner, C. H.; Billinge, S. J. L.; Yip, N. Y. A Structural Underpinning of the Lower Critical Solution Temperature (LCST) Behavior behind Temperature-Switchable Liquids. *Matter* **2025**, *8*, 101879.
(64) Choi, E.; Yethiraj, A. Entropic Mechanism for the Lower Critical Solution Temperature of Poly(Ethylene Oxide) in a Room Temperature Ionic Liquid. *ACS Macro Lett.* **2015**, *4*, 799−803.
(65) Zhao, C.; Ma, Z.; Zhu, X. X. Rational Design of Thermoresponsive Polymers in Aqueous Solutions: A Thermodynamics Map. *Prog. Polym. Sci.* **2019**, *90*, 269−291.
(66) Nitta, A.; Morita, T.; Saita, S.; Kohno, Y.; Ohno, H.; Nishikawa, K. Density Fluctuations in Aqueous Solution of Ionic Liquid with Lower Critical Solution Temperature: Mixture of Tetrabutylphosphonium Trifluoroacetate and Water. *Chem. Phys. Lett.* **2015**, *628*, 108−112.
(67) Zhao, Y.; Tian, L.; Pei, Y.; Wang, H.; Wang, J. Effect of Anionic Structure on the LCST Phase Behavior of Phosphonium Ionic Liquids in Water. *Ind. Eng. Chem. Res.* **2018**, *57*, 12935−12941.
(68) Kumari, P.; Pillai, V. V. S.; Gobbo, D.; Ballone, P.; Benedetto, A. The Transition from Salt-in-Water to Water-in-Salt Nanostructures in Water Solutions of Organic Ionic Liquids Relevant for Biological Applications. *Phys. Chem. Chem. Phys.* **2021**, *23*, 944−959.
(69) Wang, R.; Leng, W.; Gao, Y.; Yu, L. Microemulsion-like Aggregation Behaviour of an LCST-type Ionic Liquid in Water. *RSC Adv.* **2014**, *4*, 14055−14062.
(70) Meyer, G.; Schweins, R.; Youngs, T.; Dufrêche, J.-F.; Billard, I.; Plazanet, M. How Temperature Rise Can Induce Phase Separation in Aqueous Biphasic Solutions. *J. Phys. Chem. Lett.* **2022**, *13*, 2731−2736.
(71) Dong, S.; Heyda, J.; Yuan, J.; Schalley, C. A. Lower Critical Solution Temperature (LCST) Phase Behaviour of an Ionic Liquid and Its Control by Supramolecular Host-Guest Interactions. *Chem. Commun.* **2016**, *52*, 7970−7973.
(72) Shiflett, M. B.; Yokozeki, A. Hydrogen Substitution Effect on the Solubility of Perhalogenated Compounds in Ionic Liquid [Bmim][PF6]. *Fluid Phase Equilib.* **2007**, *259*, 210−217.
(73) Shiflett, M. B.; Yokozeki, A. Liquid-Liquid Equilibria in Binary Mixtures Containing Fluorinated Benzenes and Ionic Liquid 1-Ethyl-3-methylimidazolium Bis(Trifluoromethylsulfonyl)Imide. *J. Chem. Eng. Data* **2008**, *53*, 2683−2691.
(74) Lovelock, K. R. J. Quantifying Intermolecular Interactions of Ionic Liquids Using Cohesive Energy Densities. *R. Soc. Open Sci.* **2017**, *4*, No. 171223, DOI: 10.1098/rsos.171223.
(75) McDaniel, J. G.; Choi, E.; Son, C. Y.; Schmidt, J. R.; Yethiraj, A. Ab Initio Force Fields for Imidazolium-Based Ionic Liquids. *J. Phys. Chem. B* **2016**, *120*, 7024−7036.
(76) Anderson, C. J.; Deakin, M. R.; Choppin, G. R.; D'Olieslager, W.; Heerman, L.; Pruett, D. J. Spectroscopy and Electrochemistry of Uranium(IV)/Uranium(III) in Basic Aluminum Chloride-1-Ethyl-3-Methylimidazolium Chloride. *Inorg. Chem.* **1991**, *30*, 4013−4016.
(77) Bonhôte, P.; Dias, A.-P.; Papageorgiou, N.; Kalyanasundaram, K.; Grätzel, M. Hydrophobic, Highly Conductive Ambient-Temperature Molten Salts. *Inorg. Chem.* **1996**, *35*, 1168−1178.
(78) Wilkes, J. S.; Levisky, J. A.; Wilson, R. A.; Hussey, C. L. Dialkylimidazolium Chloroaluminate Melts: A New Class of Room-Temperature Ionic Liquids for Electrochemistry, Spectroscopy and Synthesis. *Inorg. Chem.* **1982**, *21*, 1263−1264.
(79) Anthony, J. L.; Maginn, E. J.; Brennecke, J. F. Solution Thermodynamics of Imidazolium-Based Ionic Liquids and Water. *J. Phys. Chem. B* **2001**, *105*, 10942−10949.
(80) McDaniel, J. G.; Verma, A. On the Miscibility and Immiscibility of Ionic Liquids and Water. *J. Phys. Chem. B* **2019**, *123*, 5343−5356.
(81) Chandler, D. Interfaces and the Driving Force of Hydrophobic Assembly. *Nature* **2005**, *437*, 640−647.
(82) Kumar, R.; Schmidt, J. R.; Skinner, J. L. Hydrogen Bonding Definitions and Dynamics in Liquid Water. *J. Chem. Phys.* **2007**, *126*, 204107.

Downloaded from pubs.acs.org/jpcbfk/article-pdf/doi/10.1021/acs.jpcb.6c04599/6906150/acs.jpcb.6c04599.pdf by GEORGIA INST OF TECHNOLOGY, Shehan Parmar on 04 November 2026

(83) Bernal, J. D.; Fowler, R. H. A Theory of Water and Ionic Solution, with Particular Reference to Hydrogen and Hydroxyl Ions. *J. Chem. Phys.* **1933**, *1*, 515−548.
(84) Narten, A. H.; Levy, H. A. Liquid Water: Molecular Correlation Functions from X-Ray Diffraction. *J. Chem. Phys.* **1971**, *55*, 2263−2269.
(85) Rahman, A.; Stillinger, F. H. Molecular Dynamics Study of Liquid Water. *J. Chem. Phys.* **1971**, *55*, 3336−3359.
(86) Stillinger, F. H. Water Revisited. *Science* **1980**, *209*, 451−457.
(87) Silverstein, K. A. T.; Haymet, A. D. J.; Dill, K. A. The Strength of Hydrogen Bonds in Liquid Water and Around Nonpolar Solutes. *J. Am. Chem. Soc.* **2000**, *122*, 8037−8041.
(88) Brini, E.; Fennell, C. J.; Fernandez-Serra, M.; Hribar-Lee, B.; Lukšič, M.; Dill, K. A. How Water's Properties Are Encoded in Its Molecular Structure and Energies. *Chem. Rev.* **2017**, *117*, 12385−12414.
(89) Frank, H. S.; Wen, W.-Y. Ion-Solvent Interaction. Structural Aspects of Ion-Solvent Interaction in Aqueous Solutions: A Suggested Picture of Water Structure. *Discuss. Faraday Soc.* **1957**, *24*, 133−140.
(90) Eliezer, I.; Krindel, P. Calculations on Alkali and Halide Ion Hydration. *J. Chem. Phys.* **1972**, *57*, 1884−1891.
(91) Marcus, Y. Effect of Ions on the Structure of Water: Structure Making and Breaking. *Chem. Rev.* **2009**, *109*, 1346−1370.
(92) Hribar, B.; Southall, N. T.; Vlachy, V.; Dill, K. A. How Ions Affect the Structure of Water. *J. Am. Chem. Soc.* **2002**, *124*, 12302−12311.
(93) Gurney, R. W. *Ionic Processes in Solution*; McGraw-Hill, 1953.
(94) Dill, K. A.; Truskett, T. M.; Vlachy, V.; Hribar-Lee, B. Modeling Water, the Hydrophobic Effect, and Ion Solvation. *Annu. Rev. Biophys. Biomol. Struct.* **2005**, *34*, 173−199.
(95) Wachter, W.; Kunz, W.; Buchner, R.; Hefter, G. Is There an Anionic Hofmeister Effect on Water Dynamics? Dielectric Spectroscopy of Aqueous Solutions of NaBr, NaI, NaNO3, NaClO4, and NaSCN. *J. Phys. Chem. A* **2005**, *109*, 8675−8683.
(96) Xu, H.; Dill, K. A. Water's Hydrogen Bonds in the Hydrophobic Effect: A Simple Model. *J. Phys. Chem. B* **2005**, *109*, 23611−23617.
(97) Ben-Amotz, D.; Widom, B. Generalized Solvation Heat Capacities. *J. Phys. Chem. B* **2006**, *110*, 19839−19849.
(98) Bouazizi, S.; Nasr, S.; Jaîdane, N.; Bellissent-Funel, M.-C. Local Order in Aqueous NaCl Solutions and Pure Water:X-ray Scattering and Molecular Dynamics Simulations Study. *J. Phys. Chem. B* **2006**, *110*, 23515−23523.
(99) Soper, A. K.; Weckström, K. Ion Solvation and Water Structure in Potassium Halide Aqueous Solutions. *Biophys. Chem.* **2006**, *124*, 180−191.
(100) Vchirawongkwin, V.; Hofer, T. S.; Randolf, B. R.; Rode, B. M. Tl(I)-the Strongest Structure-Breaking Metal Ion in Water? A Quantum Mechanical/Molecular Mechanical Simulation Study. *J. Comput. Chem.* **2007**, *28*, 1006−1016.
(101) Mancinelli, R.; Botti, A.; Bruni, F.; Ricci, M. A.; Soper, A. K. Hydration of Sodium, Potassium, and Chloride Ions in Solution and the Concept of Structure Maker/Breaker. *J. Phys. Chem. B* **2007**, *111*, 13570−13577.
(102) Mancinelli, R.; Botti, A.; Bruni, F.; Ricci, M. A.; Soper, A. K. Perturbation of Water Structure Due to Monovalent Ions in Solution. *Phys. Chem. Chem. Phys.* **2007**, *9*, 2959−2967.
(103) Thomas, A. S.; Elcock, A. H. Molecular Dynamics Simulations of Hydrophobic Associations in Aqueous Salt Solutions Indicate a Connection between Water Hydrogen Bonding and the Hofmeister Effect. *J. Am. Chem. Soc.* **2007**, *129*, 14887−14898.
(104) Singh, A. K.; Doan, L. C.; Lou, D.; Wen, C.; Vinh, N. Q. Interfacial Layers between Ion and Water Detected by Terahertz Spectroscopy. *J. Chem. Phys.* **2022**, *157*, 054501.
(105) Balos, V.; Kaliannan, N. K.; Elgabarty, H.; Wolf, M.; Kühne, T. D.; Sajadi, M. Time-Resolved Terahertz-Raman Spectroscopy Reveals That Cations and Anions Distinctly Modify Intermolecular Interactions of Water. *Nat. Chem.* **2022**, *14*, 1031−1037.
(106) Kropman, M.; Bakker, H. Vibrational Relaxation of Liquid Water in Ionic Solvation Shells. *Chem. Phys. Lett.* **2003**, *370*, 741−746.
(107) Omta, A. W.; Kropman, M. F.; Woutersen, S.; Bakker, H. J. Influence of Ions on the Hydrogen-Bond Structure in Liquid Water. *J. Chem. Phys.* **2003**, *119*, 12457−12461.
(108) Omta, A. W.; Kropman, M. F.; Woutersen, S.; Bakker, H. J. Negligible Effect of Ions on the Hydrogen-Bond Structure in Liquid Water. *Science* **2003**, *301*, 347−349.
(109) Näslund, L.; Edwards, D. C.; Wernet, P.; Bergmann, U.; Ogasawara, H.; Pettersson, L. G. M.; Myneni, S.; Nilsson, A. X-Ray Absorption Spectroscopy Study of the Hydrogen Bond Network in the Bulk Water of Aqueous Solutions. *J. Phys. Chem. A* **2005**, *109*, 5995−6002.
(110) Bakker, H. J.; Kropman, M. F.; Omta, A. W. Effect of Ions on the Structure and Dynamics of Liquid Water. *J. Phys.: Condens. Matter* **2005**, *17*, S3215.
(111) Guàrdia, E.; Laria, D.; Martí, J. Hydrogen Bond Structure and Dynamics in Aqueous Electrolytes at Ambient and Supercritical Conditions. *J. Phys. Chem. B* **2006**, *110*, 6332−6338.
(112) Kronberg, B. The Hydrophobic Effect. *Curr. Opin. Colloid Interface Sci.* **2016**, *22*, 14−22.
(113) Pratt, L. R.; Chandler, D. Theory of the Hydrophobic Effect. *J. Chem. Phys.* **1977**, *67*, 3683−3704.
(114) Ben-Naim, A. *Hydrophobic Interactions*; Springer US: Boston, MA, 1980.
(115) Clarke, S. The Hydrophobic Effect: Formation of Micelles and Biological Membranes, 2nd Edition (Tanford, Charles). *J. Chem. Educ.* **1981**, *58*, A246.
(116) Silverstein, K. A. T.; Haymet, A. D. J.; Dill, K. A. A Simple Model of Water and the Hydrophobic Effect. *J. Am. Chem. Soc.* **1998**, *120*, 3166−3175.
(117) Hummer, G.; Garde, S.; García, A. E.; Paulaitis, M. E.; Pratt, L. R. Hydrophobic Effects on a Molecular Scale. *J. Phys. Chem. B* **1998**, *102*, 10469−10482.
(118) Widom, B.; Bhimalapuram, P.; Koga, K. The Hydrophobic Effect. *Phys. Chem. Chem. Phys.* **2003**, *5*, 3085−3093.
(119) Collins, K. D. Charge Density-Dependent Strength of Hydration and Biological Structure. *Biophys. J.* **1997**, *72*, 65−76.
(120) Fennell, C. J.; Bizjak, A.; Vlachy, V.; Dill, K. A. Ion Pairing in Molecular Simulations of Aqueous Alkali Halide Solutions. *J. Phys. Chem. B* **2009**, *113*, 6782−6791.
(121) Gujt, J.; Bešter-Rogač, M.; Hribar-Lee, B. An Investigation of Ion-Pairing of Alkali Metal Halides in Aqueous Solutions Using the Electrical Conductivity and the Monte Carlo Computer Simulation Methods. *J. Mol. Liq.* **2014**, *190*, 34−41.
(122) Cammarata, L.; Kazarian, S. G.; Salter, P. A.; Welton, T. Molecular States of Water in Room Temperature Ionic Liquids. *Phys. Chem. Chem. Phys.* **2001**, *3*, 5192−5200.
(123) Danten, Y.; Cabaço, M. I.; Besnard, M. Interaction of Water Highly Diluted in 1-Alkyl-3-methyl Imidazolium Ionic Liquids with the PF_6^- and BF_4^- Anions. *J. Phys. Chem. A* **2009**, *113*, 2873−2889.
(124) Méndez-Morales, T.; Carrete, J.; Cabeza, Ó.; Gallego, L. J.; Varela, L. M. Molecular Dynamics Simulation of the Structure and Dynamics of Water-1-Alkyl-3-methylimidazolium Ionic Liquid Mixtures. *J. Phys. Chem. B* **2011**, *115*, 6995−7008.
(125) Maiti, A.; Kumar, A.; Rogers, R. D. Water-Clustering in Hygroscopic Ionic Liquids−an Implicit Solvent Analysis. *Phys. Chem. Chem. Phys.* **2012**, *14*, 5139.
(126) van der Post, S. T.; Scheidelaar, S.; Bakker, H. J. Water Dynamics in Aqueous Solutions of Tetra-n-alkylammonium Salts: Hydrophobic and Coulomb Interactions Disentangled. *J. Phys. Chem. B* **2013**, *117*, 15101−15110.
(127) Cha, S.; Ao, M.; Sung, W.; Moon, B.; Ahlström, B.; Johansson, P.; Ouchi, Y.; Kim, D. Structures of Ionic Liquid-Water Mixtures Investigated by IR and NMR Spectroscopy. *Phys. Chem. Chem. Phys.* **2014**, *16*, 9591−9601.
(128) Yaghini, N.; Nordstierna, L.; Martinelli, A. Effect of Water on the Transport Properties of Protic and Aprotic Imidazolium Ionic

Downloaded from pubs.acs.org/jpcbfk/article-pdf/doi/10.1021/acs.jpcb.6c04599/6906150/acs.jpcb.6c04599.pdf by GEORGIA INST OF TECHNOLOGY, Shehan Parmar on 04 November 2026

Liquids - an Analysis of Self-Diffusivity, Conductivity, and Proton Exchange Mechanism. *Phys. Chem. Chem. Phys.* **2014**, *16*, 9266−9275.
(129) Fadeeva, T. A.; Husson, P.; DeVine, J. A.; Costa Gomes, M. F.; Greenbaum, S. G.; Castner, E. W. Interactions between Water and 1-Butyl-1-Methylpyrrolidinium Ionic Liquids. *J. Chem. Phys.* **2015**, *143*, 064503.
(130) Liu, X.; Zhou, G.; Huo, F.; Wang, J.; Zhang, S. Unilamellar Vesicle Formation and Microscopic Structure of Ionic Liquids in Aqueous Solutions. *J. Phys. Chem. C* **2016**, *120*, 659−667.
(131) Serva, A.; Migliorati, V.; Lapi, A.; Aquilanti, G.; Arcovito, A.; D'Angelo, P. Structural Properties of Geminal Dicationic Ionic Liquid/Water Mixtures: A Theoretical and Experimental Insight. *Phys. Chem. Chem. Phys.* **2016**, *18*, 16544−16554.
(132) Wu, Y.; Wang, X.; Liu, Q.; Ma, X.; Fang, D.; Jiang, X.; Guan, W. Dynamic Phase Change and Local Structures in IL-containing Mixtures: Classical MD Simulations and Experiments. *Phys. Chem. Chem. Phys.* **2017**, *19*, 3028−3038.
(133) Kaneko, K.; Saihara, K.; Masuda, Y.; Yoshimura, Y.; Shimizu, A. Dynamic Properties of Water Molecules in Ionic Liquid/Water Mixture with Various Alkyl Chain Length. *J. Mol. Liq.* **2018**, *264*, 337−342.
(134) Mele, A.; Tran, C. D.; De Paoli Lacerda, S. H. The Structure of a Room-Temperature Ionic Liquid with and without Trace Amounts of Water: The Role of CH···O and CH···F Interactions in 1-n-Butyl-3-Methylimidazolium Tetrafluoroborate. *Angew. Chem.* **2003**, *115*, 4500−4502.
(135) Jiang, W.; Wang, Y.; Voth, G. A. Molecular Dynamics Simulation of Nanostructural Organization in Ionic Liquid/Water Mixtures. *J. Phys. Chem. B* **2007**, *111*, 4812−4818.
(136) Jeon, Y.; Sung, J.; Kim, D.; Seo, C.; Cheong, H.; Ouchi, Y.; Ozawa, R.; Hamaguchi, H.-o. Structural Change of 1-Butyl-3-methylimidazolium Tetrafluoroborate + Water Mixtures Studied by Infrared Vibrational Spectroscopy. *J. Phys. Chem. B* **2008**, *112*, 923−928.
(137) Moreno, M.; Castiglione, F.; Mele, A.; Pasqui, C.; Raos, G. Interaction of Water with the Model Ionic Liquid [Bmim][BF_4]: Molecular Dynamics Simulations and Comparison with NMR Data. *J. Phys. Chem. B* **2008**, *112*, 7826−7836.
(138) Sun, B.; Jin, Q.; Tan, L.; Wu, P.; Yan, F. Trace of the Interesting "V"-Shaped Dynamic Mechanism of Interactions between Water and Ionic Liquids. *J. Phys. Chem. B* **2008**, *112*, 14251−14259.
(139) Takamuku, T.; Kyoshoin, Y.; Shimomura, T.; Kittaka, S.; Yamaguchi, T. Effect of Water on Structure of Hydrophilic Imidazolium-Based Ionic Liquid. *J. Phys. Chem. B* **2009**, *113*, 10817−10824.
(140) D'Angelo, P.; Zitolo, A.; Aquilanti, G.; Migliorati, V. Using a Combined Theoretical and Experimental Approach to Understand the Structure and Dynamics of Imidazolium-Based Ionic Liquids/Water Mixtures. 2. EXAFS Spectroscopy. *J. Phys. Chem. B* **2013**, *117*, 12516−12524.
(141) Martins, V. L.; Nicolau, B. G.; Urahata, S. M.; Ribeiro, M. C. C.; Torresi, R. M. Influence of the Water Content on the Structure and Physicochemical Properties of an Ionic Liquid and Its Li^+ Mixture. *J. Phys. Chem. B* **2013**, *117*, 8782−8792.
(142) Abe, H.; Takekiyo, T.; Shigemi, M.; Yoshimura, Y.; Tsuge, S.; Hanasaki, T.; Ohishi, K.; Takata, S.; Suzuki, J.-i. Direct Evidence of Confined Water in Room-Temperature Ionic Liquids by Complementary Use of Small-Angle X-ray and Neutron Scattering. *J. Phys. Chem. Lett.* **2014**, *5*, 1175−1180.
(143) Sha, M.; Dong, H.; Luo, F.; Tang, Z.; Zhu, G.; Wu, G. Dilute or Concentrated Electrolyte Solutions? Insight from Ionic Liquid/Water Electrolytes. *J. Phys. Chem. Lett.* **2015**, *6*, 3713−3720.
(144) Borodin, O.; Price, D. L.; Aoun, B.; González, M. A.; Hooper, J. B.; Kofu, M.; Kohara, S.; Yamamuro, O.; Saboungi, M.-L. Effect of Water on the Structure of a Prototype Ionic Liquid. *Phys. Chem. Chem. Phys.* **2016**, *18*, 23474−23481.
(145) Gao, J.; Wagner, N. J. Water Nanocluster Formation in the Ionic Liquid 1-Butyl-3-methylimidazolium Tetrafluoroborate ([C_4 Mim][BF_4])−D_2 O Mixtures. *Langmuir* **2016**, *32*, 5078−5084.
(146) Sharma, A.; Ghorai, P. K. Effect of Water on Structure and Dynamics of [BMIM][PF6] Ionic Liquid: An All-Atom Molecular Dynamics Simulation Investigation. *J. Chem. Phys.* **2016**, *144*, 114505.
(147) Voss, J. M.; Marsh, B. M.; Zhou, J.; Garand, E. Interaction between Ionic Liquid Cation and Water: Infrared Predissociation Study of $[Bmim]^+ \cdot (H_2 O)_n$ Clusters. *Phys. Chem. Chem. Phys.* **2016**, *18*, 18905−18913.
(148) Price, D. L.; Borodin, O.; González, M. A.; Kofu, M.; Shibata, K.; Yamada, T.; Yamamuro, O.; Saboungi, M.-L. Relaxation in a Prototype Ionic Liquid: Influence of Water on the Dynamics. *J. Phys. Chem. Lett.* **2017**, *8*, 715−719.
(149) Mariani, A.; Caminiti, R.; Gontrani, L. Water and Hexane in an Ionic Liquid: Computational Evidence of Association under High Pressure. *Phys. Chem. Chem. Phys.* **2017**, *19*, 8661−8666.
(150) E Silva, F. A.; Pereira, J. F. B.; Kurnia, K. A.; Ventura, S. P. M.; Silva, A. M. S.; Rogers, R. D.; Coutinho, J. A. P.; Freire, M. G. Temperature Dependency of Aqueous Biphasic Systems: An Alternative Approach for Exploring the Differences between Coulombic-dominated Salts and Ionic Liquids. *Chem. Commun.* **2017**, *53*, 7298−7301.
(151) Klähn, M.; Stüber, C.; Seduraman, A.; Wu, P. What Determines the Miscibility of Ionic Liquids with Water? Identification of the Underlying Factors to Enable a Straightforward Prediction. *J. Phys. Chem. B* **2010**, *114*, 2856−2868.
(152) Alfassi, Z. B.; Huie, R. E.; Milman, B. L.; Neta, P. Electrospray Ionization Mass Spectrometry of Ionic Liquids and Determination of Their Solubility in Water. *Anal. Bioanal. Chem.* **2003**, *377*, 159−164.
(153) Bowers, J.; Butts, C. P.; Martin, P. J.; Vergara-Gutierrez, M. C.; Heenan, R. K. Aggregation Behavior of Aqueous Solutions of Ionic Liquids. *Langmuir* **2004**, *20*, 2191−2198.
(154) Consorti, C. S.; Suarez, P. A. Z.; de Souza, R. F.; Burrow, R. A.; Farrar, D. H.; Lough, A. J.; Loh, W.; da Silva, L. H. M.; Dupont, J. Identification of 1,3-Dialkylimidazolium Salt Supramolecular Aggregates in Solution. *J. Phys. Chem. B* **2005**, *109*, 4341−4349.
(155) Freire, M. G.; Neves, C. M. S. S.; Carvalho, P. J.; Gardas, R. L.; Fernandes, A. M.; Marrucho, I. M.; Santos, L. M. N. B. F.; Coutinho, J. A. P. Mutual Solubilities of Water and Hydrophobic Ionic Liquids. *J. Phys. Chem. B* **2007**, *111*, 13082−13089.
(156) Aki, S. N. V. K.; Brennecke, J. F.; Samanta, A. How Polar Are Room-Temperature Ionic Liquids? *Chem. Commun.* **2001**, 413−414.
(157) Lynden-Bell, R. M.; Atamas, N. A.; Vasilyuk, A.; Hanke, C. G. Chemical Potentials of Water and Organic Solutes in Imidazolium Ionic Liquids: A Simulation Study. *Mol. Phys.* **2002**, *100*, 3225−3229.
(158) Wang, Y.-L.; Li, B.; Sarman, S.; Mocci, F.; Lu, Z.-Y.; Yuan, J.; Laaksonen, A.; Fayer, M. D. Microstructural and Dynamical Heterogeneities in Ionic Liquids. *Chem. Rev.* **2020**, *120*, 5798−5877.
(159) López-Pastor, M.; Ayora-Cañada, M. J.; Valcárcel, M.; Lendl, B. Association of Methanol and Water in Ionic Liquids Elucidated by Infrared Spectroscopy Using Two-Dimensional Correlation and Multivariate Curve Resolution. *J. Phys. Chem. B* **2006**, *110*, 10896−10902.
(160) Maia, F. M.; Rodríguez, O.; Macedo, E. A. Relative Hydrophobicity of Equilibrium Phases in Biphasic Systems (Ionic Liquid + Water). *J. Chem. Thermodyn.* **2012**, *48*, 221−228.
(161) Abe, H.; Takekiyo, T.; Yoshimura, Y.; Saihara, K.; Shimizu, A. Anomalous Freezing of Nano-Confined Water in Room-Temperature Ionic Liquid 1-Butyl-3-Methylimidazolium Nitrate. *ChemPhysChem* **2016**, *17*, 1136−1142.
(162) Dawass, N.; Krüger, P.; Schnell, S. K.; Simon, J.-M.; Vlugt, T. J. H. Kirkwood-Buff Integrals from Molecular Simulation. *Fluid Phase Equilib.* **2019**, *486*, 21−36.
(163) Kirkwood, J. G. Statistical Mechanics of Fluid Mixtures. *J. Chem. Phys.* **1935**, *3*, 300−313.
(164) Reid, J. E. S. J.; Gammons, R. J.; Slattery, J. M.; Walker, A. J.; Shimizu, S. Interactions in Water-Ionic Liquid Mixtures: Comparing Protic and Aprotic Systems. *J. Phys. Chem. B* **2017**, *121*, 599−609.
(165) Cortes-Huerto, R.; Kremer, K.; Potestio, R. Communication: Kirkwood-Buff Integrals in the Thermodynamic Limit from Small-

Downloaded from pubs.acs.org/jpcbfk/article-pdf/doi/10.1021/acs.jpcb.6c04599/6906150/acs.jpcb.6c04599.pdf by GEORGIA INST OF TECHNOLOGY, Shehan Parmar on 04 November 2026

Sized Molecular Dynamics Simulations. *J. Chem. Phys.* **2016**, *145*, 141103.
(166) Sturlaugson, A. L.; Fruchey, K. S.; Fayer, M. D. Orientational Dynamics of Room Temperature Ionic Liquid/Water Mixtures: Water-Induced Structure. *J. Phys. Chem. B* **2012**, *116*, 1777−1787.
(167) Bailey, H. E.; Wang, Y.-L.; Lynch, S. R.; Fayer, M. D. Dynamics and Microstructures of Nicotine/Water Binary Mixtures near the Lower Critical Solution Temperature. *J. Phys. Chem. B* **2018**, *122*, 9538−9548.
(168) Jenkins, H. D. B.; Marcus, Y. Viscosity B-Coefficients of Ions in Solution. *Chem. Rev.* **1995**, *95*, 2695−2724.
(169) Zhao, H. Are Ionic Liquids Kosmotropic or Chaotropic? An Evaluation of Available Thermodynamic Parameters for Quantifying the Ion Kosmotropicity of Ionic Liquids. *J. Chem. Technol. Biotechnol.* **2006**, *81*, 877−891.
(170) Köddermann, T.; Ludwig, R.; Paschek, D. On the Validity of Stokes-Einstein and Stokes-Einstein-Debye Relations in Ionic Liquids and Ionic-Liquid Mixtures. *ChemPhysChem* **2008**, *9*, 1851−1858.
(171) Del Pópolo, M. G.; Voth, G. A. On the Structure and Dynamics of Ionic Liquids. *J. Phys. Chem. B* **2004**, *108*, 1744−1752.
(172) Miao, S.; Sardharwalla, A.; Perkin, S. Ion Diffusion Reveals Heterogeneous Viscosity in Nanostructured Ionic Liquids. *J. Phys. Chem. Lett.* **2024**, *15*, 11855−11861.
(173) Mahfouz, A.; Haddad, A. Z.; Kocher, J. D.; Menon, A. K. Performance Enhancement of Aqueous Ionic Liquids with Lower Critical Solution Temperature (LCST) Behavior through Ternary Mixtures. *J. Mater. Chem. A* **2025**, *13*, 275−288.
(174) Saita, S.; Kohno, Y.; Ohno, H. Detection of Small Differences in the Hydrophilicity of Ions Using the LCST-type Phase Transition of an Ionic Liquid-Water Mixture. *Chem. Commun.* **2013**, *49*, 93−95.
(175) Gao, J.; Guo, J.; Nie, F.; Ji, H.; Liu, S. LCST-Type Phase Behavior of Aqueous Biphasic Systems Composed of Phosphonium-Based Ionic Liquids and Potassium Phosphate. *J. Chem. Eng. Data* **2017**, *62*, 1335−1340.
(176) Fukaya, Y.; Sekikawa, K.; Murata, K.; Nakamura, N.; Ohno, H. Miscibility and Phase Behavior of Water−Dicarboxylic Acid Type Ionic Liquid Mixed Systems. *Chem. Commun.* **2007**, 3089−3091.
(177) Ficke, L. E.; Rodríguez, H.; Brennecke, J. F. Heat Capacities and Excess Enthalpies of 1-Ethyl-3-methylimidazolium-Based Ionic Liquids and Water. *J. Chem. Eng. Data* **2008**, *53*, 2112−2119.
(178) Kelly, C. P.; Cramer, C. J.; Truhlar, D. G. Aqueous Solvation Free Energies of Ions and Ion-Water Clusters Based on an Accurate Value for the Absolute Aqueous Solvation Free Energy of the Proton. *J. Phys. Chem. B* **2006**, *110*, 16066−16081.
(179) Abdullah, M. A. M.; Seman, M. N. A.; Abdullah, S. B. Discovering $[C_4C_1im][BF_4]$ as Draw Solution in Forward Osmosis. *J. Adv. Manuf. Process.* **2024**, *6*, e10177.
(180) Dong, B.; Xing, X.; Wang, R.; Wang, B.; Zhou, X.; Wang, C.; Yu, L.; Wu, Z.; Gao, Y. Reversible Switching of Amphiphilic Self-Assemblies between Micelles and Microemulsions by a Thermal Stimulus. *Chem. Commun.* **2015**, *51*, 11119−11122.
(181) Nitta, A.; Morita, T.; Nishikawa, K.; Koga, Y. Mixing Scheme of an Aqueous Solution of Tetrabutylphosphonium Trifluoroacetate in the Water-Rich Region. *Phys. Chem. Chem. Phys.* **2017**, *19*, 16888−16896.
(182) Nitta, A.; Morita, T.; Ohno, H.; Nishikawa, K. Fluctuations and Mixing State of an Aqueous Solution of the Ionic Liquid Tetrabutylphosphonium Trifluoroacetate around the Critical Point. *Aust. J. Chem.* **2019**, *72*, 93−100.
(183) Mahfouz, A.; Kocher, J. D.; Haddad, A. Z.; Menon, A. K. Elucidating the Microscale Behavior and Phase Separation Kinetics of Thermally Responsive Ionic Liquid-Water Mixtures. *ACS Appl. Mater. Interfaces* **2026**, *18*, 12177−12187.
(184) Chaumont, A.; Schurhammer, R.; Wipff, G. Aqueous Interfaces with Hydrophobic Room-Temperature Ionic Liquids: A Molecular Dynamics Study. *J. Phys. Chem. B* **2005**, *109*, 18964−18973.
(185) Sieffert, N.; Wipff, G. The [BMI][Tf2N] Ionic Liquid/Water Binary System: A Molecular Dynamics Study of Phase Separation and of the Liquid-Liquid Interface. *J. Phys. Chem. B* **2006**, *110*, 13076−13085.
(186) Rocha, M. A.; Zhang, Y.; Maginn, E. J.; Shiflett, M. B. Simulation and Measurement of Water-Induced Liquid-Liquid Phase Separation of Imidazolium Ionic Liquid Mixtures. *J. Chem. Phys.* **2018**, *149*, 164503.
(187) Wang, R.; Leng, W.; Gao, Y.; Yu, L. Microemulsion-like Aggregation Behaviour of an LCST-type Ionic Liquid in Water. *RSC Adv.* **2014**, *4*, 14055−14062.
(188) Muzet, N.; Engler, E.; Wipff, G. Demixing of Binary Water-Chloroform Mixtures Containing Ionophoric Solutes and Ion Recognition at a Liquid-Liquid Interface: A Molecular Dynamics Study. *J. Phys. Chem. B* **1998**, *102*, 10772−10788.
(189) Binder, K.; Kalos, M. H. "Critical Clusters" in a Supersaturated Vapor: Theory and Monte Carlo Simulation. *Journal of Statistical Physics* **1980**, *22*, 363−396.
(190) Binder, K. Theory of First-Order Phase Transitions. *Rep. Prog. Phys.* **1987**, *50*, 783.
(191) MacDowell, L. G.; Virnau, P.; Müller, M.; Binder, K. The Evaporation/Condensation Transition of Liquid Droplets. *J. Chem. Phys.* **2004**, *120*, 5293−5308.
(192) Binder, K.; Block, B. J.; Virnau, P.; Tröster, A. Beyond the Van Der Waals Loop: What Can Be Learned from Simulating Lennard-Jones Fluids inside the Region of Phase Coexistence. *Am. J. Phys.* **2012**, *80*, 1099−1109.
(193) Thiele, U.; Frohoff-Hülsmann, T.; Engelnkemper, S.; Knobloch, E.; Archer, A. J. First Order Phase Transitions and the Thermodynamic Limit. *New J. Phys.* **2019**, *21*, No. 123021.
(194) Mohammed, H. O.; de Cozar, A.; Zangi, R. Modeling and Elucidating the Behavior of a Thermoresponsive LCST Ionic Liquid. *J. Chem. Inf. Model.* **2025**, *65*, 785−797.
(195) McDaniel, J. G. Polarization Effects in Binary $[BMIM^+][BF_4^-]$/1,2-Dichloroethane, Acetone, Acetonitrile, and Water Electrolytes. *J. Phys. Chem. B* **2018**, *122*, 4345−4355.
(196) Dodda, L. S.; Cabeza de Vaca, I.; Tirado-Rives, J.; Jorgensen, W. L. LigParGen Web Server: An Automatic OPLS-AA Parameter Generator for Organic Ligands. *Nucleic Acids Res.* **2017**, *45*, W331−W336.
(197) Jorgensen, W. L.; Maxwell, D. S.; Tirado-Rives, J. Development and Testing of the OPLS All-Atom Force Field on Conformational Energetics and Properties of Organic Liquids. *J. Am. Chem. Soc.* **1996**, *118*, 11225−11236.
(198) Jorgensen, W. L.; Tirado-Rives, J. The OPLS [Optimized Potentials for Liquid Simulations] Potential Functions for Proteins, Energy Minimizations for Crystals of Cyclic Peptides and Crambin. *J. Am. Chem. Soc.* **1988**, *110*, 1657−1666.
(199) Jorgensen, W. L.; Tirado-Rives, J. Potential Energy Functions for Atomic-Level Simulations of Water and Organic and Biomolecular Systems. *Proc. Natl. Acad. Sci. U.S.A.* **2005**, *102*, 6665−6670.
(200) Dodda, L. S.; Vilseck, J. Z.; Tirado-Rives, J.; Jorgensen, W. L. 1.14*CM1A-LBCC: Localized Bond-Charge Corrected CM1A Charges for Condensed-Phase Simulations. *J. Phys. Chem. B* **2017**, *121*, 3864−3870.
(201) Jorgensen, W. L.; Chandrasekhar, J.; Madura, J. D.; Impey, R. W.; Klein, M. L. Comparison of Simple Potential Functions for Simulating Liquid Water. *J. Chem. Phys.* **1983**, *79*, 926−935.
(202) Miyamoto, S.; Kollman, P. A. Settle: An Analytical Version of the SHAKE and RATTLE Algorithm for Rigid Water Models. *J. Comput. Chem.* **1992**, *13*, 952−962.
(203) Abascal, J. L. F.; Vega, C. A General Purpose Model for the Condensed Phases of Water: TIP4P/2005. *J. Chem. Phys.* **2005**, *123*, 234505.
(204) Berendsen, H. J. C.; Grigera, J. R.; Straatsma, T. P. The Missing Term in Effective Pair Potentials. *J. Phys. Chem. A* **1987**, *91*, 6269−6271.
(205) Martínez, L.; Andrade, R.; Birgin, E. G.; Martínez, J. M. PACKMOL: A package for building initial configurations for molecular dynamics simulations. *J. Comput. Chem.* **2009**, *30*, 2157−2164.

Downloaded from pubs.acs.org/jpcbfk/article-pdf/doi/10.1021/acs.jpcb.6c04599/6906150/acs.jpcb.6c04599.pdf by GEORGIA INST OF TECHNOLOGY, Shehan Parmar on 04 November 2026

(206) Martínez, J. M.; Martínez, L. Packing Optimization for Automated Generation of Complex System's Initial Configurations for Molecular Dynamics and Docking. *J. Comput. Chem.* **2003**, *24*, 819−825.
(207) Eastman, P.; Swails, J.; Chodera, J. D.; McGibbon, R. T.; Zhao, Y.; Beauchamp, K. A.; Wang, L.-P.; Simmonett, A. C.; Harrigan, M. P.; Stern, C. D.; Wiewiora, R. P.; Brooks, B. R.; Pande, V. S. OpenMM 7: Rapid Development of High Performance Algorithms for Molecular Dynamics. *PLoS Comput. Biol.* **2017**, *13*, e1005659.
(208) Eastman, P.; Galvelis, R.; Peláez, R. P.; Abreu, C. R. A.; Farr, S. E.; Gallicchio, E.; Gorenko, A.; Henry, M. M.; Hu, F.; Huang, J.; Krämer, A.; Michel, J.; Mitchell, J. A.; Pande, V. S.; Rodrigues, J. P.; Rodriguez-Guerra, J.; Simmonett, A. C.; Singh, S.; Swails, J.; Turner, P.; Wang, Y.; Zhang, I.; Chodera, J. D.; De Fabritiis, G.; Markland, T. E. OpenMM 8: Molecular Dynamics Simulation with Machine Learning Potentials. *J. Phys. Chem. B* **2024**, *128*, 109−116.
(209) Essmann, U.; Perera, L.; Berkowitz, M. L.; Darden, T.; Lee, H.; Pedersen, L. G. A Smooth Particle Mesh Ewald Method. *J. Chem. Phys.* **1995**, *103*, 8577−8593.
(210) Ben-Naim, A. *Solvation Thermodynamics*; Springer US: Boston, MA, 1987.
(211) Shirts, M. R.; Pitera, J. W.; Swope, W. C.; Pande, V. S. Extremely Precise Free Energy Calculations of Amino Acid Side Chain Analogs: Comparison of Common Molecular Mechanics Force Fields for Proteins. *J. Chem. Phys.* **2003**, *119*, 5740−5761.
(212) Straatsma, T. P.; McCammon, J. A. Multiconfiguration Thermodynamic Integration. *J. Chem. Phys.* **1991**, *95*, 1175−1188.
(213) Beutler, T. C.; Mark, A. E.; Van Schaik, R. C.; Gerber, P. R.; Van Gunsteren, W. F. Avoiding Singularities and Numerical Instabilities in Free Energy Calculations Based on Molecular Simulations. *Chem. Phys. Lett.* **1994**, *222*, 529−539.
(214) Sellers, M. S.; Lísal, M.; Brennan, J. K. Exponential-Six Potential Scaling for the Calculation of Free Energies in Molecular Simulations. *Mol. Phys.* **2015**, *113*, 45−54.
(215) Pham, T. T.; Shirts, M. R. Optimal Pairwise and Non-Pairwise Alchemical Pathways for Free Energy Calculations of Molecular Transformation in Solution Phase. *J. Chem. Phys.* **2012**, *136*, 124120.
(216) Mobley, D. L.; Bayly, C. I.; Cooper, M. D.; Dill, K. A. Predictions of Hydration Free Energies from All-Atom Molecular Dynamics Simulations. *J. Phys. Chem. B* **2009**, *113*, 4533−4537.
(217) Shirts, M. R.; Pande, V. S. Solvation Free Energies of Amino Acid Side Chain Analogs for Common Molecular Mechanics Water Models. *J. Chem. Phys.* **2005**, *122*, 134508.
(218) Hénin, J.; Lelièvre, T.; Shirts, M. R.; Valsson, O.; Delemotte, L. Enhanced Sampling Methods for Molecular Dynamics Simulations [Article v1.0]. *Living J. Comput. Mol. Sci.* **2022**, *4* (1), 1583 DOI: 10.33011/livecoms.4.1.1583.
(219) Atkins, P.; Paula, J. D.; Keeler, J. *Atkins' Physical Chemistry*, 12th ed.; Oxford University Press, 2022.
(220) McQuarrie, D. A. *Statistical Mechanics*; Harper & Row, 1976.
(221) Wong, D. B.; Giammanco, C. H.; Fenn, E. E.; Fayer, M. D. Dynamics of Isolated Water Molecules in a Sea of Ions in a Room Temperature Ionic Liquid. *J. Phys. Chem. B* **2013**, *117*, 623−635.
(222) Moscato, D.; Mandelli, G.; Bondanza, M.; Lipparini, F.; Conte, R.; Mennucci, B.; Ceotto, M. Unraveling Water Solvation Effects with Quantum Mechanics/Molecular Mechanics Semiclassical Vibrational Spectroscopy: The Case of Thymidine. *J. Am. Chem. Soc.* **2024**, *146*, 8179−8188.
(223) Brooks, C. L. Thermodynamics of Ionic Solvation: Monte Carlo Simulations of Aqueous Chloride and Bromide Ions. *J. Phys. Chem. A* **1986**, *90*, 6680−6684.
(224) Fleischman, S. H.; Brooks, C. L., III Thermodynamics of Aqueous Solvation: Solution Properties of Alcohols and Alkanes. *J. Chem. Phys.* **1987**, *87*, 3029−3037.
(225) Kuczera, K.; Gao, J.; Tidor, B.; Karplus, M. Free Energy of Sickling: A Simulation Analysis. *Proc. Natl. Acad. Sci. U.S.A.* **1990**, *87*, 8481−8485.
(226) Lazaridis, T.; Karplus, M. Orientational Correlations and Entropy in Liquid Water. *J. Chem. Phys.* **1996**, *105*, 4294−4316.
(227) Lu, N.; Kofke, D. A.; Woolf, T. B. Staging Is More Important than Perturbation Method for Computation of Enthalpy and Entropy Changes in Complex Systems. *J. Phys. Chem. B* **2003**, *107*, 5598−5611.
(228) Peter, C.; Oostenbrink, C.; Van Dorp, A.; Van Gunsteren, W. F. Estimating Entropies from Molecular Dynamics Simulations. *J. Chem. Phys.* **2004**, *120*, 2652−2661.
(229) Wan, S.; Stote, R. H.; Karplus, M. Calculation of the Aqueous Solvation Energy and Entropy, as Well as Free Energy, of Simple Polar Solutes. *J. Chem. Phys.* **2004**, *121*, 9539−9548.
(230) Madurga, S.; Vilaseca, E. Free Energy and Entropy Calculations in the Conformational Equilibrium of 1,2-Dichloroethane in Water. *Chem. Phys. Lett.* **2005**, *406*, 409−414.
(231) Maurer, P.; Iftimie, R. Combining *Ab Initio* Quantum Mechanics with a Dipole-Field Model to Describe Acid Dissociation Reactions in Water: First-principles Free Energy and Entropy Calculations. *J. Chem. Phys.* **2010**, *132*, No. 074112.
(232) Cabeza de Vaca, I.; Zarzuela, R.; Tirado-Rives, J.; Jorgensen, W. L. Robust Free Energy Perturbation Protocols for Creating Molecules in Solution. *J. Chem. Theory Comput.* **2019**, *15*, 3941−3948.
(233) Jorgensen, W. L. Enthalpies and Entropies of Hydration from Monte Carlo Simulations. *Phys. Chem. Chem. Phys.* **2024**, *26*, 8141−8147.
(234) Huggins, M. L. Solutions of Long Chain Compounds. *J. Chem. Phys.* **1941**, *9*, 440.
(235) Flory, P. J. Thermodynamics of High Polymer Solutions. *J. Chem. Phys.* **1942**, *10*, 51−61.
(236) Hill, T. L. *An Introduction to Statistical Thermodynamics*, unabridged, corr. republ. of the 2. printing of the work reading, mass.: addison-wesley, 1960 ed.; Dover Books on Physics; Dover Publ: New York, 1998.
(237) Ben-Naim, A., Ed. *Molecular Theory of Solutions*; Oxford University Press: Oxford, 2011.
(238) Han, Q.; Wang, X.; Bynre, N. Utilizing Water Activity as a Simple Measure to Understand Hydrophobicity in Ionic Liquids. *Front. Chem.* **2019**, *7*, 112 DOI: 10.3389/fchem.2019.00112.
(239) Haddad, A. Z.; Menon, A. K.; Revanur, R.; Klare, J.; Urban, J. J.; Kostecki, R. Forward Osmosis Desalination Using Thermoresponsive Ionic Liquids: Bench-Scale Demonstration and Cost Analysis. *Ind. Eng. Chem. Res.* **2025**, *64*, 7810−7817.
(240) Ben-Naim, A.; Marcus, Y. Solvation Thermodynamics of Nonionic Solutes. *J. Chem. Phys.* **1984**, *81*, 2016−2027.
(241) Nishikawa, K. The Solution Chemistry of Mixing States Probed via Fluctuations: A Direct Description of Inhomogeneity in Mixing. *Bull. Chem. Soc. Jpn.* **2021**, *94*, 2170−2186.
(242) Abraham, M. H.; Whiting, G. S.; Fuchs, R.; Chambers, E. J. Thermodynamics of Solute Transfer from Water to Hexadecane. *J. Chem. Soc., Perkin Trans. 2* **1990**, *2*, 291−300.
(243) Wang, Y.-L.; Sarman, S.; Kloo, L.; Antzutkin, O. N.; Glavatskih, S.; Laaksonen, A. Solvation Structures of Water in Trihexyltetradecylphosphonium-Orthoborate Ionic Liquids. *J. Chem. Phys.* **2016**, *145*, 064507.
(244) Smith, P. E.; Van Gunsteren, W. F. When Are Free Energy Components Meaningful? *J. Phys. Chem. A* **1994**, *98*, 13735−13740.
(245) Wang, X.-B.; Jagoda-Cwiklik, B.; Chi, C.; Xing, X.-P.; Zhou, M.; Jungwirth, P.; Wang, L.-S. Microsolvation of the Acetate Anion [CH 3 CO 2 - (H 2 O) n, n= 1-3]: A Photoelectron Spectroscopy and Ab Initio Computational Study. *Chem. Phys. Lett.* **2009**, *477*, 41−44.
(246) Zhang, Q.-G.; Wang, N.-N.; Wang, S.-L.; Yu, Z.-W. Hydrogen Bonding Behaviors of Binary Systems Containing the Ionic Liquid 1-Butyl-3-methylimidazolium Trifluoroacetate and Water/Methanol. *J. Phys. Chem. B* **2011**, *115*, 11127−11136.
(247) Wagman, D. D. *The NBS Tables of Chemical Thermodynamic Properties: Selected Values for Inorganic and C1 and C2 Organic Substances in SI Units*; American Chemical Society and the American Institute of Physics for the National Bureau of Standards, 1982.

Downloaded from pubs.acs.org/jpcbfk/article-pdf/doi/10.1021/acs.jpcb.6c04599/6906150/acs.jpcb.6c04599.pdf by GEORGIA INST OF TECHNOLOGY, Shehan Parmar on 04 November 2026

(248) Eisen, L.; Marano, N.; Glazier, S. Activity-Based Approach For Teaching Aqueous Solubility, Energy, and Entropy. *J. Chem. Educ.* **2014**, *91*, 484−491.
(249) Southall, N. T.; Dill, K. A.; Haymet, A. D. J. A View of the Hydrophobic Effect. *J. Phys. Chem. B* **2002**, *106*, 521−533.
(250) Kocher, J. D.; Mahfouz, A.; McDaniel, J. G.; Menon, A. K. Thermodynamic Properties of Lower Critical Solution Temperature (LCST) Mixtures for Application in Energy-Water Systems. *Phys. Chem. Chem. Phys.* **2025**, *27*, 15024−15036.
(251) Parmar, S. M.; Dean, W.; Do, C.; Browning, J. F.; Klein, J. M.; Gurkan, B. E.; McDaniel, J. G. Structural Properties of [N1888]-[TFSI] Ionic Liquid: A Small Angle Neutron Scattering and Polarizable Molecular Dynamics Study. *J. Phys. Chem. B* **2024**, *128*, 11313−11327.
(252) Kelkar, M. S.; Shi, W.; Maginn, E. J. Determining the Accuracy of Classical Force Fields for Ionic Liquids: Atomistic Simulation of the Thermodynamic and Transport Properties of 1-Ethyl-3-methylimidazolium Ethylsulfate ([Emim][$EtSO_4$]) and Its Mixtures with Water. *Ind. Eng. Chem. Res.* **2008**, *47*, 9115−9126.
(253) Cranmer, M. Interpretable Machine Learning for Science with PySR and SymbolicRegression.Jl. *arXiv* 2023, *arXiv:2305.01582*.
(254) Podgoršek, A.; Jacquemin, J.; Pádua, A. A. H.; Costa Gomes, M. F. Mixing Enthalpy for Binary Mixtures Containing Ionic Liquids. *Chem. Rev.* **2016**, *116*, 6075−6106.
(255) Ficke, L. E.; Brennecke, J. F. Interactions of Ionic Liquids and Water. *J. Phys. Chem. B* **2010**, *114*, 10496−10501.
(256) Ficke, L. E.; Novak, R. R.; Brennecke, J. F. Thermodynamic and Thermophysical Properties of Ionic Liquid + Water Systems. *J. Chem. Eng. Data* **2010**, *55*, 4946−4950.
(257) Navia, P.; Troncoso, J.; Romaní, L. Excess Magnitudes for Ionic Liquid Binary Mixtures with a Common Ion. *J. Chem. Eng. Data* **2007**, *52*, 1369−1374.
(258) Chang, C.-K.; Siepmann, J. I. Enthalpy of Mixing and Liquid Structure for Mixtures of Primary and Secondary Alcohols: Molecular Simulations and COSMO-SAC Calculations. *J. Chem. Eng. Data* **2024**, *69*, 509−525.
(259) Troncoso, J. Isobaric Heat Capacity of Ionic Liquids in Aqueous Solutions. A Review. *J. Chem. Eng. Data* **2019**, *64*, 4611−4618.
(260) Katayanagi, H.; Nishikawa, K.; Shimozaki, H.; Miki, K.; Westh, P.; Koga, Y. Mixing Schemes in Ionic Liquid-H_2O Systems: A Thermodynamic Study. *J. Phys. Chem. B* **2004**, *108*, 19451−19457.
(261) Mason, T. G.; Seeger, Z. L.; Nguyen, A. L. P.; Fujita, K.; Izgorodina, E. I. Predicting Entropic Effects of Water Mixing with Ionic Liquids Containing Anions of Strong Hydrogen Bonding Ability: Role of the Cation. *J. Phys. Chem. B* **2020**, *124*, 9182−9194.
(262) Shah, J. K.; Maginn, E. J. Monte Carlo Simulations of Gas Solubility in the Ionic Liquid 1-n-Butyl-3-methylimidazolium Hexafluorophosphate. *J. Phys. Chem. B* **2005**, *109*, 10395−10405.
(263) Ben-Amotz, D.; Underwood, R. Unraveling Water's Entropic Mysteries: A Unified View of Nonpolar, Polar, and Ionic Hydration. *Acc. Chem. Res.* **2008**, *41*, 957−967.
(264) Garza, A. J. Solvation Entropy Made Simple. *J. Chem. Theory Comput.* **2019**, *15*, 3204−3214.
(265) Murphy, K. P. Hydration and Convergence Temperatures: On the Use and Interpretation of Correlation Plots. *Biophys. Chem.* **1994**, *51*, 311−326.
(266) Hansen, J. P.; McDonald, I. R. Statistical Mechanics of Dense Ionized Matter. IV. Density and Charge Fluctuations in a Simple Molten Salt. *Phys. Rev. A* **1975**, *11*, 2111−2123.
(267) Stillinger, F. H., Jr; Lovett, R. General Restriction on the Distribution of Ions in Electrolytes. *J. Chem. Phys.* **1968**, *49*, 1991−1994.
(268) Caillol, J. M.; Levesque, D.; Weis, J. J. Electrical Properties of Polarizable Ionic Solutions. I. Theoretical Aspects. *J. Chem. Phys.* **1989**, *91*, 5544−5554.
(269) McDaniel, J. G.; Yethiraj, A. Influence of Electronic Polarization on the Structure of Ionic Liquids. *J. Phys. Chem. Lett.* **2018**, *9*, 4765−4770.
(270) McDaniel, J. G.; Son, C. Y. Ion Correlation and Collective Dynamics in BMIM/BF4-Based Organic Electrolytes: From Dilute Solutions to the Ionic Liquid Limit. *J. Phys. Chem. B* **2018**, *122*, 7154−7169.
(271) Bowron, D. T.; D'Agostino, C.; Gladden, L. F.; Hardacre, C.; Holbrey, J. D.; Lagunas, M. C.; McGregor, J.; Mantle, M. D.; Mullan, C. L.; Youngs, T. G. A. Structure and Dynamics of 1-Ethyl-3-methylimidazolium Acetate via Molecular Dynamics and Neutron Diffraction. *J. Phys. Chem. B* **2010**, *114*, 7760−7768.
(272) Araque, J. C.; Hettige, J. J.; Margulis, C. J. Modern Room Temperature Ionic Liquids, a Simple Guide to Understanding Their Structure and How It May Relate to Dynamics. *J. Phys. Chem. B* **2015**, *119*, 12727−12740.
(273) Brehm, M.; Thomas, M.; Gehrke, S.; Kirchner, B. TRAVIS−A Free Analyzer for Trajectories from Molecular Simulation. *J. Chem. Phys.* **2020**, *152*, 164105.
(274) Weingärtner, H.; Merkel, T.; Maurer, U.; Conzen, J.-P.; Glasbrenner, H.; Käshammer, S. On Coulombic and Solvophobic Liquid-Liquid Phase-Separation in Electrolyte Solutions. *Ber. Bunsenges. Phys. Chem.* **1991**, *95*, 1579−1586.
(275) Oluwole, S. A.; Weldu, W. D.; Agatemor, C. Hydrophobicity-Driven Enhancement of Hydrogen Bonding in Ionic Liquid Hybrid Solvents. *J. Phys. Chem. B* **2025**, *129*, 7228−7237.
(276) Sun, Q. The Hydrophobic Effects: Our Current Understanding. *Molecules* **2022**, *27*, 7009.
(277) Pártay, L. B.; Jedlovszky, P.; Brovchenko, I.; Oleinikova, A. Formation of Mesoscopic Water Networks in Aqueous Systems. *Phys. Chem. Chem. Phys.* **2007**, *9*, 1341−1346.
(278) Bernardes, C. E. S.; Minas da Piedade, M. E.; Canongia Lopes, J. N. The Structure of Aqueous Solutions of a Hydrophilic Ionic Liquid: The Full Concentration Range of 1-Ethyl-3-methylimidazolium Ethylsulfate and Water. *J. Phys. Chem. B* **2011**, *115*, 2067−2074.
(279) Verma, A.; Stoppelman, J. P.; McDaniel, J. G. Tuning Water Networks via Ionic Liquid/Water Mixtures. *International Journal of Molecular Sciences* **2020**, *21*, 403.
(280) Stoppelman, J. P.; McDaniel, J. G. Proton Transport in [BMIM+][BF4−]/Water Mixtures Near the Percolation Threshold. *J. Phys. Chem. B* **2020**, *124*, 5957−5970.
(281) McGibbon, R. T.; Beauchamp, K. A.; Harrigan, M. P.; Klein, C.; Swails, J. M.; Hernández, C. X.; Schwantes, C. R.; Wang, L.-P.; Lane, T. J.; Pande, V. S. MDTraj: A Modern Open Library for the Analysis of Molecular Dynamics Trajectories. *Biophys. J.* **2015**, *109*, 1528−1532.
(282) Parmar, S. M. Shehan807/Mdtraj: Molecular Aggregation Analysis. Zenodo 2026.
(283) Leskiv, M.; Bernardes, C. E. S.; Minas Da Piedade, M. E.; Canongia Lopes, J. N. Energetics of Aqueous Solutions of the Ionic Liquid 1-Ethyl-3-methylimidazolium Ethylsulfate. *J. Phys. Chem. B* **2010**, *114*, 13179−13188.
(284) Dill, K. A.; Bromberg, S.; Kocher, C. D.; Balázsi, G. *Molecular Driving Forces: Statistical Thermodynamics in Biology, Chemistry, Physics, and Nanoscience*; 3rd ed.; MIT Press: Cambridge, MA, USA, 2026.
(285) Koga, Y. *Solution Thermodynamics and Its Application to Aqueous Solutions*; Elsevier, 2007; pp 23−49.
(286) Rowlinson, J. S.; Swinton, F. L. *Liquids and Liquid Mixtures*; Elsevier, 1982; pp 86−131.
(287) de Souza, J. P.; Stone, H. A. Exact Analytical Solution of the Flory-Huggins Model and Extensions to Multicomponent Systems. *J. Chem. Phys.* **2024**, *161*, 044902.
(288) Bates, F. S. Polymer-Polymer Phase Behavior. *Science* **1991**, *251*, 898−905.
(289) Kim, J. Y. Phase Behavior of Conjugated Polymer Solutions and Blends: The Flory-Huggins Lattice Model. *J. Phys. Chem. C* **2025**, *129*, 3983−3992.
(290) Bingham, E.; Chen, J. P.; Jankowiak, M.; Obermeyer, F.; Pradhan, N.; Karaletsos, T.; Singh, R.; Szerlip, P. A.; Horsfall, P.; Goodman, N. D. Pyro: Deep Universal Probabilistic Programming. *J. Mach. Learn. Res.* **2019**, *20* (28), 1−6.

Downloaded from pubs.acs.org/jpcbfk/article-pdf/doi/10.1021/acs.jpcb.6c04599/6906150/acs.jpcb.6c04599.pdf by GEORGIA INST OF TECHNOLOGY, Shehan Parmar on 04 November 2026

(291) Phan, D.; Pradhan, N.; Jankowiak, M. Composable Effects for Flexible and Accelerated Probabilistic Programming in NumPyro. *arXiv* 2019, *arXiv:1912.11554*.
(292) Ganose, A. M.; Sahasrabuddhe, H.; Asta, M.; Beck, K.; Biswas, T.; Bonkowski, A.; Bustamante, J.; Chen, X.; Chiang, Y.; Chrzan, D. C.; Clary, J.; Cohen, O. A.; Ertural, C.; Gallant, M. C.; George, J.; Gerits, S.; Goodall, R. E. A.; Guha, R. D.; Hautier, G.; Horton, M.; Inizan, T. J.; Kaplan, A. D.; Kingsbury, R. S.; Kuner, M. C.; Li, B.; Linn, X.; McDermott, M. J.; Mohanakrishnan, R. S.; Naik, A. N.; Neaton, J. B.; Parmar, S. M.; Persson, K. A.; Petretto, G.; Purcell, T. A. R.; Ricci, F.; Rich, B.; Riebesell, J.; Rignanese, G.-M.; Rosen, A. S.; Scheffler, M.; Schmidt, J.; Shen, J.-X.; Sobolev, A.; Sundararaman, R.; Tezak, C.; Trinquet, V.; Varley, J. B.; Vigil-Fowler, D.; Wang, D.; Waroquiers, D.; Wen, M.; Yang, H.; Zheng, H.; Zheng, J.; Zhu, Z.; Jain, A. Atomate2: Modular Workflows for Materials Science. *Digital Discovery* **2025**, *4*, 1944−1973.
(293) Parmar, S. M.; Cohen, O.; Persson, K. A.; Vaghjiani, G. L.; McDaniel, J. G.; Wirz, R. E. Multimode Propellant Discovery: A Computational High-Throughput Screening Paradigm. *J. Electr. Propulsion* **2026**, *5*, No. 1.

Downloaded from pubs.acs.org/jpcbfk/article-pdf/doi/10.1021/acs.jpcb.6c04599/6906515O/acs.jpcb.6c04599.pdf by GEORGIA INST OF TECHNOLOGY, Shehan Parmar on 04 November 2026

https://doi.org/10.1021/acs.jpcb.6c04599
J. Phys. Chem. B XXXX, XXX, XXX−XXX